COMPLEX MIXED-MODE OSCILLATIONS AND A SEARCH FOR OSCILLATOR GLASS

A Dissertation

Presented to the Faculty of the Graduate School

of Cornell University

in Partial Fulfillment of the Requirements for the Degree of

Doctor of Philosophy

by

Ian Malcolm Lizarraga

August 2017

COMPLEX MIXED-MODE OSCILLATIONS AND A SEARCH FOR OSCILLATOR GLASS

Ian Malcolm Lizarraga, Ph.D.

Cornell University 2017

In this thesis, we consider problems across two families of dynamical systems: low-dimensional systems that have multiple timescales, and high-dimensional systems of coupled oscillators.

We study a three-dimensional system in two slow and one fast variables, which has been used to model electrochemical oscillations. We demonstrate the existence of a manifold of elusive Shilnikov homoclinic orbits in the parameter space. Each of these orbits organizes a complex structure of mixed-mode oscillations (MMOs).

We then study the dynamics near a tangency bifurcation between an unstable manifold and a slow manifold. We find bifurcations and define a dynamical partition to analyze some of the complicated MMOs which arise immediately after the tangency.

Finally, we consider a variant of a Kuramoto system which has been used as a model of spin glass. We apply an ansatz of Ott and Antonsen to effectively reduce the dimension of the system, and derive a phase diagram of the system.

To dad, errant scholar

To mom, prudent sage

BIOGRAPHICAL SKETCH

Ian was born in Belize City, Belize on June 14, 1990. After spending 18 years avoiding winter, he moved to Evanston, IL, USA to attend Northwestern University. He then moved to Ithaca, NY three years later to attend Cornell University. After receiving his PhD in applied mathematics, Ian will join the Cornell math department as a visiting assistant professor.

His relationship with snow remains ambivalent.

ACKNOWLEDGEMENTS

I would like to thank my advisor, John Guckenheimer, and my co-mentor, Steve Strogatz (research dads with joint custody), for their consistent and gentle mentoring throughout my time in Ithaca. I would also like to thank Richard Rand, the third member of my committee, for his illuminating course on perturbation methods in dynamical systems, and for being generous with his time and advice whenever I asked for it.

Alex Vladimirsky graciously lent his experience to give me useful advice towards the end of my program. Kelly Delp has been a wonderful source of teaching support over the past year. I'm also very grateful to many of the administrators in both the applied math center and the math department for their support along the way, including Karen Benavidez, Tara Woodard, Jake Gibson, Mikki Klinger, Heather Peterson, Steve Gaarder, and Kelly Patwell.

To my friends old and new, and especially Jessica, Ryan, Zach, Matt, Hintellect, Aurya, Danielle, Isabelle, Mimi, Iian, and Rocío, thank you for being lovely company and compassionate sounding boards.

Finally, to my family: though we sail across the world, we keep our lines tethered. Thank you for keeping me close even when we're far apart.

TABLE OF CONTENTS

LIST OF FIGURES

CHAPTER 1

INTRODUCTION

This thesis collects three self-contained publications across two quite different paradigms in applied dynamical systems. It seems clearest to discuss these paradigms in separate sections; however, it is worth mentioning immediately that the results are phrased in terms of bifurcation theory and dimension reduction, emphatically from a geometric point of view. In one family of systems we are concerned with, our techniques derive from *geometric singular perturbation theory*. In the other, we effectively reduce the dimension of a system with a large number of coupled oscillators by grouping subfamilies of oscillators into distinct communities, following a trick due to Edward Ott and Thomas Antonsen.

1.1 Slow-fast systems and mixed-mode oscillations

Multiple-timescale (or *slow-fast*) dynamical systems have been used to model natural phenomena in which distinct mechanisms operate on vastly different timescales. Researchers have used this framework to model processes as diverse as climate phenomena, complex chemical reactions, cell bursting, and combustion (an excellent literature review is provided in [25]). We generally formulate a slow-fast system as follows:

$$\begin{aligned} \varepsilon \dot{x} = \varepsilon \frac{dx}{d\tau} &= f(x, y, \lambda, \varepsilon) \\ \dot{y} = \frac{dy}{d\tau} &= g(x, y, \lambda, \varepsilon), \end{aligned} \tag{1.1}$$

where $x \in \mathbb{R}^m$ denotes the *fast* variable, $y \in \mathbb{R}^n$ denotes the *slow* variable, $\lambda \in \mathbb{R}^k$ lists the parameters, and $\varepsilon > 0$ characterizes the ratio of the slow to fast

timescales. The functions f, g are assumed to have some degree of smoothness. In this thesis, $m = 1$, $n = 2$, and f, g are smooth.

One can consider two formal, 'low-dimensional' limits of (1.1). Setting $\varepsilon = 0$ in (1.1), we obtain the system

$$\begin{aligned} 0 &= f(x, y, \lambda, 0) \\ \dot{y} &= g(x, y, \lambda, 0). \end{aligned} \tag{1.2}$$

This system is referred to as the *slow subsystem* (or *slow flow equations*) of (1.1). The set $C = \{(x, y) : f(x, y, \lambda, 0)$ defines the *critical* manifold of (1.1) upon which trajectories of the slow flow are confined. Away from folds of C, we may apply the implicit function theorem to write S as a graph of the slow variables and rescale time in the resulting system by $\pm \det(D_x f)$ to obtain a desingularized slow flow.

On the other hand, we may define the *fast timescale* $t = \tau/\varepsilon$. Making this substitution into (1.1) and then formally setting $\varepsilon = 0$ again, we obtain the *layer equations*

$$\begin{aligned} x' = \frac{dx}{dt} &= f(x, y, \lambda, 0) \\ y' = \frac{dy}{dt} &= 0. \end{aligned} \tag{1.3}$$

The typical goal is to understand how trajectories of the simpler systems (1.2)-(1.3) give insight into trajectories for the full system (1.1) when $\varepsilon > 0$.

A remarkable set of theorems due to Fenichel [31] gives tremendous insight into the connection between the flow of the full system and the slow flow on C, assuming that ε is sufficiently small and a property called *normal hyperbolicity* is

satisfied. We say that a subset $S \subset C$ is normally hyperbolic if for each $p \in S$, the eigenvalue spectrum of the matrix $D_x f(p)$ does not intersect the imaginary axis in the complex plane. Fenichel then shows that there exist nonunique, locally invariant *slow manifolds* S_ε which perturb from S. Furthermore, these slow manifolds inherit the smoothness and stability properties of S, and the flow on S_ε converges to the slow flow on S as $\varepsilon \to 0$.

Therefore, for $\varepsilon > 0$ sufficiently small, trajectories of the full system may be analyzed fruitfully as perturbations of concatenations of trajectories which follow the slow flow for $O(1)$ time, interspersed by fast 'jumps' across normally hyperbolic branches of C along fast fibers of the layer equation.

Particularly interesting solutions that arise in such systems are *mixed-mode oscillations* (MMOs), which are solutions having large and small oscillations and a distinct gap between the two. The definitions of 'large' and 'small' depend on the system being studied. An MMO is typically classified by its *signature*, which is a finite symbolic sequence of the form $L_1^{s_1} L_2^{s_2} \cdots L_k^{s_k}$, indicating that the trajectory undergoes L_1 large oscillations, followed by s_1 small oscillations, then L_2 large oscillations, and so on.

Researchers have been concerned with exploring the emergence of MMOs having certain signatures, as well as identifying signature transitions between MMOs. An archetypical example of such a result, which gives an indication of the state of the theory, will now be described. *Folded singularities* are equilibrium points of the desingularized slow flow. For $m = 1$, $n = 2$, we define a *folded node* as an equilibrium point of this system, whose linearization has nonzero real

eigenvalues with the same sign. A normal form for this system is

$$\begin{aligned} \varepsilon \dot{x} &= y - x^2 \\ \dot{y} &= z - x \\ \dot{z} &= -\nu, \end{aligned} \tag{1.4}$$

where ε, ν are the parameters. Let $\mu < 1$ denote the ratio of eigenvalues of the linearization at the folded node.

Brøns, Krupa, and Wechselberger [16] proved the following :

Theorem 1 *Consider the system* (1.1) *with* $m = 1, n = 2$ *such that:*

(FN1) $0 < \varepsilon \ll 1$ *is sufficiently small,* $\sqrt{\varepsilon} \ll \mu$*, and* $k \in \mathbb{N}$ *satisfies* $2k+1 < \mu^{-1} < 2k+3$.

(FN2) The critical manifold C *is locally a folded surface.*

(FN3) The reduced problem contains a folded node (i.e. the normal form near the singularity is given by (1.4)*).*

(FN4) There exists a 'candidate' periodic orbit, i.e. a formal concatenation of fast fibers, a global return segment, and a segment which connects to the folded node within the 'funnel' defined by the stable manifolds of the folded node on C*.*

(FN5) An appropriate transversality condition is satisfied, for eg. the projection of the folds onto the sheets of C *is transverse to the slow flow.*

Then there exists a stable 1^{k+1} *MMO.*

The folded node case is arguably among the simplest nontrivial cases where we can prove the existence of MMOs having a certain signature; yet, the arguments are already quite involved, involving careful analytic arguments based

on techniques such as geometric blow-up theory. For more sophisticated scenarios (for eg. interactions of Hopf bifurcations with folded singularities, which are *separately* associated with the emergence of periodic orbits), the theory remains woefully incomplete; yet, these scenarios do arise in models, and are furthermore associated with the emergence of very complicated MMO signatures indeed. A firmer synthesis of the theory with the numerical methods, which we have used fairly successfully to study some of these complicated scenarios, is eagerly awaited.

Chapter 2 of this thesis solves a problem first posed by Marc Koper and Pierre Gaspard in the early nineties [58]. They were concerned with modeling the complicated, and possibly chaotic, electrochemical oscillations observed by an indium-thiocyanate solution at a mercury electrode. Koper and Gaspard derived a minimal three-dimensional dynamical system using a shell approximation of the reaction-diffusion PDEs which describe the system. They located tantalizing evidence of a Shilnikov homoclinic orbit, but were unable to settle its existence with certainty. This bifurcation is known as a precursor of extremely complicated dynamics, including countably many periodic orbits as well as aperiodic, chaotic trajectories. In a paper with John Guckenheimer, we locate this Shilnikov orbit and analyze the MMO structure nearby.

In chapter 3, a numerical exploration is given of a tangency bifurcation of a slow manifold of the system, with the unstable manifold of a saddle-focus equilibrium point. This bifurcation heralds the emergence of MMOs which arise from interactions between the invariant manifolds of the equilibrium point, the slow manifolds, a folded singularity in the system, and a small-amplitude stable periodic orbit together with its basin of attraction. Bifurcations occurring after

this tangency, and their influence on MMO transitions, are catalogued. A new dynamical partition is also presented, which we use to describe some unusual, unstable MMOs which are not neatly described as 'small or large' oscillations. We also identify a Smale-Birkhoff homoclinic orbit. Numerical calculations related to escape rates support the conjecture that the orbit is a chaotic attractor.

1.2 Coupled oscillators and the Ott-Antonsen ansatz

Large systems of coupled limit-cycle oscillators have been used to model collective synchronization problems across physics, engineering, biology, and social science. A universal formulation of the long-term dynamics when the oscillators are nearly identical and the coupling is weak was first derived by Kuramoto [63]:

$$\begin{aligned} \dot{\theta}_i &= \omega_i + \sum_{i=1}^{N} \Gamma_{ij}(\theta_j - \theta_i) \\ & \qquad i = 1, \cdots, N, \end{aligned} \tag{1.5}$$

where N is a large positive integer denoting the number of oscillators, and the natural frequencies ω_i are distributed according to some probability density $g(\omega)$. The family of interaction functions between oscillators is given by $\{\Gamma_{ij}\}$. Many natural models have symmetric coupling, giving rise to the constraint $\Gamma_{ij} = \Gamma_{ji}$ (or indeed, $\Gamma_{ij} \equiv \Gamma$).

We focus briefly on the classical Kuramoto model, where $\Gamma_{ij}(\theta_j - \theta_i) = (K/N)\sin(\theta_j - \theta_i)$ and $K \geq 0$ is the coupling strength. Moving to the complex

plane and defining the complex order parameter

$$z(t) \quad = \quad r(t)e^{i\phi(t)} = \frac{1}{N}\sum_{j=1}^{N} e^{i\theta_j}, \tag{1.6}$$

the Kuramoto model may be rewritten as $\dot{\theta}_i = \omega_i + Kr\sin(\psi - \theta_i)$. Here, $r(t)$ measures phase coherence and $\phi(t)$ is the average phase. By considering the continuum limit as $N \to \infty$, Kuramoto then made a remarkable series of symmetry and self-consistency arguments to derive the existence of a *critical* coupling strength $K = K_c$. Before this bifurcation, coupling is too weak for the oscillators to spontaneously synchronize; after, the oscillators split into two distinct groups: a "drifting" state where $|\omega_i| > Kr$ and a "phase-locked" state where $|\omega_i| \leq Kr$.

This is just the beginning of a sprawling story in the field of coupled oscillators. One important chapter is the study of the stability of these phase states, culminating with a *tour-de-force* analysis by Crawford [21] in which he derives, among other results, a normal form for $r(t)$ near the neighborhood of the incoherent state $r = 0$ and a proof of the local stability of the partially synchronized states. The point is that even in this relatively simple model, these calculations are delicate and not easy to generalize. Crawford's derivation drew upon careful center manifold expansions and equivariant bifurcation theory, to study bifurcations of reflection-symmetric distributions.

Another piece of this story is the realization, via numerical calculations, that low-dimensional behavior is a pervasive feature of coupled oscillator models, hinting at the existence of attracting invariant manifolds in these systems. Crawford's center manifold calculation may be seen retroactively as a rigorous push to classify some of these low-dimensional features, but the nature of these

constants of motion remained unclear except in a few cases. See for example a derivation of constants of motion in a Josephson array model by Watanabe and Strogatz using coordination transformations.

A 2009 paper by Ott and Antonsen [72] introduced a clever ansatz which suddenly rendered an entire host of Kuramoto-type problems immediately tractable, starting a gold rush in the field. A brief list of this proliferation is given in the introduction of our third paper. The key to this ansatz is to locate a dynamically invariant submanifold in the system which accurately reproduces the long-term macroscopic dynamics. Since we do not demonstrate this ansatz in detail in our paper, it is worthwhile to show off a simple example using the technique. In the $N \to \infty$ limit, the classical Kuramoto model is given by the continuity equation describing conservation of oscillators:

$$\rho_t + (\rho v)_\theta = 0, \tag{1.7}$$

where $\rho(\theta, t)$ is the phase density and $v(\theta, \omega, t) = \omega + (K/2i)(re^{-i\theta} + r^* e^{i\theta})$ is the oscillator velocity field (r^* denotes complex conjugation). The complex order parameter becomes $z(t) = \int_0^{2\pi} \int_{-\infty}^{\infty} \rho e^{i\theta} d\omega d\theta$ in this limit.

Ott and Antonsen make the following step: express ρ as the following Fourier series in θ:

$$\rho(\theta, t) = \frac{g(\omega)}{2\pi}\left[1 + \sum_{n=1}^{\infty}(\alpha^n e^{in\theta} + (\alpha^*)^n e^{-in\theta})\right], \tag{1.8}$$

where $\alpha = \alpha(\omega, t)$ is an unspecified function which is independent of θ. This ansatz represents a considerable simplification: we are demanding that the nth Fourier coefficient c_n satisfies the simple relation $c_n = \alpha^n$. For example, this is the series for a Poisson kernel on the complex unit disc in the case when α is real and less than 1.

Substituting this ansatz into the continuity equation, the amplitude equations are satisfied for each harmonic if and only if the Fourier coefficient function $\alpha(\omega, t)$ evolves according to the following family of integro-differential equations in t, parametrized by the frequency ω:

$$\begin{aligned} \frac{\partial \alpha}{\partial t} &= -i\omega\alpha - \frac{K}{2}(r\alpha^2 - z^*) \\ z(t) &= \int_{-\infty}^{\infty} \alpha(\omega, t) g(\omega) d\omega. \end{aligned} \tag{1.9}$$

The usefulness of the ansatz rests upon a gentle complex-analytic requirement: we assume that the analytic continuation of $\alpha(\omega, t)$ from the line $\mathrm{Im}(\omega) = 0$ has no singularities when $\mathrm{Re}(\omega) < 0$ and that $|\alpha| \to 0$ as $\mathrm{Im}(\omega) \to -\infty$.

Let us take the Lorentzian distribution $g(\omega) = 1/[\pi(1 + \omega^2)]$. Note that $g(0) = 1/\pi$. Consider the lower semicircle $S(R) = \{R = c, \pi \leq \varphi \leq 2\pi\} \cup \{-R \leq \mathrm{Re}(z) \leq R, \mathrm{Im}(z) = 0\}$ of radius $R > 0$ in the complex plane. We may now compute the integral for $z(t)$ above by computing the contour integral $\int_{S(R)} \alpha(\omega, t) g(\omega) d\omega$ as $R \to \infty$ to obtain $z(t) = \alpha^*(-i, t)$. Thus, setting $\omega = -i$ in (1.9) and writing the complex order parameter equations $z(t) = r(t)e^{i\phi(t)}$ in polar coordinates, we obtain the following closed system:

$$\begin{aligned} \dot{r} &= \left(\frac{K}{2} - 1\right) r - \frac{K}{2} r^3 \\ \dot{\phi} &= 0. \end{aligned} \tag{1.10}$$

We see here that we recover the critical value $K_c = 2 = 2/(\pi g(0))$ originally derived by Kuramoto, as well as the value of the centroid $r = \sqrt{1 - K_c/K}$ of partially synchronized states which bifurcate from incoherence ($r = 0$) above the critical value.

The technique is similar for more sophisticated variants of the Kuramoto

model. Clever choices of frequency distributions $g(\omega)$ and the use of residues allow us to extract finite-dimensional dynamics on an invariant submanifold to which the family of oscillators is enslaved.

In the final chapter of this thesis, we study a coupled-oscillator model of disordered spin glass introduced by Van Hemmen. We use the technique of Ott and Antonsen to derive a closed ODE system of four complex-valued oscillator populations. Happily, this system is amenable to standard techniques in dynamical systems, allowing us to draw a phase diagram of the four stable states produced by the system in the large N limit. The states giving 'glassy' behavior (and the limitations of the model therein) are discussed in context in that chapter.

CHAPTER 2

SHILNIKOV HOMOCLINIC BIFURCATION OF MIXED-MODE OSCILLATIONS

2.1 Abstract

The Koper model is a three-dimensional vector field that was developed to study complex electrochemical oscillations arising in a diffusion process. Koper and Gaspard described paradoxical dynamics in the model: they discovered complicated, chaotic behavior consistent with a homoclinic orbit of Shilnikov type, but were unable to locate the orbit itself. The Koper model has since served as a prototype to study the emergence of mixed-mode oscillations (MMOs) in slow-fast systems, but only in this paper is the existence of these elusive homoclinic orbits established. They are found first in a larger family that has been used to study singular Hopf bifurcation in multiple time scale systems with two slow variables and one fast variable. A curve of parameters with homoclinic orbits in this larger family is obtained by continuation and shown to cross the submanifold of the Koper system. The strategy used to compute the homoclinic orbits is based upon systematic investigation of intersections of invariant manifolds in this system with multiple time scales. Both canards and folded singularities are multiple time scale phenomena encountered in the analysis. Suitably chosen cross-sections and return maps illustrate the complexity of the resulting MMOs and yield a modified geometric model from the one Shilnikov used to study spiraling homoclinic bifurcations.

2.2 Introduction

In 1992, Marc Koper and Pierre Gaspard introduced a three-dimensional model to analyze an electrochemical diffusion problem, in which layer concentrations of electrolytic solutions fluctuate nonlinearly at an electrode [58, 59]. They sought to model mixed-mode oscillations (MMOs) arising in a wide variety of electrochemical systems. Their analysis revealed a host of complicated dynamics, including windows of period-doubling bifurcations, Hopf bifurcations, and complex Farey sequences of MMO signatures.

They also found regions in the parameter space where the equilibrium point of the system satisfies the Shilnikov condition.[1] Within these regions, they observed that trajectories repeatedly come close to the fixed point, and return maps strongly suggest chaotic motion consistent with a Shilnikov homoclinic bifurcation. However, they were unable to locate a genuine homoclinic orbit to account for this behavior, so it was catalogued as a *near-homoclinic scenario*. In such a scenario, complex and chaotic MMOs could suddenly arise—as if from a homoclinic bifurcation—but without the existence of the homoclinic orbit to serve as an organizing center.

Nevertheless, the Koper model has emerged as a paradigm in studies of slow-fast systems containing MMOs [14, 25]. As its four parameters are varied, local mechanisms such as folded nodes [16, 36, 89] and singular Hopf bifurcation [4, 14, 36, 43, 46] generate small-amplitude oscillations. A global return mechanism allows for repeated reinjection into the regions containing these local objects. The interplay of these local and global mechanisms gives rise to

[1] Let the linearization of a three-dimensional vector field at an equilibrium point p have eigenvalues $\rho \pm i\omega$ and λ, where ρ, ω, and λ are all real. Then p satisfies the *Shilnikov condition* if $\rho\lambda < 0$ and $|\rho/\lambda| < 1$.

sequences of large and small oscillations characterized by signatures that count the numbers of consecutive small and large oscillations. Shilnikov homoclinic orbits are limits of families of MMOs with an unbounded number of small oscillations in their signatures. When the Shilnikov condition is satisfied, they also guarantee the existence of chaotic invariant sets whose presence in the Belousov-Zhabotinsky reaction was controversial for several years (eg. [35]).

The homoclinic orbits that could explain Koper's original observations have remained elusive. This paper describes their first successful detection. Multiple time scales make numerical study of these homoclinic orbits quite delicate; on the other hand, the presence of *slow manifolds* allows us to analyze many aspects of the system with low-dimensional maps. We find the homoclinic orbits by exhibiting multiple time scale phenomena such as canards and folded singularities. We first locate such orbits in a five-parameter family of vector fields used to explore the dynamics of singular Hopf bifurcation. After an affine coordinate change, the Koper model is a four-parameter subfamily. Shooting methods that compute trajectories between carefully chosen cross-sections cope with the numerical instability resulting from the singular behavior of the equations. Following identification of a homoclinic orbit in the larger family, a continuation algorithm is used to track a curve on the codimension-one manifold of spiraling homoclinic orbits in parameter space. This manifold intersects the parametric submanifold corresponding to the Koper model, locating the homoclinic orbit that is the target of our search.

This paper is a numerical investigation of *the* Koper model. The results are not rigorous, so a formal "theorem-proof" style is inappropriate for this discussion. Following the numerical part of the paper, we abstract our reasoning to

present a geometric model for the slow-fast decomposition of the homoclinic orbits of the Koper model. This geometric model produces a list of properties that we use to prove the existence of a homoclinic orbit in a slow-fast system. We think these properties may be amenable to verification in the Koper model through the use of interval arithmetic.

2.3 The Koper model as a slow-fast system

We consider vector fields of the form

$$\begin{aligned} \varepsilon \dot{x} &= f(x, y), \\ \dot{y} &= g(x, y), \end{aligned} \tag{2.1}$$

where $x \in R^m$, $y \in R^n$, and the functions f and g are smooth. In this paper, f and g are polynomials. *Slow-fast* vector fields are those where $\varepsilon \ll 1$. In this case, x is the fast variable and y is the slow-variable.

The Koper model is a frequently studied example and the subject of this paper. It is defined by

$$\begin{aligned} \varepsilon_1 \dot{u} &= kv - u^3 + 3u - \lambda, \\ \dot{v} &= u - 2v + w, \\ \dot{w} &= \varepsilon_2 (v - w), \end{aligned} \tag{2.2}$$

and has two slow variables v and w and one fast variable u when the parameters $\varepsilon_1 \ll 1$ and $\varepsilon_2 = 1$. The terms k and λ are additional parameters. We assume throughout this paper that $\varepsilon_2 = 1$ without further comment.

The study of slow-fast vector fields has advanced rapidly in recent years

with specific focus on systems having two slow variables and one fast variable. We recall relevant aspects of the theory that bear on the Koper model. The review paper [25] includes an extensive discussion that provides additional information, especially about MMOs.

The set of points defined by $C = \{f = 0\}$ in system (2.3) is called the *critical manifold*. Fenichel [31] proved the existence of locally invariant slow manifolds near regions of C where $D_x f$ is hyperbolic. Trajectories on the slow manifolds are approximated by trajectories of the *reduced system* on C defined by

$$\dot{y} = g(h(y), y, 0), \tag{2.3}$$

where h is defined implicitly by $f(h(y), y, 0) = 0$. While the slow manifolds are not unique, compact portions are exponentially close to each other: their distances from each other are $O(\exp(-c/\varepsilon))$ as $\varepsilon \to 0$. We often refer to 'the' slow manifold in statements where the choice of slow manifold does not matter. The points $x \in C$ where $D_x f$ is singular are called *fold points*. For the Koper model, C is the zero set of $kv - u^3 + 3u - \lambda$, and the fold curve consists of the points on C with $\frac{3}{k}(u^2 - 1) = 0$. The reduced system is given by

$$\begin{aligned} \frac{3}{k}(u^2 - 1)\dot{u} &= u - 2v + w, \\ \dot{w} &= (v - w), \end{aligned} \tag{2.4}$$

where $v = \frac{1}{k}(u^3 - 3u + \lambda)$.

The reduced system is a *differential algebraic equation* that is the main component of the *singular limit* of the "full" system (2.2) as $\varepsilon_1 \to 0$. The other component of the singular limit comes from the fast part of the full system. The fold curve divides the critical manifold into attracting and repelling sheets where $u^2 > 1$ and $u^2 < 1$, respectively. When trajectories of the full system reach the

vicinity of the fold curves, they turn and then flow close to the fast direction to a small neighborhood of the attracting slow manifold. In the singular limit, one has trajectories on the attracting and repelling sheets of the critical manifold that meet at the fold curve separating the sheets. The limiting behavior of the full system from these impasse points is to *jump* along the fast direction stopping at the first intersection with an attracting sheet of C. The addition of fast jumps makes the singular limit a *hybrid* system whose trajectories (called *candidates*) consist of concatenations of slow segments that solve the reduced system and fast jumps parallel to the fast direction. As we describe below, fast jumps may occur at points of C which are not fold points.

Rescaling time in the reduced system produces a *desingularized* reduced system that extends to the fold curve. In the case of the Koper model, the desingularized reduced system is

$$\begin{aligned} \dot{u} &= u - 2v + w, \\ \dot{w} &= \frac{3}{k}(u^2 - 1)(v - w), \end{aligned} \tag{2.5}$$

where $v = \frac{1}{k}(u^3 - 3u + \lambda)$. Discrete time jumps of trajectories that reach the fold curve of (2.5) are added to the reduced model to reflect the limiting behavior of the full system. However, there are exceptional trajectories of the full system that flow from an attracting slow manifold to a repelling slow manifold without making a jump at the fold curve. The singular limits of these trajectories flow to equilibrium points of (2.5) which lie on its fold curves. Since the time rescaling of desingularization reverses the direction of time on the repelling sheet of C where $u^2 < 1$, we follow trajectories of (2.5) backwards in time "through" the singularity. At any location along such a backward trajectory, a jump to one of the attracting sheets of the slow manifold is allowed along the fast direction.

This makes the reduced system multivalued and hence still more complicated. See [12] for further discussion of this construction of a hybrid reduced model in the context of the forced van der Pol system.

The desingularized reduced system of a fast-slow system can have two types of equilibrium points. Equilibria of the "full" system are retained as equilibria of the desingularized reduced system. Additionally, points on a fold curve may become equilibria of the desingularized reduced system because the time rescaling factor vanishes at these points. For the Koper model, these *folded singularities* are solutions of the equations $kv - u^3 + 3u - \lambda$, $u - 2v + w = 0$, and $u^2 - 1 = 0$. (The third of these equations replaces the equation $\dot{z} = 0$ for an actual equilibrium.) The folded singularities are further classified as *folded nodes*, *saddles*, *saddle-nodes*, and *foci* depending on their type as equilibria of the desingularized reduced system. The folded singularities mark transitions along the fold curve where the trajectories of the reduced system (without desingularization) approach the fold curve or flow away from it. They are also close to places where the full system might have trajectories that contain segments on an attracting slow manifold that proceed to follow the repelling slow manifold without an intervening jump. Trajectory segments that flow for time $O(1)$ in the slow time scale along a repelling slow manifold of a slow-fast systems are called *canards*. They have been the subject of intense study since they were found in periodic orbits of the forced van der Pol equation [77, 27, 29]. They also play an important role in the dynamics of the Koper model and are part of the homoclinic orbits we find. See Figure 2.1.

The dynamics of the full system close to folded singularities is significantly more complicated than suggested by the reduced system. Benoît [6] observed

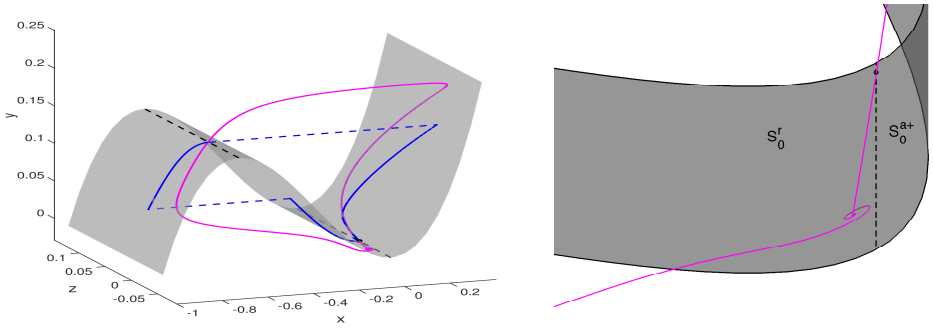

(a) (b)

Figure 2.1: (a) Shilnikov homoclinic orbit (magenta curve) found in the Koper model, defined by (3.2), alongside a typical singular homoclinic orbit defined by trajectories (blue solid curves) lying on the critical manifold (gray surface) of the system, concatenated with instantaneous jumps (blue dashed curves) to different branches of the critical manifold. Fold lines are given by black dashed curves. Section 2.8 discusses families of singular homoclinic orbits in detail. (b) A cartoon of the local dynamics. The homoclinic orbit departs along the two-dimensional unstable manifold of the equilibrium and returns by passing very close to a folded singularity of the singular system, given by the black dot on the fold line separating the sheets S_0^r and S_0^{a+} of the critical manifold. These sheets perturb to attracting and repelling slow manifolds for small values of the singular perturbation parameter ε.

that trajectories of the full system near folded nodes of the reduced system can make small-amplitude oscillations in directions that involve both fast and slow variables. The oscillations are manifest in the twisting of the attracting and repelling slow manifolds, as visualized by Desroches [25]. The maximum number of small oscillations of trajectories passing through this region is bounded, with a bound determined from a normal form for the folded node [6, 89]. In the Koper model and other slow-fast systems, small oscillations associated with folded nodes together with "global returns" produce *mixed mode oscillations* (MMOs) [25].

Our goal in this paper is to locate a homoclinic orbit of the Koper model when its equilibrium is a saddle-focus. The initial portion of such an orbit consists of small-amplitude oscillations as the homoclinic orbit spirals away from the equilibrium along its unstable manifold (see Fig. 2.1). In single time scale systems, both shooting and boundary value methods can be used to find the homoclinic orbit. With both types of algorithms, as well as in theoretical analysis of the dynamics near the homoclinic orbit, trajectories are decomposed into a local portion in a neighborhood of the equilibrium and a global portion that lies outside that neighborhood. Linearization or higher order approximations are used to identify the local stable and unstable manifolds, and then numerical methods are used to find the global return.

Because the homoclinic bifurcation is a codimension-one phenomenon, an "active" parameter is used in locating the bifurcation. Extending the phase space to include the active parameter, the homoclinic orbit becomes a transverse intersection of the families of stable and unstable manifolds of the curve of equilibria in the extended system. Shooting methods locate the global return by computing a two-parameter family of initial value problems whose initial conditions depend on the active parameter and a coordinate that parameterizes trajectories in the unstable manifold. The intersections of these trajectories with a cross-section of the local stable manifolds form a surface while the family of local stable manifolds intersects the cross-section in a curve. The cross-section is three-dimensional in the extended phase space, so the intersections of the stable and unstable manifolds can cross transversally.

Straightforward implementation of this strategy fails in the Koper model, as Koper discovered in his original investigation. The slow-fast structure of the

problem makes portions of the global return trajectories so sensitive that continuous dependence on initial conditions appears to fail for numerical solutions of initial value problems. This apparent discontinuity of trajectories has been documented in the "canard explosions" of the van der Pol equation with constant forcing [38]. The crux of our analysis of the Koper homoclinic model is to decompose the global returns into segments, each of which can be reliably computed with either forward or backward integration. This strategy has worked with other examples like the canard explosion [41] of the van der Pol system with constant forcing, and it proves successful again here.

When the Koper model equilibrium is a saddle-focus, its two-dimensional unstable manifold is a source of small-amplitude oscillations. The number of small amplitude oscillations is unbounded as trajectories leave the equilibrium. However, their magnitude changes quickly unless the ratio of the real and complex parts of the complex eigenvalues at the equilibrium is small. Parameter regions close to a Hopf bifurcation yield small ratios, so choosing parameters in such a region is part of our strategy for finding homoclinic orbits. Hopf bifurcation in slow-fast systems takes several forms that depend on whether the two-dimensional subspace of center directions lie in fast directions, slow directions, or a mixture of the two. The third case is called *singular Hopf bifurcation*, and it is the case that occurs in the Koper model. In systems with two slow variables, singular Hopf bifurcation is closely associated with a phenomenon in the desingularized reduced system called *folded saddle-node, type II* (FSNII)[89]. This occurs in the desingularized reduced system when an equilibrium (that is not a folded singularity) crosses a fold curve as a parameter is varied. As the equilibrium crosses the fold curve, a folded singularity passes through the same point, and its type switches between a fold node and a folded saddle. Singular

Hopf bifurcations are found at a distance $O(\varepsilon)$ from the FSNII point.

The dynamics of a model system with an FSNII bifurcation have been analyzed by Guckenheimer and Meerkamp [43]. The model they studied is obtained by truncating a Taylor expansion at the FSNII bifurcation: it can be viewed informally as a normal form for this problem and for singular Hopf bifurcation. Moreover, this normal form is closely related to the Koper model. With the addition of a single cubic term and an appropriate affine coordinate change, it contains the Koper system as a subfamily. We make use of this relationship below, first finding a homoclinic orbit of the larger family and then continuing it to parameters that lie in the (transformed) Koper family. The FSNII normal form has many different types of bifurcations, and small-amplitude chaotic behavior is possible [43]. Complicated small scale dynamics of this system raise the possibility of homoclinic orbits that are more complicated than those we exhibit in this paper.

A key aspect of the FSNII dynamics relevant to our search for homoclinic orbits in the Koper model is the intersection of the unstable manifold of the equilibrium with the repelling slow manifold. Since both of these manifolds are two-dimensional, we expect them to intersect along isolated trajectories. The homoclinic orbits we find contain segments close to such intersections. As trajectories in the unstable manifold emerge from the equilibrium point, they may follow the repelling slow manifold for some distance, producing a canard that can then jump away from the repelling manifold. Part of our computational task is to identify the jump point that yields the homoclinic orbit.

By definition, the homoclinic orbit contains a branch of the stable manifold of the equilibrium. We find that this branch lies close to the attracting slow man-

ifold for a substantial distance. A second key part of our computations stems from the observation that the stable manifold of the equilibrium crosses the attracting slow manifold as a parameter is varied and that the homoclinic bifurcation lies exponentially close to this parameter value. Finding this crossing is delicate because the stable manifold passes through a region where extensions of the normally hyperbolic attracting manifold twist. Most of the studies of mixed mode oscillations of the Koper model to date are based upon local analysis of oscillations close to perturbations of a folded node or near the equilibrium. Here, we need to study trajectories that interact with both the equilibrium and a twisting, attracting slow manifold, a situation that remains poorly understood. Our homoclinic orbit lies close to such trajectories, and further analysis of their dynamics is likely to produce interesting results.

We close this section with three remarks:

1. Folded singularities are defined for the reduced system that is the singular limit of a slow-fast system. In the full system with time scale parameter $\varepsilon > 0$, these entities are no longer defined. However, it is useful to identify points that are located where their influence is manifest. We use the term *twist region* to describe sets in the phase space of the full system where an (extended) attracting slow manifold twists around a canard. Numerically, we locate approximations to these points as folded nodes of the reduced system obtained by setting $\varepsilon = 0$.

2. We consider only parameter values of the Koper model for which its equilibrium point p_{eq} has a pair of complex conjugate eigenvalues $\rho \pm i\omega$ and one real eigenvalue λ with $\lambda < 0 < \rho$. This constraint forces the equilibrium to be within a distance $O(\varepsilon)$ of the folded singularity of the singular

limit. This requirement is explained further in Section 2.4 below. When we study the singular limit of the system, we do so along parameter curves along which the equilbrium remains a saddle-focus.

3. Numerical studies of slow-fast systems always rely on particular choices of the time scale parameter $\varepsilon > 0$, while the theory focuses on dynamics that are present for "small enough ε." It is rare that one can verify that a particular choice of ε is indeed small enough to fall within the scope of particular theorems. Nonetheless, the theory provides a guide to expected behavior in the numerics, explaining observations that would otherwise appear anomalous. These studies are based on the presumption that ε is sufficiently small and test this presumption by examining the dynamics for different values of ε. However, like the theory, the problem of connecting the behavior observed at specific values of $\varepsilon > 0$ with the singular limit is nontrivial. Our approach here is to show that we find behavior *consistent* with that described by perturbations from the singular limit.

2.4 The singular Hopf extension of the Koper model

We now introduce a family of vector fields with two slow variables and one fast variable that contains a singular Hopf bifurcation [4, 14, 36, 43, 46]. It is given by

$$\begin{aligned} \varepsilon \dot{x} &= y - x^3 - x^2, \\ \dot{y} &= z - x, \\ \dot{z} &= -\nu - ax - by - cz, \end{aligned} \tag{2.6}$$

where ε, ν, a, b, and c are parameters, x is the fast variable, and y and z are the slow variables. We denote $\alpha = (\varepsilon, \nu, a, b, c)$ and define P to be the five-dimensional space of parameters α. The critical manifold is the S-shaped cubic surface $\{y = x^3 + x^2\}$ with two *fold lines* at L_0 (defined as $\{x = 0\}$) and $L_{-2/3}$ (defined as $\{x = -2/3\}$). In our numerical investigations, we set $\varepsilon = 0.01$ unless otherwise noted.

"The" slow manifold S has sheets S_ε^{a-}, S_ε^r and S_ε^{a+} that lie close to the sheets of the critical manifold C defined by $C \cap \{x < -2/3\}$, $C \cap \{-2/3 < x < 0\}$ and $C \cap \{0 < x\}$. Away from the fold lines, forward trajectories are attracted to $S_\varepsilon^{a\pm}$ and repelled from S_ε^r at fast exponential rates (see, eg., [53] for a derivation of estimates using the Fenichel normal form).

After the affine coordinate change defined by $(x, y, z) = ((u - 1)/3, (kv - \lambda + 2)/27, 2v - w - 1)/3)$ [25], scaling time by $-k/9$, and the substitutions

$$(\varepsilon, a, b, c, \nu) = (-k\varepsilon_1/81, 18/k, 81\varepsilon_2/k^2, -9(\varepsilon_2 + 2)/k, (3\lambda - 6 - 3k)\varepsilon_2/k^2),$$

the Koper model becomes a parametric subfamily of (3.2), with parameters satisfying the equation

$$2b + a(a + c) = 0. \tag{2.7}$$

Note that the above parametric equation corrects a sign error in Desroches et al.[25]. We work henceforth with the Koper model in the form given by (3.2).

The corresponding desingularized slow flow of the system (3.2) is given by

$$\begin{aligned} \dot{x} &= z - x \\ \dot{z} &= -(2x + 3x^2)(\nu + ax + b(x^2 + x^3) + cx). \end{aligned} \tag{2.8}$$

In analogy to (2.5), this two-dimensional system is derived by rescaling time

with the term $(2x + 3x^2)$. The origin is always an equilibrium of (2.8), so $n = (0, 0, 0) \in L_0$ is a folded singularity of (3.2).

We consider only parameter sets of (3.2) satisfying the following conditions: (i) the reduced system (2.8) has a singularity at $(0, 0)$, which is a folded node for $\nu > 0$, (ii) exactly one equilibrium point p_{eq} exists in the full system with $\nu = O(\varepsilon)$, with a pair of complex conjugate eigenvalues $\rho \pm i\omega$ and one real eigenvalue λ, (iii) the stable manifold W^s of p_{eq} is one-dimensional and the unstable manifold W^u of p_{eq} is two-dimensional ($\lambda < 0 < \rho$). Our notation for W^s and W^u hides their dependence on the parameter values.

We comment on requirements (i) and (ii) above. When studying the singular limit $\varepsilon \to 0$ of system (3.2), condition (ii) requires that ν must also change, so that the limiting system has an FSNII.

In this regime, small-amplitude oscillations may be due to intersections of the attracting and repelling slow manifolds as they twist around each other near a folded singularity [25, 89] or to the spiraling of trajectories near the unstable manifold of the equilibrium or both. We find that the homoclinic orbits we seek pass through the twisting region, so that the interactions of W^s and W^u with the slow manifolds of the system play a significant role in their existence. In particular, the homoclinic orbits we locate contain segments that lie close to the intersection of W^u with the repelling slow manifold S^r_ε, similar to the homoclinic orbits that form the traveling wave profiles for the FitzHugh-Nagumo equation [40], a system with one slow variable and two fast variables. The homoclinic orbits also contain segments where W^s lies close to S^{a+}_ε.

To focus on trajectories that pass through a twist region before encoun-

tering the equilibrium, we use the position of the equilibrium as an alternative to the parameter ν. This position is given by $p_{eq} = (x_{eq}, x_{eq}^2 + x_{xeq}^3, x_{eq})$, so $\nu = -x_{eq}[a + bx_{eq}(x_{eq} + 1) + c]$ and the family can be parameterized by (x_{eq}, a, b, c) instead of (ν, a, b, c). With this new parameterization, the equilibrium point remains fixed as the parameters a, b, and c are varied, while the twist region is a small neighborhood of the origin. In the rest of this paper, we set $x_{eq} = -0.03$ whenever we study system (3.2) with $\varepsilon > 0$, except in the concluding remarks where we let the distance between p_{eq} and L_0 vary with ε.

2.5 The shooting procedure

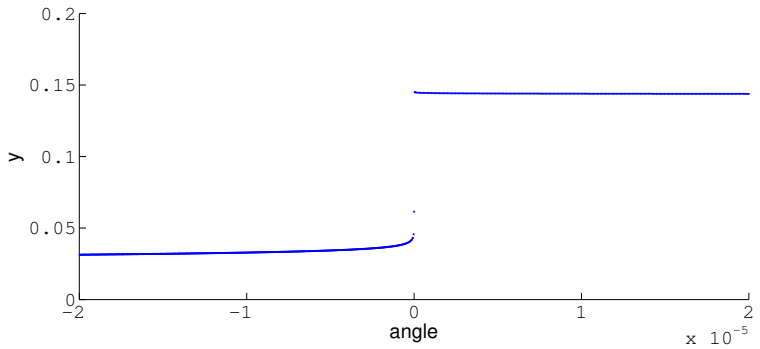

Figure 2.2: Height (y value) of forward trajectories in W^u crossing the surface $\{x = -0.05\}$ as a function of angle. An angle of 0 corresponds to a trajectory of height $y = 0.1$ lying in $S_\varepsilon^r \cap W^u$. The parameter set is $(\varepsilon, a, b, c) \approx (0.01, -4.416165, 2.891404, 5.725663)$.

The boundary value algorithm HOMCONT [17] was created within the package AUTO [28] to compute homoclinic orbits with a collocation procedure. Nonetheless, we have been unsuccessful in using AUTO or MATCONT [26] to locate a Shilnikov homoclinic orbit in (3.2) when $\varepsilon \ll 1$. The stiffness of the vector field appears to prevent convergence to a homoclinic solution even when very large numbers of collocation points are used. Shooting algorithms are also

problematic since trajectories of W^u diverge rapidly from each other near a canard segment of the homoclinic orbit. Thus, parameterizing trajectories in W^u by an angular variable and varying the angle of an initial point is not well suited to locating a Shilnikov homoclinic orbit because trajectories in W^u are extremely sensitive to the angle of an initial condition near p_{eq} (see Fig. 2.2). This issue suggests a different shooting strategy than varying this angle. Instead, we define an angular variable, θ that parameterizes trajectories in W^u smoothly (including as a function of the parameters) and regard it as an additional parameter for the system. So $W^u = \cup_\theta W^u_\theta$. The shooting procedure can then fix θ and use another parameter in the search for a homoclinic orbit that contains W^u_θ.

Our extended family has the six-dimensional parameter space $\bar{P}$ with coordinates (α, θ). The homoclinic submanifold of the extended parameter space persists as a codimension-one object [39]. To obtain defining equations $\psi : \bar{P} \to \Sigma$ for this manifold, we choose the surface of section Σ defined by $z = 0$, set s^α to be the *first* intersection (in backward time) of W^s with Σ, u^α_θ to be the *first* intersection (in forward time) with decreasing z of W^u_θ with Σ, and define $\psi(\alpha, \theta) = s^\alpha - u^\alpha_\theta$. The relation $\psi(\alpha, \theta) = 0$ defines a four-dimensional submanifold $\bar{H}$ of $\bar{P}$. The projection of $\bar{H}$ to P is a homoclinic manifold H consisting of parameters for which (3.2) has a homoclinic orbit.

Approximations to s^α and u^α_θ are obtained by numerically integrating trajectories with initial conditions in the linear stable and unstable subspaces of p_{eq}. Denoting these approximations by $\tilde{s}^\alpha$ and $\tilde{u}^\alpha_\theta$ the formula $\tilde{\psi}(\alpha, \theta) = \tilde{s}^\alpha - \tilde{u}^\alpha_0$ approximates the defining equations. Previous studies [8, 9, 3, 78] analyze the convergence of the solutions $\tilde{\alpha}$ of $\tilde{\psi} = 0$ as the distance of the initial conditions to p_{eq} tends to 0. Hyperbolicity of the fixed point, which is satisfied by p_{eq}, is

required for these estimates.

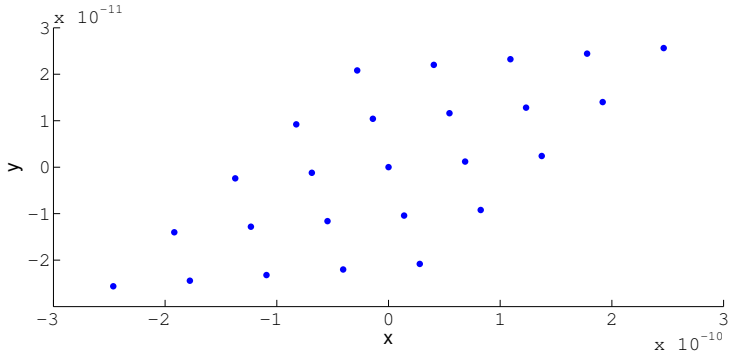

Figure 2.3: The image of a square grid of parameters (a, b) under the shooting function ψ_{Σ_0} in the surface $\Sigma_0 = \{z = 0\}$. The location of the Shilnikov homoclinic orbit is found to be close to the parameters $\tilde{\alpha} \approx (0.01, -0.03, -0.2515348, -1.6508230, 1)$. Integrations were performed for a square grid of points (a, b) in the domain of ψ_{Σ_0}, specified by $a \in [\tilde{a} - 2 * 10^{-6}, \tilde{a} + 2 * 10^{-6}]$ and $b \in [\tilde{b} - 2 * 10^{-6}, \tilde{b} + 2 * 10^{-6}]$.

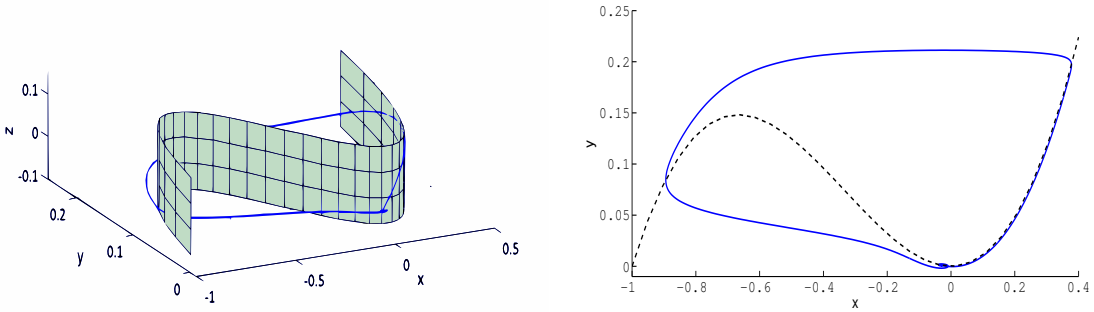

(a) (b)

Figure 2.4: Homoclinic orbit (blue curve) to p_{eq} specified by the parameters $\theta = 0$ and $\tilde{\alpha}$ in Fig. 3.12. The critical manifold $C = \{y = x^2 + x^3\}$ is given by the light green manifold in (a) and its xy-projection is given by the black dashed curve in (b).

We now reduce the number of active parameters by fixing $\varepsilon = 0.01$, $\theta = 0$, $c = 1$, and $x_{eq} = -0.03$. Note that our choice of Σ as the hyperplane $z = 0$ is motivated by the complicated dependence of W^s on the parameters [36]. This section slices through a twist region and is close enough to the equilibrium point

that small changes in α do not produce large jumps in s^{α}. These choices leave a and b as active parameters to vary in $\bar{P}$ to locate an approximate homoclinic orbit by solving the approximate defining equations $\tilde{\psi} = 0$.

Figure 3.12 illustrates the regularity of the defining equations $\tilde{\psi} = 0$ on a small rectangle $A \subset R^2$ of points in the space of active parameters (a, b). Blue dots represent the images of a 5×5 lattice of points in A under the shooting function $\tilde{\psi}$. The data indicate that $\tilde{\psi}$ is close to affine and regular on A and that its image contains the point $(0, 0)$, implying that there exists $(\tilde{a}, \tilde{b}) \in A$ with $\tilde{\psi}(\tilde{\alpha}) = 0$, where $\tilde{\alpha}$ is the parameter set with second and third components given by $(\tilde{a}, \tilde{b})$. This in turn implies the existence of a Shilnikov homoclinic orbit, depicted by the blue curve in Figure 2.4.

2.6 Continuation of the homoclinic orbit

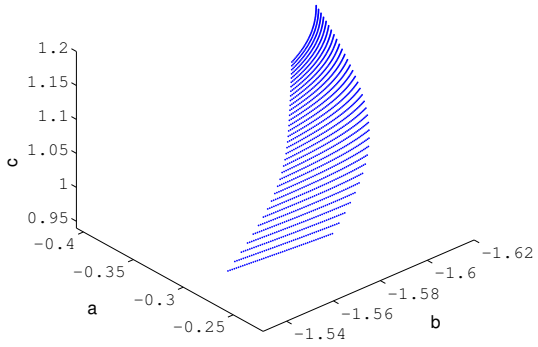

Figure 2.5: A portion of H created with continuation. The portion was projected from (θ, a, b, c) space to (a, b, c) space. The apparent curves show the results of continuation in the direction of one of the two nullvectors of $J = D\xi$.

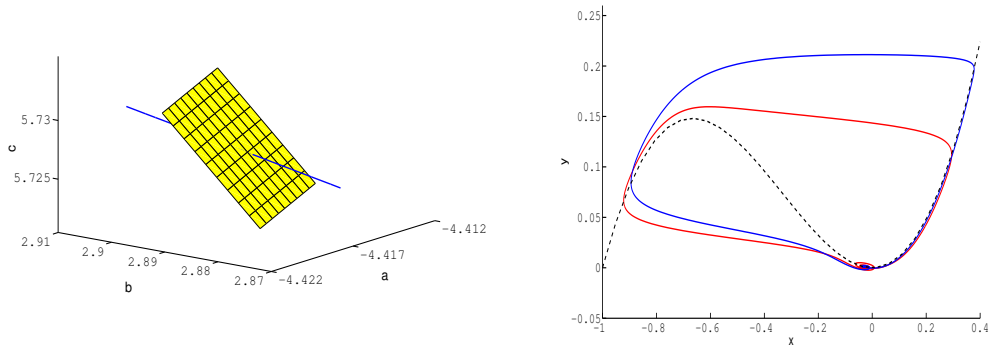

(a) (b)

Figure 2.6: (a) Continuation of a curve (blue) on H_0' through a local patch of the Koper manifold (yellow) defined by Eq. 2.7. (b) A comparison of the homoclinic orbit defined by the parameter set $\tilde{\alpha}$ (blue curve) and the homoclinic orbit lying in the Koper subfamily (red curve) obtained via the continuation in (a), with parameter set $\beta = (\varepsilon_\beta, a_\beta, b_\beta, c_\beta) \approx (0.01, -4.416165, 2.891404, 5.725663)$. The eigenvalues of p_{eq} for the Koper homoclinic are $(\rho \pm i\omega, \lambda) \approx (0.790204 \pm 8.482321i, -1.576071)$, so p_{eq} satisfies the Shilnikov condition.

Continuation algorithms [65] are widely used to find curves of bifurcations in multidimensional parameter spaces. Here, the goal is to find an intersection of the homoclinic manifold H with the subfamily of (3.2) that yields the Koper model. The tangent space to $\bar{H}$ is the null space of $D\psi$. We estimate $D\psi$ with a central finite difference method to provide starting data for continuation calculation of curves on $\bar{H}$. The following iterative calculations use a *predictor-corrector* algorithm to compute a sequence of parameter values α_j on H. This iteration converges for small stepsizes [2].

1. *Prediction*: Compute $w^0 = \alpha^j + hv^j$, where $v^j \in \text{null}(D\psi)$ and h is our chosen stepsize.
2. *Correction*: Choose a tolerance δ; iteratively compute $w^{k+1} = w^k - (D\psi)^+(w^k)\psi(w^k)$, where J^+ is the *Moore-Penrose pseudoinverse matrix* of J de-

fined by $J^+ = J^T(JJ^T)^{-1}$.

3. *Stopping criterion*: Stop when $||w^{k+1} - w^k|| < \delta$ and let $\alpha^{j+1} = w^{k+1}$.

We fix $\varepsilon = 0.01$, $x_{eq} = -0.03$, and θ and then use c as the third active parameter in addition to a and b in the continuation calculation of a curve on H. Figure 2.5 shows a computation of a patch of H in (a, b, c) space with different curves corresponding to different values of θ. Figure 2.6(a) shows a transversal intersection of one of these curves on H with the Koper manifold given by Eq. 2.7. The affine transformations relating (3.2) to the Koper model will rescale and shift the homoclinic orbit (shown in Figure 2.6(b)) while preserving its topological structure.

2.7 Transversality of invariant manifolds

The homoclinic orbit exists for the full system (3.2) when a trajectory in the two-dimensional unstable manifold W^u flows along S^r_ε to a point where it jumps to S^{a-}_ε, and then flows along S^{a-}_ε to its fold, jumps again to S^{a+}_ε, and then flows along this manifold to the folded node region, where it connects to the one-dimensional local stable manifold W^s of the equilibrium. This only happens when the parameter values lie in the homoclinic submanifold H of the parameter space. We can visualize how this happens by looking at intersections of W^s and W^u in the cross-section $z = 0$ that pass through the twist region. On this cross-section, W^s sweeps out a curve C and S^a_ε sweeps out a two-dimensional surface S as the parameter a is varied. Figure (2.7) shows this intersection in (x, y, n) space where the local coordinate n is defined via $(x, y, a) \cdot \eta = n$ and η is a unit vector normal to a small patch of S. This choice of coordinates increases the

angle of intersection that occurs in (x, y, a) space. As a varies, the surface swept out by W^u intersects the curve swept out by W^s transversally, demonstrating that the solution of the defining equation for the homoclinic orbit is regular.

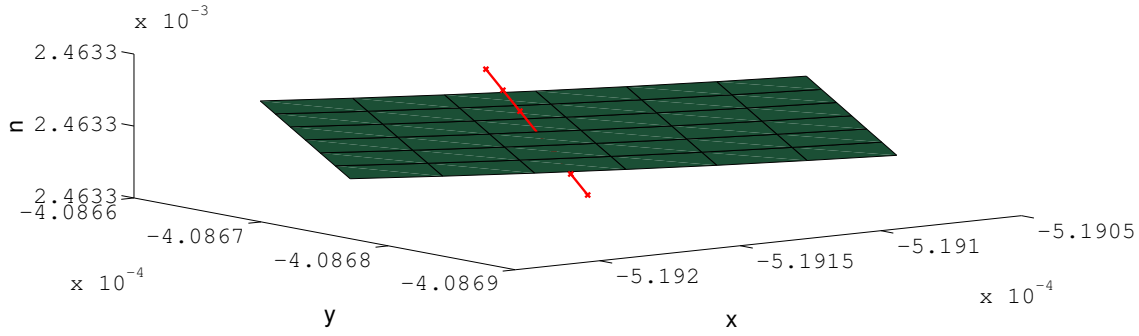

Figure 2.7: Transversal intersection in $\{z = 0\}$ of surface S (green) swept out by S^a_ε and curve C (red) swept out by W^s as the parameter a is varied. Intersection corresponds to homoclinic orbit defined by β as given in Fig. 2.6. Integrations were performed for $a \in [a_\beta - 3 * 10^{-5}, a_\beta + 3 * 10^{-5}]$.

It is difficult to directly compute the relevant portion of W^u since it contains canards. The two-dimensional subset of S^r_ε we want to compute consists of trajectories which leave the fixed point p_{eq} along its unstable manifold and follow the repelling slow manifold S^r_ε up to some height y, before finally jumping across to S^{a-}_ε. In order to locate this part of S^r_ε, we first integrate backward a line of initial conditions at a particular height lying midway between the jump from S^r_ε to S^{a+}_ε. These backward trajectories jump to S^r_ε and flow along it before turning along one of the two branches of W^s as they approach the equilibrium point. Since trajectories lying in W^u separate those trajectories which follow the two branches of W^s, we can locate the trajectory γ in $S^r_\varepsilon \cap W^u$ with a bisection method. We then compute an approximation to the strong unstable manifold of γ by integrating forward points on either side of W^u that lie close to γ. This strategy relies on the fact that trajectories in W^u approximate leaves of the strong

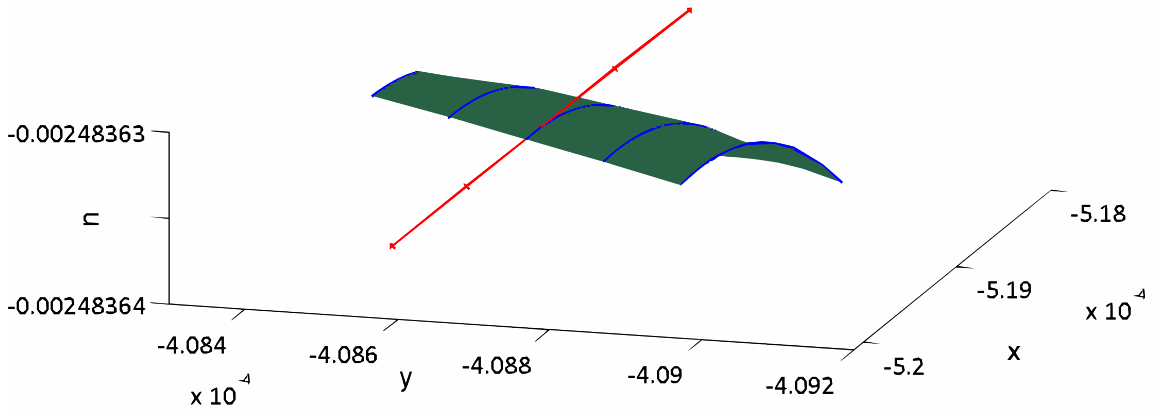

Figure 2.8: Transversal intersection in $\{z = 0\}$ of the surface S' (green) swept out by $S^r_\varepsilon \cap W^u$ and the curve C (red) swept out by W^s as the parameter a is varied. The intersection corresponds to the homoclinic orbit defined by β as given in Fig. 2.6. Integrations were performed for five equally spaced values of $a \in [a_\beta - 3 * 10^{-5}, a_\beta + 3 * 10^{-5}]$. Intersections of W^u (blue curves) for different values of a are shown.

unstable foliation of S_r for the canard trajectory in $S^r_\varepsilon \cap W^u$. As discussed in section 4, the resulting heights of the trajectories are extremely sensitive to the angle as illustrated in Figure (2.2). Since the calculation of W^u is lengthy and indirect, we located the homoclinic orbit parameters by instead finding intersections of W^s with S^{a+}_ε. Figure (2.7) shows that as we vary the parameter a, the intersections of W^s with S^{a+}_ε are similar to those of W^u and W^s shown in Figure ((2.8)). As before, this figure locates the transversal intersections of W^u and W^s on the surface of section specified by $\{z = 0\}$. Trajectories lying on $S^r_\varepsilon \cap W^u$ sweep out a two-dimensional surface S' and the stable manifold sweeps out a curve C. The objects S' and C intersect transversally (Figure 2.8).

2.8 Singular homoclinic orbits

As $\varepsilon \to 0$, trajectories for (3.2) have singular limits consisting of concatenations of fast segments ("jumps") parallel to the x-axis and segments that are trajectories of the reduced system on the critical manifold. Transitions from slow to fast segments in the singular limit trajectories can occur at folds or anywhere along a slow segment on the repelling sheet of the critical manifold. The slow trajectory segments are contained in invariant manifolds that are approximated by invariant manifolds appearing in the singular limit $\varepsilon \to 0$ of the system. These invariant manifolds provide a substrate for our theoretical analysis of the homoclinic orbits in Section 2.10.

When $\varepsilon > 0$, the unstable manifold W^u and the repelling slow manifold S^r_ε are each two-dimensional, so they can intersect transversally along a trajectory. Moreover, W^u contains segments aligned with the unstable foliation of S^r_ε beginning where its trajectories jump from S^r_ε. Tiny variations in initial conditions on W^u yield trajectories that turn abruptly at different heights, as illustrated in Fig. (2.2). This fast portion of W^u turns again to follow S^{a-}_ε exponentially closely, then jumps to S^{a+}_ε and follows this manifold to the twist region. The singular limits of these transitions are given by smooth one-dimensional maps whose composition with one another maps a segment of W^u to a section of S^{a+}_0 that passes through the folded node.

We are interested in studying the singular limit of a system for which the equilibrium point is a saddle-focus that remains ε-close to the folded singularity. These conditions can be satisfied only when the distance from the equilibrium point to the fold scales with ε: in the system (3.2), this implies $\nu = O(\varepsilon)$. In

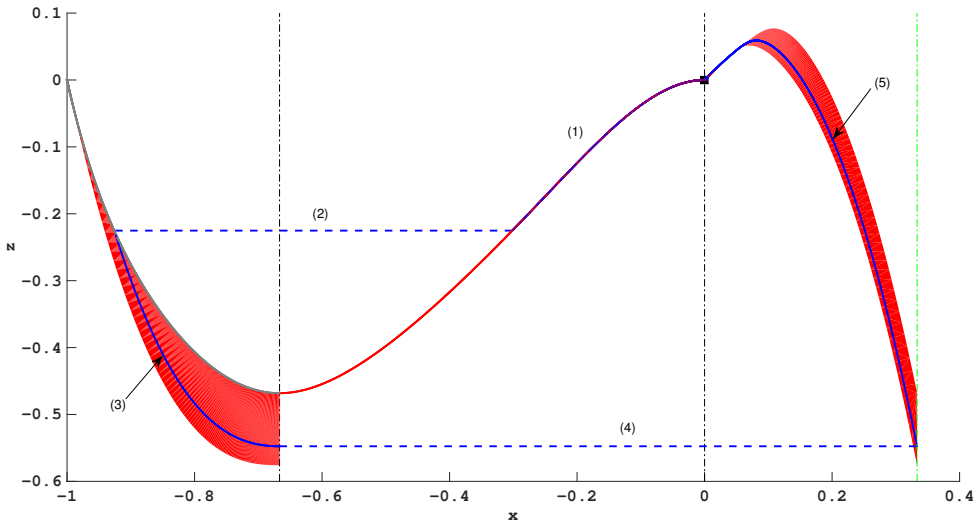

Figure 2.9: Nonunique singular cycles of the desingularized reduced system (2.8). Recall that stability is reversed on S_0^r, the region $-2/3 < x < 0$, because of the time reparametrization used to desingularize the reduced system. A typical cycle in this family contains trajectories on C (blue solid curves) and jumps (blue dashed curves): (1) a segment of the unstable manifold of the folded saddle-node (0,0), (2) a jump to S_0^{a-}, (3) a segment of a trajectory flowing forward on S_0^{a-} to the left jump curve at $x = -2/3$, (4) a jump to S_0^{a+} ending on the green dashed line $\{x = 1/3\}$, (5) a trajectory segment on S_0^{a+} connecting the end of this jump to the folded node at (0,0). The slow segments of all the singular homoclinic orbits lie in the red regions. Parameter set is $(\nu, a, b, c) = (0, a_\beta, b_\beta, c_\beta)$, where subscripted parameters are defined in Fig. 2.6

.

particular, when $\nu = \varepsilon = 0$ the origin is an equilibrium point of the full system that is a folded saddle-node, type II. Summarizing, the singular limit of the homoclinic orbits can be decomposed as follows:

- An initial segment which lies in W^u within the repelling sheet S_0^r of the critical manifold.

- A jump from S_0^r to the attracting sheet S_0^{a-} of the critical manifold.
- A slow trajectory on S_0^{a-} that ends at the fold at $x = -2/3$.
- A jump from the fold of S_0^{a-} to S_0^{a+}.
- A slow trajectory that follows S_0^{a+} back to the saddle-node equilibrium at the origin.

We reemphasize here that slow trajectories are defined for the reduced system (2.8) at an FSN II bifurcation. The saddle-node point of this system has a single unstable separatrix and a two dimensional stable manifold with boundary. This creates a lack of uniqueness in the singular limit as shown in Fig. (2.9). In the reduced system, trajectories that jump from the unstable manifold to S_0^{a-} continue to the fold curve $x = -2/3$ where they jump to points lying in the stable manifold of the saddle-node. Jumps from the unstable manifold of the saddle-node that occur anywhere on S_0^r yield trajectories that return to the saddle-node. However, when $\varepsilon > 0$, the geometry near the equilibrium becomes much more complicated. The equilibrium has a one dimensional stable manifold, and this manifold intersects the attracting slow manifold S_ε^{a+} only for parameters lying in a codimension one manifold of the parameter space. Moreover, S_ε^{a+} may twist around the stable manifold near the location of a folded-node in the reduced system. Section 2.10 investigates the persistence of each of the transitions between segments of the singular homoclinic orbit as ε becomes positive. Establishing persistence requires transversality hypotheses that are formulated there.

2.9 Geometry and returns of the twist region

We now turn to a study of the return map to a suitably chosen cross-section near the Shilnikov homoclinic orbit we have found. The classical analysis of Shilnikov begins with a homoclinic orbit of a three-dimensional vector field that has a very special form. First, it is assumed that the vector field is linear in a neighborhood U of an equilibrium p and that the eigenvalues $\lambda, \rho \pm i\omega$ at p satisfy $|\rho/\lambda| < 1$. Cross-sections Σ_1 and Σ_2 are chosen in U, and the flow map from Σ_1 to Σ_2 is computed explicitly. The second assumption is that the "global return" from Σ_2 back to Σ_1 is an affine map. The return map obtained by composing these two flow maps is then proved to have hyperbolic invariant sets. Since hyperbolic invariant sets persist under perturbation of the vector field, homoclinic orbits of vector fields that do not have this special form still have nearby hyperbolic invariant sets. In particular, the Shilnikov analysis applies to the homoclinic orbits of (3.2) with the parameter set β (as in Fig. 2.6). However, we expect that two aspects of the slow-fast structure of (3.2) may significantly distort the "standard" Shilnikov return map: (1) the twist region may introduce additional twisting of the flow near the homoclinic orbit, and (2) the strong attraction and repulsion to the slow manifolds might make the global return map from Σ_2 to Σ_1 almost singular. We investigate these issues, producing modifications of the Shilnikov return map suitable for the homoclinic orbits we have located in (3.2).

We consider the parameter set β (as in Figure 2.6) and analyze the returns of a thin strip Σ near $S_\varepsilon^{a+} \cap \{z = 0\}$. Exponential contraction of the flow onto S_ε^{a+} suggests that Σ may be mapped into itself in the vicinity of its intersection with the homoclinic orbit. Numerical computations suggest that this does happen

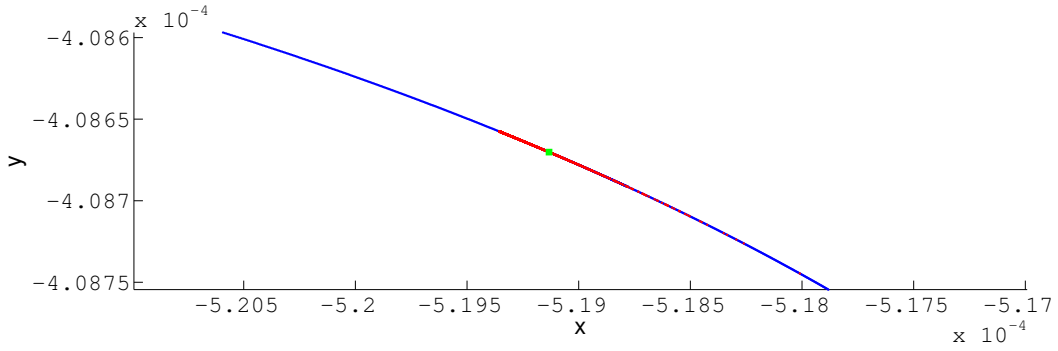

Figure 2.10: A segment of S_ε^{a+} on $\{z = 0\}$ (blue curve) and its first return (red points). The first intersection of W^s with $\{z = 0\}$ is depicted by the green square. Parameter set is β.

(Figure (2.10)). Approximating Σ by a small segment I parameterized by the x-coordinate, the corresponding one-dimensional approximation to the return map $R : I \to I$ reveals complicated dynamics (Figure 2.11(a)). In particular, we find a sequence of fixed points in steep portions of the map R that accumulate at the homoclinic orbit intersection. This agrees with previous analyses of homoclinic orbits to spiraling equilibrium points that identified a countable number of periodic orbits of decreasing Hausdorff distance to the Shilnikov homoclinic orbit [33, 80]. The novel behavior here is that these fixed points lie in steep portions of the return map whose trajectories contain canard segments (Figure 2.11(b)). These periodic orbits may have a few additional twists (small-amplitude oscillations) associated with reinjection into the twist region, in addition to the spiraling local to the equilibrium point.

An issue of concern is whether the twisting inside twist regions significantly distorts the return map. We explore this issue by comparing the geometry we find in the twist region with what is known about the twisting of slow manifolds in twist regions. In order to make this comparison, we must briefly revisit the slow flow equations.

In studies of the folded node normal form, Benoît [6] and Wechselberger [89] relate the ratio of eigenvalues $\mu = w_1/w_2$ of the folded node in the reduced system to the number of intersections of the (extended) attracting and repelling slow manifolds. The number j of intersections is estimated by the formula $j = 1 + [(\mu - 1)/2]$, and this also estimates the maximal number of small oscillations of trajectories passing through the twist region in the full system. As further elucidated by Krupa and Wechselberger [61], this estimate breaks down when the folded node is too close to a folded saddle-node. Here, the folded node is too close because $\nu = O(\varepsilon)$ while the results of Krupa and Wechselberger [61] require that $\nu = O(\varepsilon^{1/2})$ or larger. Nonetheless, we use the value of μ as a guide for our numerical investigations.

In the present instance, the folded node of our reduced system equations (2.8) has eigenvalues $w_1 \approx -0.920102$ and $w_2 \approx -0.0798982$ at the parameter set β. Thus we estimate $j = 1 + [(11.5159 - 1)/2] = 6$. However, since the equilibrium point lies in the intersection of the extended slow manifolds, S^r_ε has an infinite number of turns that yield a countable number of intersections with S^a_ε (Figure 2.12). Although the twist region serves to strongly contract volumes of the phase space, the equilibrium point produces the large numbers of small-amplitude oscillations. It seems that the twisting inside the twist region does not contribute significantly to the geometry of the return map near the homoclinic orbit.

Since trajectories beginning in I have canard segments when I intersects S^r_ε, we examine the resulting distortion by focusing on a section closer to the equilibrium point. Figure 2.13 shows not only that I intersects S^r_ε countably many times near the equilibrium point but also that canard lengths of forward trajectories are organized smoothly in neighborhoods of S^r_ε. The property of countable

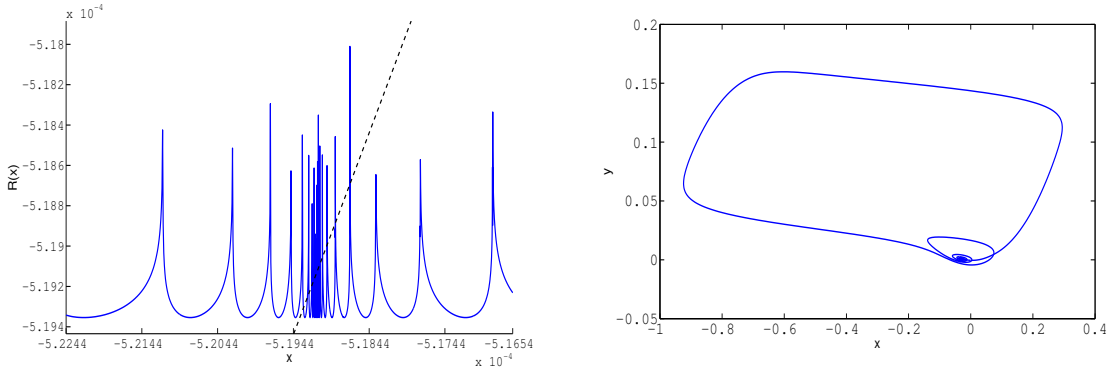

(a) (b)

Figure 2.11: (a) The return map R of points in I, where both $(x, y) \in I$ and $R(x, y) \in R(I)$ are parametrized by their x-coordinates. Points $(x, R(x))$ lie on the solid blue curve, and the fixed points that also lie on the line $x = R(x)$ (dotted black) belong to periodic orbits that intersect the cross section $z = 0$ just once. (b) Periodic orbit corresponding to the fixed point $p \approx -5.18996 * 10^{-4}$ of the map R. Parameter set is β.

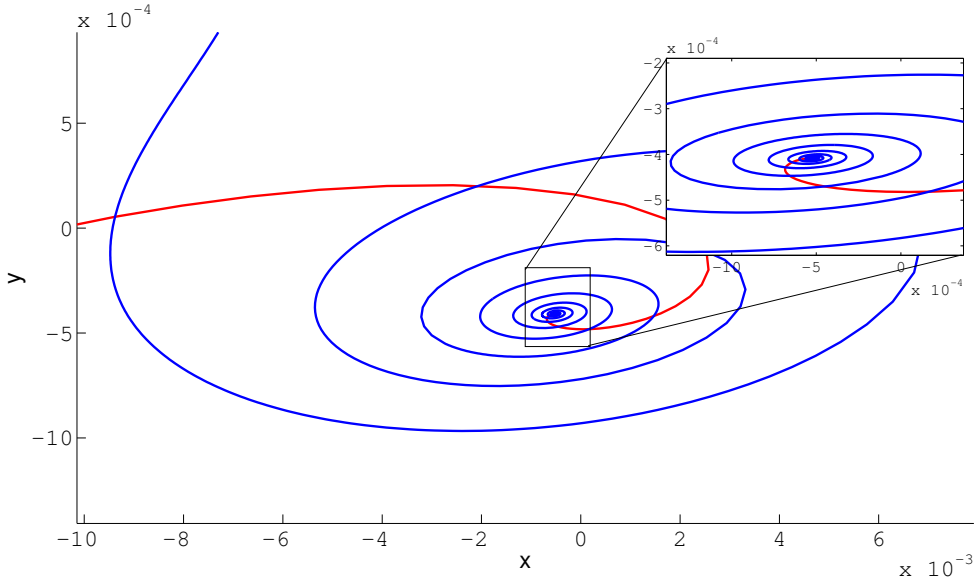

Figure 2.12: Intersection of the extensions of S^a_ε (red) and S^r_ε (blue) in the section $\{z = 0\}$. Inset shows magnification of spiraling of S^r_ε near the first intersection of W^s with $\{z = 0\}$. Parameter set is β.

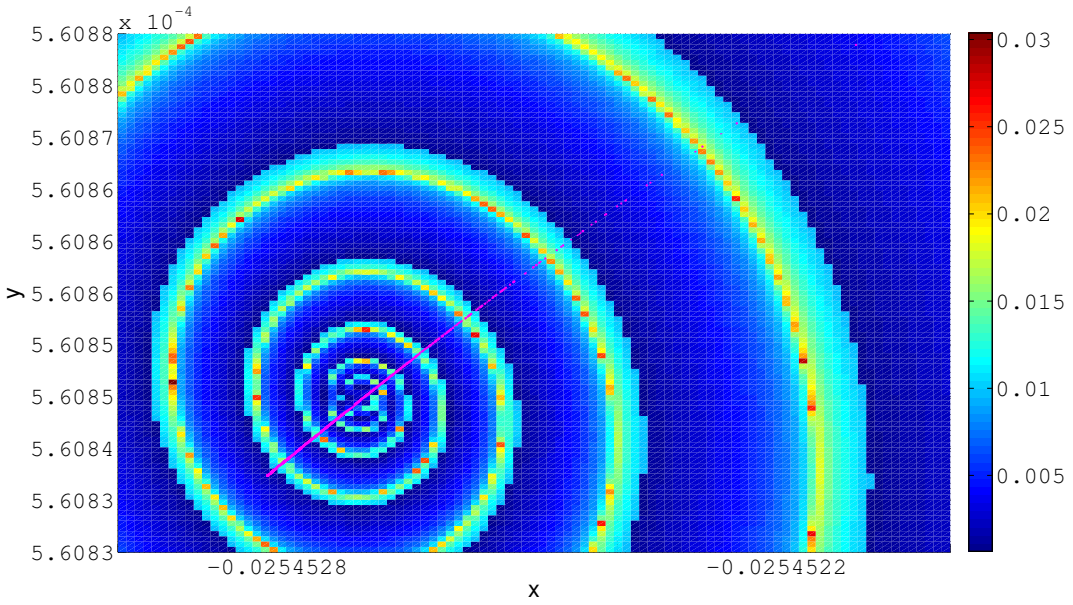

Figure 2.13: Intersection of I (purple) with S^r_ε in the cross-section $\{z = -0.025\}$. Color values denote heights (y-values) attained by trajectories beginning in a 100×100 grid of initial conditions $(x, y, -0.025)$, where $x \in [-0.025453, -0.025452]$ and $y \in [5.6083 * 10^{-4}, 5.6088 * 10^{-4}]$. Stopping conditions are $x = -2/3$ and $y = x^2 + x^3 \pm 0.004$. Heights computed from projection of trajectory endpoint onto the critical manifold $\{y = x^2 + x^3\}$. Parameter set is β.

intersections is explained by the "local" Shilnikov map (in reverse time) applied to initial points in S^r_ε. Backward trajectories flowing past the equilibrium point spiral very close to W^s by the time the trajectory exits a neighborhood of the equilibrium. The distribution of canard segment lengths implies that the return map of I stretches and folds subsets depending on how the subsets straddle the spiral of the repelling slow manifold.

We get additional insight into the return map using arguments that resemble the Exchange Lemma [54]. This result analyzes the Jacobian of a flow map for trajectories that jump from a slow manifold of saddle type along its unstable

manifold. Consider the two-dimensional system

$$\begin{aligned} \varepsilon \dot{x} &= 1 \\ \dot{y} &= \lambda y. \end{aligned}$$

The flow map of this system from the section $x = 0$ to the section $y = 1$ is given by $x(1) = \frac{-1}{\lambda} \log y(0)$, with derivative $(\frac{-1}{\lambda y(0)}) = \frac{-1}{\lambda} \exp(-\lambda x(1))$. Note that this derivative grows exponentially with the distance a trajectory flows along the slow repelling manifold. For us, this is a source of stretching in the global return map of the system (3.2). We consider trajectories in W^u near S^r_ε that jump to S^{a-}_ε. The arrival points of these curves can be projected onto S^{a-}_ε along its strong stable foliation. So long as this projection is transverse to the trajectories on S^{a-}_ε, the stretching that comes from the varying jump points on S^r_ε is maintained. Similarly, jumps from S^{a-}_ε to S^{a+}_ε, projected onto S^{a+}_ε along its strong stable foliation, sweep out a curve on S^{a+}_ε. If this curve is transverse to the flow on S^{a+}_ε, the stretching in the global return is once again maintained.

Of course, there is also fast contraction to the attracting manifolds as well. Unless contraction of the flow along S^{a+}_ε in the folded node region dominates the stretching originating along S^r_ε, we can expect the global return map to be approximately a rank one map of large norm for the trajectories that have longer canards. This is apparent in the spikes of Figure 2.11.

We now verify the claim that stretching is maintained in the global return map. Fix two compact, planar cross-sections Σ_0 and Σ_1, transverse to W^u and W^s, respectively. The global return map $R : \Sigma_0 \to \Sigma_0$ can then be decomposed into the two maps $\varphi : \Sigma_0 \to \Sigma_1$ and $\psi : \Sigma_1 \to \Sigma_0$, so that $R = \psi \circ \varphi$. Points beginning in Σ_1 make small oscillations around W^s before spiraling out along W^u and hitting Σ_0. Later, we give an analytical approximation of the local map

ψ.

We compute $D\varphi(p)$ with central differences, where p is a 10^{-10} perturbation of the point where the homoclinic orbit intersects Σ_0. The matrix $D\varphi(p)$ has singular values $\sigma_1 \approx 1.53064$ and $\sigma_2 \approx 2.66223 * 10^{-7}$, indicating that the global part of R is close to rank one due to strong contraction onto the attracting slow manifolds.

The Jacobian $D\psi$ of the local part of the return map is approximated analytically. First, transform coordinates with the real Jordan form $P^{-1}JP = J'$, where J is the Jacobian of (3.2) at p_{eq}. We denote transformations of variables x, maps ζ, and subsets Σ by primes x', ζ', and Σ'. Thus, the unstable subspace of p_{eq} becomes parallel to the $x'y'$-plane, and the stable subspace becomes parallel to the z'-axis. Following Shilnikov, $\psi' : \Sigma_1' \to \Sigma_0'$ and its derivative $D\psi'$ are approximated explicitly from the normal form of the spiraling equilibrium point:

$$\psi'(x', y') \;=\; (re^{\rho\theta/\omega}, de^{-\lambda\theta/\omega}), \tag{2.9}$$

where $r = \sqrt{x'^2 + y'^2}$, $\tan\theta = y'/x'$, and d is a small, fixed height of Σ_1' above $(0, 0, 0)$.

We recover the Jacobian $D\psi$ by transforming $D\psi'$ to the original coordinates on the cross-sections $\Sigma_{0,1}$. By the chain rule, we have $DR(p) = D\psi(\varphi(p)) \circ D\varphi(p)$, with eigenvalue magnitudes $|\lambda_1| \approx 80166$ and $|\lambda_2| \approx 2 * 10^{-16}$. We have not tried to confirm the relative accuracy of the small eigenvalue, but clearly it is very small. Note also that the stretching factor in the local map can be shown to become unbounded by picking points approaching the stable manifold on Σ_1 and a sequence of cross-sections Σ_0 with decreasing heights. These points spiral out along the unstable manifold. The number m of turns that the trajectory makes before intersecting Σ_0 determines the appropriate solution of the multivalued

function $\theta = \arctan(y'/x') + 2m\pi$ in (2.9). The effect on the resulting Jacobian matrix $D\psi'$ is multiplication by a diagonal matrix with entries $e^{2m\pi\rho/\omega}$ and $e^{-2m\pi\lambda/\omega}$, both of which are larger than 1.

2.10 A geometric model of Shilnikov homoclinic orbits

This section abstracts our analysis of the Shilnikov homoclinic orbit in the Koper model with a list of geometric conditions that are sufficient to prove the existence of such homoclinic orbits in slow-fast systems. In the context of this geometric model, the previous sections can be regarded, retrospectively, as numerical evidence that these conditions are satisfied along a particular curve of parameter values parametrized by ε in the Koper model.

The geometric model is formulated in terms of a three-dimensional slow-fast vector field X_ε with two slow variables and one fast variable that depends on additional parameters. Our first hypothesis is that the reduced system X_0 (without desingularization) has singular cycles like those shown in Fig. 2.9:

Singular Cycles Hypothesis:

- The reduced vector field X_0 has an S-shaped critical manifold with sheets S^{a-}, S^r and S^{a+} separated by fold curves L^- and L^+. $S^{a-}$and S^{a+} are attracting while S^r is repelling. The folds are generic.
- X_0 has a folded saddle-node p_{eq}. This point lies on a curve of equilibrium points for the full system X_ε that are saddle-foci for $\varepsilon > 0$.
- Beginning at p_{eq}, the singular cycles consist of

1. a segment of the unstable manifold W^u lying entirely in S^r,
2. a jump from W^u to S^{a-},
3. a segment that flows along S^{a-} to L^-,
4. a jump from L^- to S^{a+}, and
5. a segment that flows along S^{a+} back to p_{eq}.

- Following jumps from L^- to S^{a+}, all of the points of S^{a+} from candidates following the first four steps of this process form a curve K lying in the basin of attraction of p_{eq}.

Remark: In the Koper model and other slow-fast systems with an FSNII bifurcation, the equilibrium point is a focal saddle only when it is $O(\varepsilon)$- distant from the FSNII point. Thus the second item in this hypothesis implies that the distance from the equilibrium to the twist region of the system scales with ε. System (3.2) satisfies this scaling hypothesis along a curve obtained by setting $\nu = \varepsilon\bar{\nu}$ and using $\bar{\nu}$ as a parameter which is fixed when letting $\varepsilon \to 0$.

Proving the persistence of the singular cycles requires additional hypotheses that are expressed in terms of transversality. We continue to refer to the repelling and attracting slow manifolds that perturb from the sheets S^r and $S^{a\pm}$ for $\varepsilon > 0$ as S^r_ε and $S^{a\pm}_\varepsilon$.

Transversality Hypotheses:

- In the singular limit, the image of the jump curve from W^u to S^{a-} is transverse to the vector field of the reduced system.
- Similarly, the curve K defined above is transverse to the vector field of the reduced system on S^{a+}.

- For $\varepsilon > 0$ small, the unstable manifold of the equilibrium point p_{eq} intersects the repelling slow manifold S^r_ε transversally in a trajectory γ_ε.
- In the four-dimensional extended phase space that includes a parameter λ, the stable manifolds of p_{eq} sweep out a two-dimensional surface as λ is varied. This surface intersects the three-dimensional attracting slow manifold transversally along a trajectory β_ε. For each $\varepsilon > 0$, β_ε only exists for a particular parameter value $\lambda = \lambda_h(\varepsilon)$.
- The trajectories β_ε have a limit as $\varepsilon \to 0$. This limit intersects the curve K defined above.

Remark: The last item in this list of hypotheses has not been investigated thoroughly. Systems with an FSNII bifurcation can be rescaled so that the system has a regular limit as $\varepsilon \to 0$ [36, 43]. We think that the intersections of W^s and S^{a+}_ε that we have analyzed in this paper scale nicely with variations of ε when the remaining parameters are suitably scaled, but have little evidence to substantiate this presumption. The small-amplitude dynamics associated with FSNII bifurcations have not yet been studied systematically.

We now state our main theorem about the geometric model:

Theorem 2 *Let X_ε be a slow-fast vector field with two slow variables and one fast variable that depends upon an additional parameter λ. If X_0 satisfies the singular cycle hypothesis, and if X_ε satisfies the tranversality hypotheses, then there is an $\varepsilon_0 > 0$ so that for each $0 < \varepsilon < \varepsilon_0$, there is a value of $\lambda = \lambda(\varepsilon)$ for which X_ε has a homoclinic orbit.*

Outline of proof: Define a cross-section Σ_J orthogonal to the fast direction in the middle of jumps from L^- to S^{a+}. Denote by L^J the curve on Σ_J that projects

onto L^- along the fast direction. Since homoclinic orbits are formed by branches of the stable manifold of p_{eq}, we prove the theorem by starting at p_{eq} and following its stable manifold W^s backward in time. There are intervals of λ near $\lambda_h(\varepsilon)$ for which the jump points of W^s from S_ε^{a+} cross K. The fast segments of these jumps intersect Σ_J in a smooth curve A. Projection of A to S_ε^{a+} along its fast foliation gives a curve that is close to a trajectory of the reduced system on S^{a+}. The second transversality hypothesis implies that L^J and A are transverse.

Now return to p_{eq} and follow trajectories of its unstable manifold W^u until they jump to S_ε^{a+}. An exponentially thin wedge of angles in W^u gives trajectories that follow S_ε^r for varying distances, jumping to S_ε^{a-} along strong unstable manifolds of S_ε^r. These trajectories turn to follow S_ε^{a-} where trajectories are approximated by trajectories of the reduced system. The first transversality hypothesis implies that the width of this strip of trajectories, measured orthogonal to the flow direction, will be $O(1)$. When the strip reaches the vicinity of L^-, it jumps to S_ε^{a+}, intersecting Σ_J in a curve L_ε^J. By a classical result of Levinson [67], L_ε^J is C^1 close to L^J. Consequently, when $\varepsilon > 0$ is small enough, L_ε^J and A intersect transversally in Σ_J close to a point of Σ_J lying on a singular cycle. The point $L_\varepsilon^J \cap A$ lies on the homoclinic orbit, and the theorem is proved.

In addition to proving the existence of the homoclinic orbit, we want to use the arguments in Section 2.9 to analyze its return map and prove that there are chaotic invariant sets nearby. Moreover, these invariant sets contain MMOs with unbounded numbers of small amplitude oscillations in their signatures.

Theorem 3 *Let X_ε be a slow-fast vector field with two slow and one fast variable that depends upon an additional parameter λ. Assume that (1) X_0 satisfies the singular cycle hypothesis, (2) X_ε satisfies the tranversality hypotheses and (3) the equilibrium*

p_{eq} satisfies the Shilnikov condition $-\rho/\mu < 1$ for its eigenvalues $\rho \pm i\omega$ and μ when $\varepsilon > 0$. Then, there are chaotic invariant sets in any neighborhood of the homoclinic orbit of X_ε. These invariant sets include an infinite number of periodic orbits that make a single global return around the homoclinic orbit. The number of small amplitude oscillations in this set of periodic MMOs is unbounded.

Outline of proof: Let Σ_{fn} be a cross-section to X_ε in its folded-node region. We establish that its return map resembles Figure 2.11. Due to the strong contraction along S_ε^{a+}, this return map will be close to rank one with image aligned along $I = S_\varepsilon^{a+} \cap \Sigma_{fn}$. We study the returns of a thin strip $\bar{I}$ around $I \subset \Sigma_{fn}$ to Σ_{fn}. The intersection ξ of the stable manifold of p_{eq} with Σ_{fn} never returns. Shilnikov's original analysis [80] of the local flow map establishes (1) that points that approach ξ make increasing numbers of small-amplitude oscillations along W^u before flowing along S_ε^r, and (2) the Jacobian of the flow map has a direction with strong expansion. The arguments presented in section 2.9 show that this expanding direction becomes aligned with the vector field on S_ε^r as trajectories jump from S_ε^r to S_ε^{a-}. Arriving at S_ε^{a-}, our transversality hypotheses imply that the expanding direction retains a component transverse to the slow flow on S_ε^{a-}. The transversality hypotheses also imply that expansion transverse to the slow flow on S_ε^{a+} is preserved following the jump from S_ε^{a-} to S_ε^{a+}. When flowing along S_ε^{a+}, strong contraction compresses the image of $\bar{I}$ into an exponentially thin neighborhood of S_ε^{a+}. Thus when points of $\bar{I}$ return to Σ_{fn}, their Jacobian is nearly rank one but (by (2) above) with strong expansion along I.

As in Figure 2.11, the spiral formed as $\bar{I}$ flows past p_{eq} returns to Σ_{fn} with monotone branches that cut through $\bar{I}$. Each of these branches contains a fixed point at the intersection of a periodic MMO with Σ_{fn}, and the returns that remain

within a fixed set of n branches constitute hyperbolic invariant sets on which the return map is conjugate to the shift map on sequences of n symbols.

2.11 Concluding Remark

We have given a fairly complete description of a Shilnikov homoclinic orbit in the Koper model, and we have formulated abstract hypotheses that imply it occurs in a structurally stable bifurcation for sufficiently small ε_1. Our numerical investigations suggest that these hypotheses are satisfied.

The Koper model is only moderately stiff in the regime we investigated, raising the question as to whether the qualitative structure of the homoclinic orbits remains unchanged as one approaches the singular limit of the system. In response to this question, we performed a continuation of the singular Hopf normal form homoclinic orbit in Fig. (2.6) along a parametric path satisfying $\nu = \varepsilon\bar{\nu}$ with $\bar{\nu}$ fixed. On such a path, the distance from the saddle focus to the FSNII scales with ε. As ε decreases from 0.01 to approximately 0.003, the resulting picture agrees with our analysis of the reduced system (Eq. (2.8)): the Shilnikov orbits become better approximated by concatenations of slow trajectories on C with jumps across branches of C.

CHAPTER 3

TANGENCY BIFURCATION OF MIXED-MODE OSCILLATIONS

3.1 Abstract

Identifying routes toward *mixed-mode oscillations* (MMOs)—periodic solutions consisting of large- and small-amplitude oscillations—is a topic of active research. This paper concerns a recently catalogued bifurcation associated with the emergence of MMOs: the tangency of the unstable manifold of a unique equilibrium point with a repelling slow manifold. This tangency is fundamental because it functions as a 'switch' connecting different parts of the phase space via *slow manifolds*. However, this geometric characterization is not easily rephrased as a set of algebraic conditions. Furthermore, the flow in various regions of the phase space is complicated due to the simultaneous existence of various invariant objects, including a saddle-focus fixed point and a small-amplitude stable periodic orbit. Each of these objects plays a role in the formation of various types of MMOs.

The purpose of this analysis is twofold: first, we give a numerical exploration of some of the routes to complicated MMO signatures occurring after this bifurcation. This step is performed using bifurcation theory: we identify certain bifurcations in discrete return maps of the system at parameter values near to the tangency bifurcation, and translate these into statements about MMO transitions. These bifurcations are not sufficient to identify some of the more elusive transitions and MMO types, so we are led to the second part of the analysis: we construct a new dynamical partition of the domain of two-dimensional return maps in the system. This construction relies upon topological conditions which

are well-defined only when the parameter characterizing a timescale ratio in the dynamical system is sufficiently small. With the aid of this partition, we identify sets of unusual 'medium'-amplitude MMOs which occur as fixed points of a return map, and we also give numerical evidence of a Smale-Birkhoff homoclinic orbit as a route to chaotic MMOs. This partition construction should be compared to the identification of 'rotation sectors,' which have been used to organize less-complicated return maps of more elementary singular bifurcations.

3.2 Introduction

Mixed-mode oscillations (MMOs) are periodic solutions of a dynamical system containing large and small amplitude oscillations and a distinct separation between the two. These solutions may be characterized by their signatures, which are symbolic sequences of the form $L_1^{s_1} L_2^{s_2} \cdots L_k^{s_k}$. This notation is used to indicate that a particular solution undergoes L_1 large oscillations, followed by s_1 small oscillations, followed by L_2 large oscillations, and so on. The distinction between 'large' and 'small' oscillations is dependent on the model. We also refer to nontrivial, aperiodic, bounded solutions as MMOs. These include solutions having arbitrarily long, nonrepeating signatures. Such MMOs may be chaotic.

The classification of routes to MMOs with complicated signatures as well as chaotic MMOs continues to garner interest. Global bifurcations of multiple-timescale (or simply *slow-fast*) dynamical systems are natural starting points in this direction.

We study slow-fast dynamical systems of the form

$$\begin{aligned} \varepsilon \dot{x} &= f(x, y, \varepsilon) \\ \dot{y} &= g(x, y, \varepsilon), \end{aligned} \tag{3.1}$$

where $x \in R^m$ is the *fast* variable, $y \in R^n$ is the *slow* variable, $\varepsilon > 0$ is the *singular perturbation parameter* that characterizes the ratio of the timescales, and f, g are sufficiently smooth. The *critical manifold* $C = \{f = 0\}$ is the manifold of equilibria of the fast subsystem defined by $\dot{x} = f(x, y, 0)$. When ε is sufficiently small, theorems of Fenichel[32] guarantee the existence of locally invariant *slow manifolds* that perturb from subsets of C where the equilibria are hyperbolic. We may also project the vector field $\dot{y} = g(x, y, 0)$ onto the tangent bundle TC. Away from folds of C, we may desingularize this projected vector field to define the *slow flow*. The desingularized slow flow is oriented to agree with the full vector field near stable equilibria of C. For sufficiently small values of ε, trajectories of the full system can be decomposed into segments lying on the slow manifolds near C together with fast jumps across branches of C. Trajectory segments lying near the slow manifolds converge to solutions of the slow flow as ε tends to 0.

In the case of two slow variables and one fast variable ($m = 1$, $n = 2$), C is two-dimensional and its folds form curves. Selected points on fold curves are called *folded singularities*. When the slow flow is two-dimensional we use the terms "folded node", "folded focus", and "folded saddle" to denote folded singularities of node-, focus-, and saddle-type, respectively. In analogy to classical bifurcation theory, folded saddle-nodes are folded singularities having a zero eigenvalue. These are classified according to their persistence as equilibria in the full system of equations; folded-saddle nodes of type II (FSNII) are true equilibria of the full system. At a *singular Hopf bifurcation*, a pair of eigenvalues

of the linearization of the flow crosses the imaginary axis, and a small-amplitude periodic orbit is born at the bifurcation point. These are shown to occur generically at $O(\varepsilon)$-distances from the FSNII in parameter space.[37]

Characterizing the behavior near a folded singularity has been the subject of intense study. In the case of a folded node, Benoît[7] and Wechselberger[90] observed that the maximum number of small oscillations made by a trajectory passing through the folded node region can be counted using the ratio of eigenvalues of the linearization near the folded node. Guckenheimer[36] has also analyzed the local flow maps and global return maps of normal forms exhibiting folded nodes and folded saddle-nodes, showing that such folded singularities can give rise to complex and chaotic behavior.

In a complementary direction, period-doubling cascades, torus bifurcations,[37] and more recently, Shilnikov homoclinic bifurcations[42] have been shown to produce MMOs with complex signatures. Even so, the connection between these bifurcations and interactions of slow manifolds—which organize the global dynamics for small values of ε—remains poorly understood.

In this paper, we study a minimal example of a slow-fast three-dimensional system having a so-called "S-shaped" critical manifold. Parametric subfamilies of this dynamical system have served as important prototypical models of electrochemical oscillations.[60]

Our focus is a tangency bifurcation catalogued by Guckenheimer and Meerkamp.[44] This tangency is important in the context of MMOs. In our system, there exist several mechanisms which can generate large and small oscillations: folded singularities and a saddle-focus equilibrium point are *local* mech-

anisms which generate small-amplitude twisting of orbits, and an S-shaped critical manifold allows repeated reinjection into these local regions via large-amplitude excursions. There is also a parametric family of stable periodic orbits emerging from the saddle-focus, which generate additional twists around the stable manifold of the saddle-focus.

Before the tangency has occurred, the small- and large-amplitude mechanisms are 'disconnected' by the basin of attraction of the periodic orbit, in the sense that nontrivial trajectories not lying in the basin of attraction escape to infinity. The tangency bifurcation suddenly 'connects' these mechanisms together via bands of trajectories, allowing MMOs to form (see Fig. 3.1). We expect that aspects of this geometric analysis will remain relevant for any sufficiently low-dimensional, smooth slow-fast system whose critical manifold is S-shaped in a local region of the phase space.

Another reason why this bifurcation is interesting is that there is an interplay of *several* local mechanisms which produce twisting behavior. The delicate analytic arguments used to study twists near isolated folded singularities, or near saddle-foci, do not easily generalize to produce an accurate global analysis. We are left with numerical approximation of return maps to illuminate key features of the bifurcation.

Due to strong phase space contraction towards *attracting* slow manifolds of the system, it is possible to approximate return maps on cleverly chosen cross-sections with one-dimensional maps on an interval. We show that such maps are characterized by wildly varying derivatives and nonzero-length gaps which may be characterized as escape sets, corresponding to orbits which lie in the basin of attraction of the stable periodic orbit. The fixed points of these maps

correspond to MMOs of the full system; however, the one-dimensional approximation gives limited information about the types of MMOs that emerge. To further understand how these large and small oscillations connect, we must turn to two-dimensional return maps defined on cross-sections near to the equilibrium point and folded singularity. We show that the return dynamics, although highly nonlinear with regions of immense stretching and contraction as well as escape regions, are nonetheless organized by the slow manifolds of the system, together with the stable manifold of the equilibrium point and the periodic orbit's basin of attraction.

Our goal is to understand transitions of small to large oscillations. This requires disentangling the relative influence of the folded singularity versus the saddle-focus. Our approach is to partition the domain of the return map depending not only on the number of small turns the corresponding trajectories make—a technique which has been used previously to draw 'rotation sectors' of return maps in other slow-fast problems—but also on the direction of the jump from the repelling slow manifold. We argue that this partition is able to accurately distinguish between the various small-amplitude mechanisms, which is a new step forward for slow-fast systems of this type. For example, we show that the small oscillations of trajectories jumping right are characteristic of twists due to a folded node, whereas small oscillations of trajectories jumping left spiral out along the unstable manifold of the saddle-focus. Trajectories jumping left or right also return to the cross-section very differently, giving us more confidence that this partition isn't spurious.

The remainder of this paper is organized as follows.

- In Sec. 3.3, we define the three-dimensional slow-fast system and describe

the dynamics near the tangency bifurcation at a broad level.

- In Sec. 3.4, we define one-dimensional approximations to return maps and describe saddle-node bifurcations and period-doubling cascades of MMOs. We also describe the statistics of the return map at a parameter set within a chaotic window of the period-doubling sequence.
- In Sec. 3.5, we define a return map on a two-dimensional cross-section. We use the slow manifolds and the basin of attraction of the small-amplitude periodic orbit as guides to create a partition according to the turning behavior of trajectories with initial conditions on that cross-section. We define a symbolic map encoding the return dynamics of partition subsets, and use this to streamline the discussion by giving concrete constructions of MMOs with varying symbolic dynamics. We also identify a Smale-Birkhoff homoclinic orbit, giving rise to a full-shift over a finite set of symbols and return horseshoes. We give numerical evidence that this chaotic invariant set may be a chaotic attractor of the full system.

3.3 Defining the tangency bifurcation

We study the following three-dimensional flow:

$$\begin{aligned} \varepsilon \dot{x} &= y - x^2 - x^3 \\ \dot{y} &= z - x \\ \dot{z} &= -\nu - ax - by - cz, \end{aligned} \tag{3.2}$$

where x is the fast variable, y, z are the slow variables, and $\varepsilon, \nu, a, b, c$ are the system parameters. This system exhibits a singular Hopf bifurcation.[15, 37, 45]

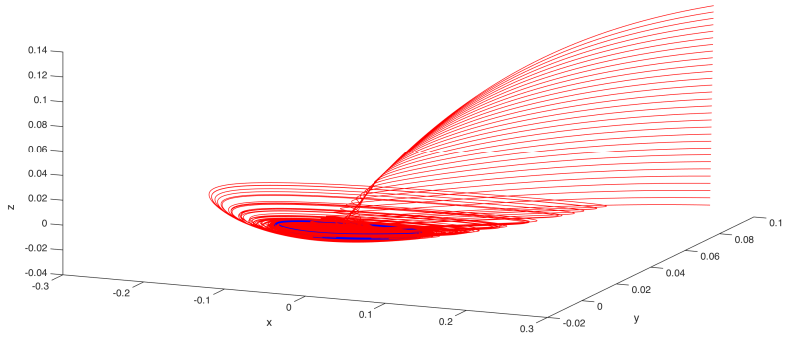

(a)

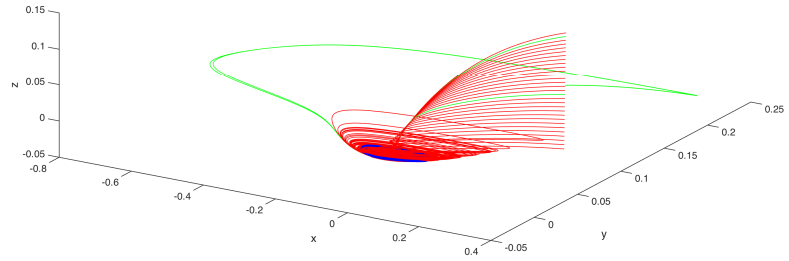

(b)

Figure 3.1: Phase space (a) just before ($\nu = 0.00647$) and (b) just after ($\nu = 0.00648$) tangency bifurcation of W^u with S^r_ε. Thirty trajectories are initialized in a band on Σ_+. Blue curve: small-amplitude stable periodic orbit Γ. Red curves: forward trajectories tending asymptotically to Γ without jumping to S^{a-}_ε. Green curves: forward trajectories making a large-amplitude excursion before returning to Σ_+. Remaining parameters are $\varepsilon = 0.01$, $a = -0.3$, $b = -1$, $c = 1$.

The critical manifold is the S-shaped cubic surface $C = \{y = x^2 + x^3\}$ having two fold lines $L_0 := S \cap \{x = 0\}$ and $L_{-2/3} := S \cap \{x = -2/3\}$. When $\varepsilon > 0$ is sufficiently small, nonsingular portions of C perturb to families of slow manifolds: near the branches $S \cap \{x > 0\}$ (resp. $S \cap \{x < -2/3\}$), we obtain the *attracting slow manifolds* S^{a+}_ε (resp. S^{a-}_ε) and near the branch $S \cap \{-2/3 < x < 0\}$ we obtain the *repelling slow manifolds* S^r_ε. Nearby trajectories are exponentially attracted

toward $S_\varepsilon^{a\pm}$ and exponentially repelled from S_ε^r. One derivation of these estimates uses the Fenichel normal form.[56] Within each family, these sheets are $O(-\exp(c/\varepsilon))$ close,[56, 55] so we refer to any member of a particular family as 'the' slow manifold. This convention should not cause confusion.

We focus on parameters where forward trajectories beginning on S_ε^{a+} interact with a 'twist region' near L_0, a saddle-focus equilibrium point p_{eq}, or both. A folded singularity $n = (0,0,0) \in L_0$ centers this twist region. The saddle-focus p_{eq} has a two-dimensional unstable manifold W^u and a one-dimensional stable manifold W^s. This notation disguises the dependence of these manifolds on the parameters of the system.

3.3.1 Tangency bifurcation of S_ε^r with W^u

Guckenheimer and Meerkamp[44] drew bifurcation diagrams of the system (3.2) in a two-dimensional slice of the parameter space defined by $\varepsilon = 0.01$, $b = -1$, and $c = 1$. Codimension-one tangencies of S_ε^r and W^u are represented in Fig. 5.1 of their paper by smooth curves (labeled T) in (ν, a) space. For fixed a and increasing ν, this tangency occurs after p_{eq} undergoes a supercritical Hopf bifurcation. A parametric family of stable limit cycles emerges from this bifurcation. Henceforth we refer to 'the' small-amplitude stable periodic orbit Γ to mean the corresponding member of this family at a particular parameter set, and $B(\Gamma)$ refers basin of attraction. The three-dimensional stable manifold of Γ interacts with the other invariant manifolds of the system. We will show that $B(\Gamma)$ has a significant influence on the global returns of the system.

Fixing $a = -0.03$, the tangency occurs within the range $\nu \in [0.00647, 0.00648]$.

The location of the tangency may be approximated by studying the asymptotics of orbits beginning on S_ε^{a+}. Fix a section $\Sigma_+ = S_\varepsilon^{a+} \cap \{x = 0.27\}$. Before the tangency occurs, trajectories lying on and sufficiently near W^u must either escape to infinity or asymptotically approach Γ; these trajectories cannot jump to the attracting branches of the slow manifold, as they must first intersect S_ε^r before doing so. Trajectories beginning in Σ_+ first flow very close to p_{eq}. As shown in Fig. 3.1, these trajectories then leave the region close to W^u. Before the tangency, W^u forms a part of the boundary of $B(\Gamma)$. Therefore, all trajectories sufficiently high up on S_ε^{a+} must lie inside $B(\Gamma)$ (Fig. 3.1(a)).

After the tangency has occurred, W^u and S_ε^r will generically intersect transversely along isolated trajectories. These trajectories will bound sectors of trajectories that can now make large-amplitude passages. Trajectories within these sectors jump 'to the left' toward S_ε^{a-} or 'to the right' toward S_ε^{a+}. Trajectories initialized in Σ_+ that leave neighborhoods of p_{eq} near these sectors contain *canards*, which are segments lying along S_ε^r. Examples of such trajectories are highlighted in green in Fig. 1. We can now establish a dichotomy between those trajectories in Σ_+ that immediately flow into a neighborhood of Γ and never leave, versus those that make a global return to Σ_+. In Fig. 3.1(b), only two of the thirty sample trajectories are able to make a global return. Note however that such trajectories might still lie inside $B(\Gamma)$, depending on where they return on Σ_+.

We will be interested in the transient dynamics of such trajectories, whose initial conditions are defined on cross-sections like Σ_+. Therefore, if Σ is any fixed cross-section in the phase-space and ϕ^t is the flow of the dynamical system, we define the *immediate basin of attraction* $B_0 = \{x \in \Sigma : \phi^t(x) \cap \Sigma = \emptyset$ for all

$t > 0\}$. Note that $B_0 \subset B(\Gamma)$ and that this notation also disguises the dependence on Σ. This convention will not cause confusion.

We say that a trajectory γ ($\gamma(0) \in \Sigma$) *escapes from* Σ if there exists a minimal $s > 0$ such that $\gamma(s) \in B_0(\Gamma)$. In terms of discrete return maps $R : \Sigma \to \Sigma$, this is equivalent to the condition that there exists a minimal $n \in \mathbb{Z}^+$ such that $R^n(\gamma(0)) \in B_0$. We end this section by addressing a possible confusion in our terminology: trajectories in B_0 have technically become 'trapped' by Γ— but our analysis in this paper is always concerned with the dynamics of return maps defined on cross-sections positioned away from neighborhoods of Γ, hence our use of the term 'escaping' and not 'trapping.'

3.4 One Dimensional Return Maps

The return map $R : \Sigma_+ \to \Sigma_+$ is well-approximated by a rank-one map on an interval, also denoted R. Our approach in studying the dynamics of R is similar to the analysis performed for return maps near folded nodes[90] and folded saddle-nodes.[36, 62] In those cases, rotation sectors partitioning the domain of the return map are identified. These components, arising from the twisting that occurs near a folded singularity, classify trajectories according to the number of small turns they make.[90]

In the present case there is a folded singularity, a saddle-focus, and a small-amplitude periodic orbit; each of these local objects plays a role in the twisting of trajectories that enter neighborhoods of the fold curve L_0. The remainder of this section carries out three tasks:

(a)

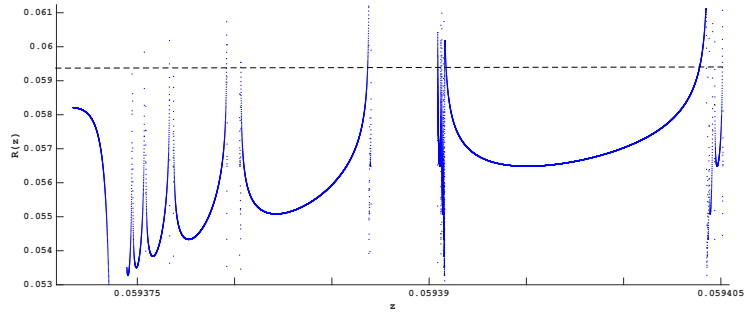

(b)

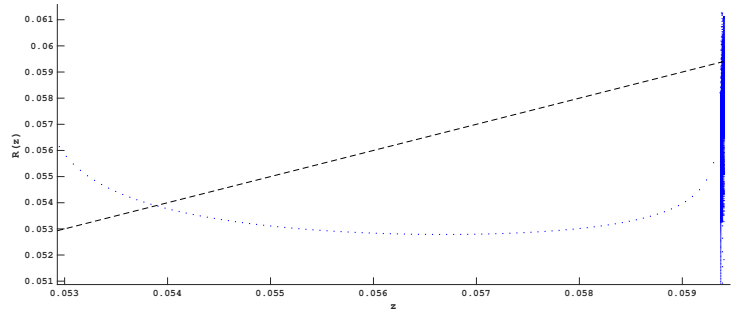

(c)

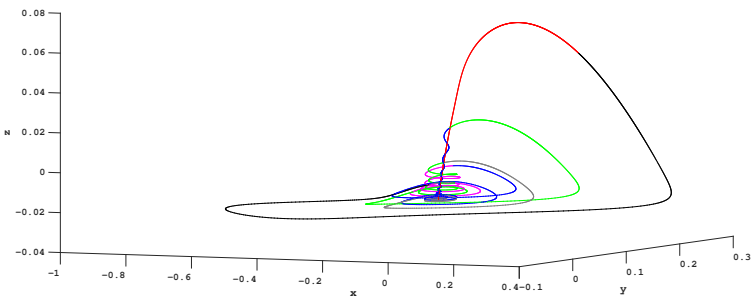

(d)

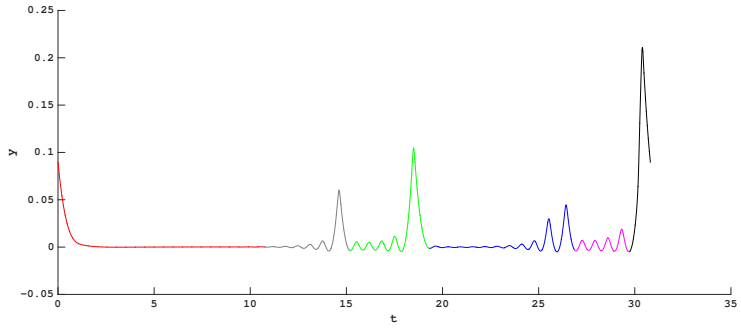

Figure 3.2: (a-b) Subinterval of the return map $R : \Sigma_+ \to \Sigma_+$ of Eqs. (3.2) ((a) is a zoom-in of the right end of (b)). Dashed black line intersects the graph of R at the fixed points of R. (c) Periodic orbit corresponding to fixed point of R at $z \approx 0.05939079$. (d) Time series of the periodic orbit. The orbit is decomposed into red, gray, green, blue, magenta, and black segments (defined in Sec. 3.4). Parameter set: $\nu \approx 0.00870134$, $a = -0.3$, $b = -1$, $c = 1$.

- first, we approximate the return map by a one-dimensional map on an interval and describe the typical dynamics of a trajectory (in the full system) corresponding to returns of this map;
- then, we demonstrate the existence of saddle-node and period-doubling bifurcations in this one-dimensional approximation and describe how these bifurcations relate to transitions of MMOs occurring in the full system; and
- finally, we describe a parameter set on which the return dynamics are well-approximated by a unimodal map having escape sets within the interval.

3.4.1 One-dimensional projection of mixed-mode oscillations

When Γ exists, the domain of the return map is now disconnected, with components separated by gaps of nonzero length (Fig. 3.2(a)). The gaps where R is undefined correspond to those trajectories beginning on S_ε^{a+} that asymptotically approach Γ without making a large-amplitude oscillation. Near the boundaries of the intervals where R is defined, the derivative changes rapidly within tiny intervals (Fig. 3.2(b)). These points arise from canard segments of trajectories resulting in a jump from S_ε^r to S_ε^{a+} and hence to Σ_+. Fixing the parameters and iteratively refining successively smaller windows of initial conditions, this pattern of disconnected regions where the derivative changes rapidly repeats several times, within the resolution of the double-precision arithmetic we use in our computations. One consequence of this structure is the existence of large numbers of unstable periodic orbits, defined by fixed points of R at which $|R'(z)| > 1$. This topological structure also appears to be robust to variations of the parameter ν.

(a)

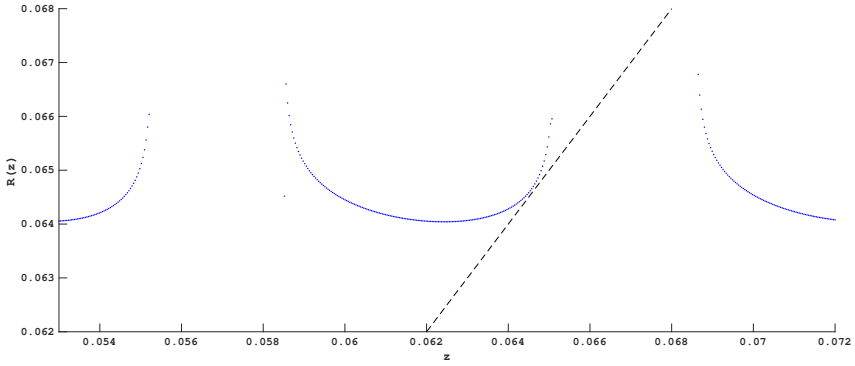

(b)

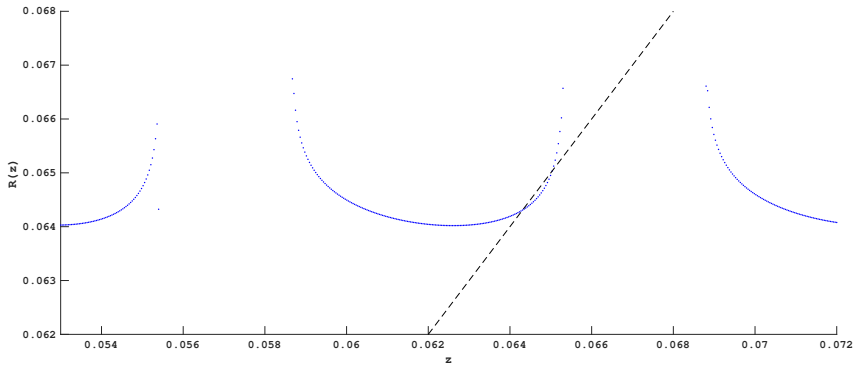

Figure 3.3: Saddle-node bifurcation of periodic orbits in system (3.2). (a) $\nu = 0.00801$, (b) $\nu = 0.00802$. Dashed black line is the line of fixed points $\{z, z\}$. Remaining parameters: $a = -0.3, b = -1, c = 1$.

This complicated structure arises from the interaction between $B(\Gamma)$, the twist region near the folded singularity and $W^{u,s}$. To illustrate this, consider an unstable fixed point $z \approx 0.05939079$ of the return map illustrated in Fig. 3.2(a). The corresponding unstable periodic orbit in the full system of equations is shown in Fig. 3.2(c)-(d). This orbit is approximately decomposed according to its interactions with the (un)stable manifolds of p_{eq} and the slow manifolds. Here is one possible forward-time decomposition of this orbit:

- A segment (red) that begins on S_ε^{a+} and flows very close to p_{eq} by remaining near W^s,

- a segment (gray) that leaves the region near p_{eq} along W^u, then jumps right from S^r to S_ε^{a+},
- a segment (green) that flows from S_ε^{a+} to S_ε^r, making small-amplitude oscillations while remaining a bounded distance away from p_{eq}, then jumping right from S_ε^r to S_ε^{a+},
- a segment (blue) that flows back down into the region near p_{eq}, making small oscillations around W^s, then jumping right from S_ε^r to S_ε^{a+},
- a segment (magenta) with similar dynamics to the green segment, making small-amplitude oscillations while remaining a bounded distance away from p_{eq}, then jumping right from S_ε^r to S_ε^{a+}, and
- a segment (black) making a large-amplitude excursion by jumping left to S_ε^{a-}, flowing to the fold $L_{-2/3}$, and then jumping to S_ε^{a+}.

A linearized flow map can be constructed[34, 80] in small neighborhoods of the saddle-focus p_{eq}, which can be used to count the number of small-amplitude oscillations contributed by orbit segments approaching the equilibrium point. However, the small-amplitude periodic orbit and the twist region produce additional twists, as observed in the green and magenta segments of the example above.

3.4.2 Bifurcations of MMOs: saddle-node and period-doubling

Fixed points of a return map defined on the section Σ_+ are interpreted in the full system as the locations of mixed-mode oscillations, formed from trajecto-

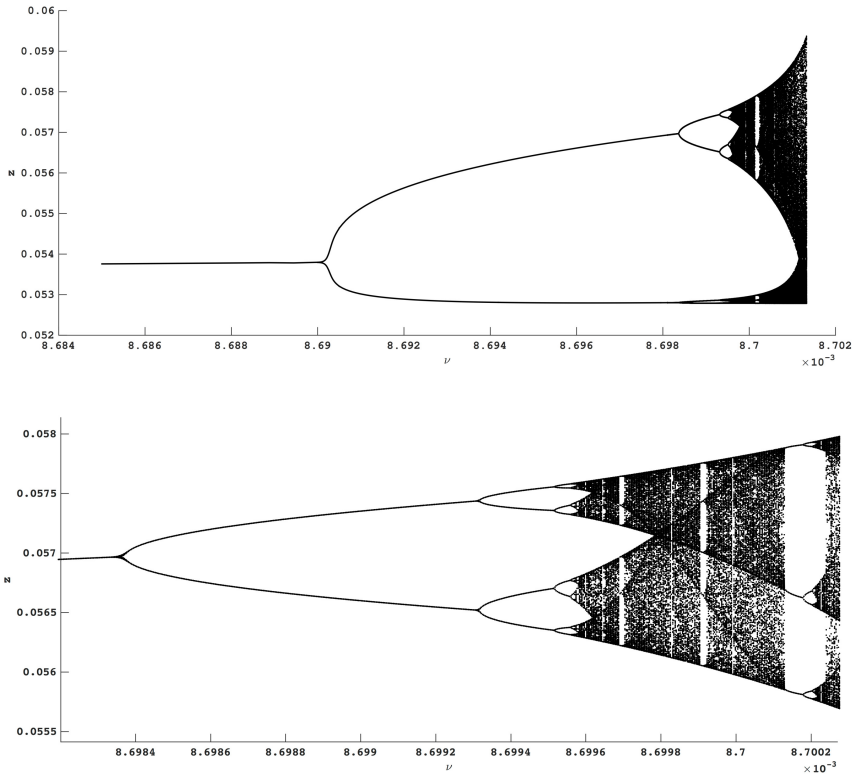

(a)

(b)

Figure 3.4: (a) Period-doubling bifurcation sequence of the one-dimensional approximation of the return map $R : \Sigma_+ \to \Sigma_+$ as the parameter ν is varied from 0.008685 to 0.0087013. Remaining parameters: $a = -0.3$, $b = -1$, $c = 1$. (b) Magnification of upper branch of first period doubling cascade.

ries making one large-amplitude passage after interacting with the local mechanisms near L_0. Similarly, periodic orbits of the (discrete) return map can be used to identify mixed-mode oscillations having more than one large-amplitude passage. We demonstrate common bifurcations associated with these invariant objects. First we locate a saddle-node bifurcation of periodic orbits, in which a pair of orbits coalesce and annihilate each other at a parameter value.

Fig. 3.3 demonstrates the existence of a fixed point $z = R(z)$ with unit derivative as ν is varied within the interval $[0.00801, 0.00802]$. Such a parameter set lies on a generically codimension one branch in the parameter space. Saddle-node

bifurcations produce a stable-unstable pair of cycles in the full system (with identical signatures to the bifurcating orbit). Either of these may in turn undergo torus bifurcations and period-doubling cascades as a parameter is varied.

The beginning of a period-doubling cascade is identified in the return map R as ν is varied in the interval $[0.008685, 0.0087013]$ (Fig. 3.4a). Within this range, period-3, period-5, and period-6 windows are readily identifiable in Fig. 3.4(b). The local unimodality of the return map suggests that our (ν-parametrized) family of return maps share some universal properties with maps of the interval that exhibit period-doubling cascades,[30, 20] despite the nonlinearity at the right boundary of the interval observed in Fig. 3.2. This structure appears to be robust to small changes in the parameter ν.

We conclude by stressing that these bifurcations generate additional *large-amplitude* oscillations of MMOs (i.e. transition is of the form $L_n^{s_n} \to (2L_n)^{s_n}$). In between period-doubling events, more small-amplitude twists may be generated, but a shortcoming of this one-dimensional analysis is that we cannot see where these intermediate bifurcations occur. The mechanism for producing small-amplitude oscillations will become clearer in Sec. 3.5, when we study return maps defined on cross-sections nearer to p_{eq} and Γ.

3.4.3 Nontrivial aperiodic MMOs

We recall a classical result of unimodal dynamics for the quadratic family $f_a(x) = 1 - ax^2$ near the critical parameter $a = 2$, where $f_a : I \to I$ is defined on its invariant interval I (when $a = 2$, $I = [-1, 1]$). On positive measure sets of parameters near $a = 2$, the map f_a admits absolutely continuous invariant mea-

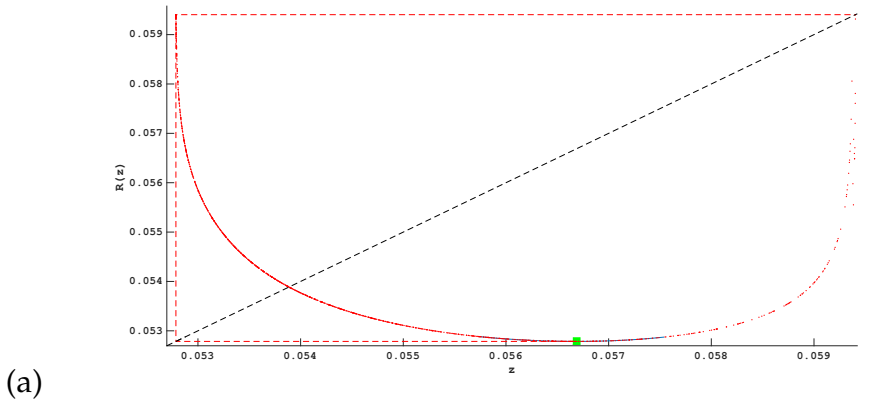

(a)

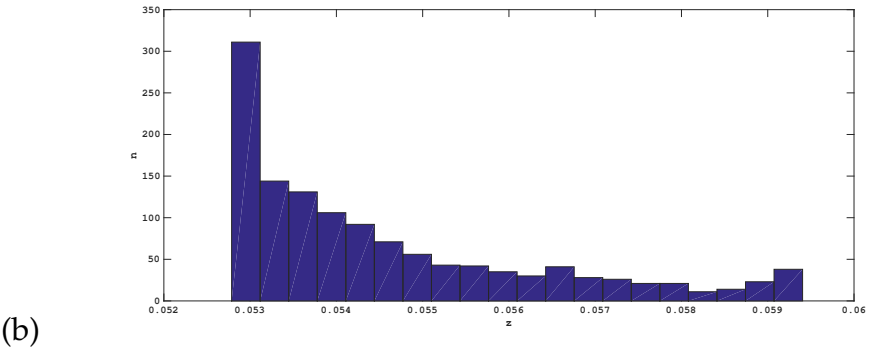

(b)

Figure 3.5: (a) Forward trajectory (red points) of the critical point (green square) under the return map $R : \Sigma_+ \to \Sigma_+$. Red dashed lines indicate the cobweb diagram of the first two iterates of the trajectory to guide the eye. Black dashed line intersects the graph of R at fixed points. All 1284 forward iterates are plotted. The subsequent iterate lands outside the domain of R: the corresponding portion of the full trajectory of (3.2) tends asymptotically to Γ without returning to Σ_+. (b) Distribution of points in the forward orbit of the critical point. Parameter set: $\nu \approx 0.00870134$, $a = -0.3$, $b = -1$, $c = 1$.

sures (a.c.i.m.) with respect to Lebesgue measure.[52] These facts depend on the delicate interplay between stretching behavior away from neighborhoods of the critical point, together with recurrence to the arbitrarily small neighborhoods of the critical point as trajectories are 'folded back' under the action of f. Since Jakobson's result in 1981, several extensions to the theory have been proven in various directions. Nowicki and van Strien [70] proved that a.c.i.m. exist for C^2 unimodal maps satisfying a generalization of the usual negative

Schwarzian derivative. In a complementary direction, Benedicks and Young [5] proved the existence and stability of a.c.i.m. for small random perturbations of the quadratic family.

These results motivate our current objective: to locate a parameter set for which (i) there exists a forward-invariant subset $\Sigma_u \subset \Sigma_+$ where $R : \Sigma_u \to \Sigma_u$ is a unimodal map (having exactly one critical point $c \in \Sigma_u$), and (ii) $R^2(c)$ is a fixed point of R at the right endpoint of Σ_u. It is difficult to locate a parameter set satisfying both (i) and (ii), but we can relax condition (i) to identify a parameter set where (i') R has the topology of Fig. 3.2 (i.e. is unimodal over a sufficiently large interval) and admits a critical point satisfying (ii). This parameter set is numerically approximated using a two-step bisection algorithm. First, a bisection method is used to approximate the critical point c by refining the region where R' first changes sign up to a fixed error tolerance 10^{-15}. Another bisection method is used to approximate the parameter value at which $|R^2(c) - R^3(c)|$ is minimized. This distance can be minimized to 2.5603×10^{-8} at the parameter set $(\nu, a, b, c) = (0.0087013381084, -0.3, -1, 1)$.

Fig. 3.5(a) depicts the forward trajectory of the critical point near the line of fixed points at this parameter value. Note that we have made no effort yet to numerically check theoretical conditions for an a.c.i.m.– nevertheless, we can identify complicated transient dynamics consistent with the existence a conditionally invariant measure for an expanding map. [74] The itinerary of c is finite, eventually landing in a subinterval of Σ_u where R is undefined. Even so, its forward orbit is unpredictable, sampling the interval $\left[R(c), R^2(c)\right]$ with a nontrivial transient density for 1284 iterates (Fig.3.5(b)). The length of the itinerary is extremely sensitive to tiny ($O(10^{-14})$) perturbations of the parameter b, reflecting

the sensitive dependence of initial conditions in the selected parameter neighborhood. However, the distributions of the forward iterates appear to be more robust to small parameter changes: they are all similar to the distribution shown in Fig. 3.5(b).

3.5 Two-dimensional return maps

Fix a compact subset $\Sigma_0 \subset \{z = 0\}$ containing the first intersection (with orientation $\dot{z} > 0$) of W^s and such that $\Gamma \cap \Sigma_0 = \emptyset$. Recall that the forward return map $R : \Sigma_0 \to \Sigma_0$ is undefined on the immediate basin of attraction B_0, and points landing in B_0 under finitely many forward iterates of R 'escape.' We have the set inclusion $\phi^{t\geq 0}(\cup_{i=0}^{\infty} R^{-i}(B_0)) \subset B(\Gamma)$, and the j-th iterate of the return map R^j is defined only on the subset $\Sigma_0 - \cup_{i=0}^{j} R^{-j}(B_0)$. We abuse notation slightly and denote by S_ε^{a+} (resp. S_ε^r) the intersections of these slow manifolds with Σ_0. We also refer to the intersection of S_ε^{a+} (resp. S_ε^r) with Σ_0 as the *attracting* (resp. *repelling*) *spiral* due to its distinctive shape (see Figure 3.6). The basin B_0 is sampled by the gray points in Fig. 3.6(a), accounting for the finite-length gaps in the one-dimensional return maps.

The slow manifolds intersect transversely. Segments of the attracting spiral can straddle both B_0 and the repelling spiral. In Fig. 3.6(b), we color initial conditions based on the maximum y-coordinate achieved by the corresponding trajectory before its return to Σ_0. Exchange Lemma-type calculations imply that only thin bands of trajectories are able to remain close enough to S_ε^r to jump at an intermediate height. We choose the maximum value of the y-coordinate to approximately parametrize the length of the canards. This parametrization

(a)

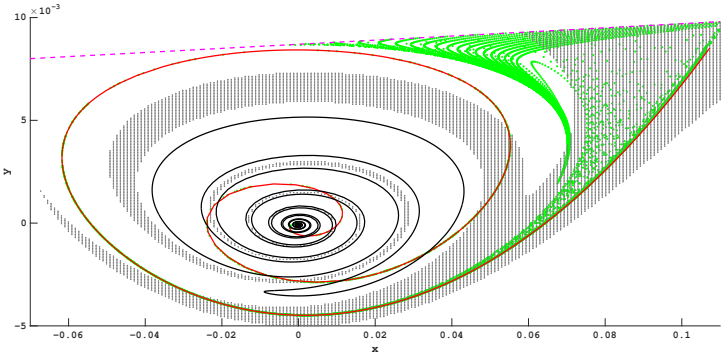

(b)

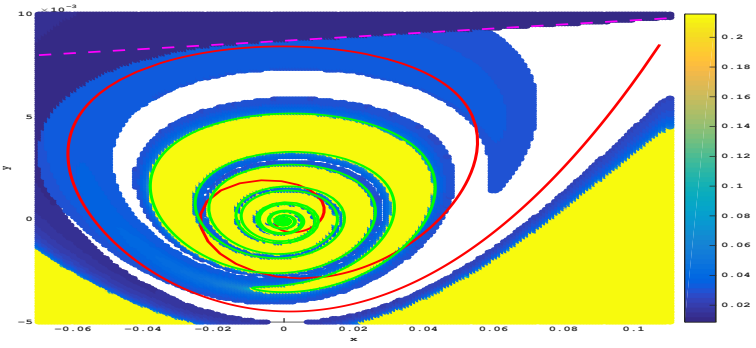

Figure 3.6: (a) Geometry in the section $\Sigma_0 = \{(x, y, z) : x \in [-0.07, 0.11], y \in [-0.005, 0.01], z = 0\}$. Gray points sample the subset of Σ_0 whose corresponding forward trajectories tend to the stable periodic orbit without returning to Σ_0. Green points denote the first forward return of the remaining points in Σ_0 with the orientation $\dot{z} < 0$. (b) Color plot of maximal height (y-coordinate) obtained by trajectories that return to Σ_0 as defined in previous subfigure. Cross-sections of S_ε^{a+} (red) and S_ε^r (green) at Σ_0 are shown, and the tangency of the vector field with Σ_0 (i.e. the set $\{ax + by = -\nu\}$) is given by the magenta dashed line. Parameter set: $\nu \approx 0.00870134$, $a = 0.01$, $b = -1$, $c = 1$.

heavily favors trajectories jumping left (from S_ε^r to S_ε^{a-}) rather than right (from S_ε^r to S_ε^{a+}), since trajectories jumping left can only return to Σ_0 by first following S_ε^{a-} to a maximal height, and then jumping from $L_{-2/3}$ to S_ε^{a+}. In Figure 3.6, S_ε^r separates the blue and yellow regions, allowing us to distinguish trajectories turning right to S_ε^{a+}or left to S_ε^{a-} before returning to Σ_0. This distinction will become useful in constructing our dynamical partition later. Summarizing,

(a)

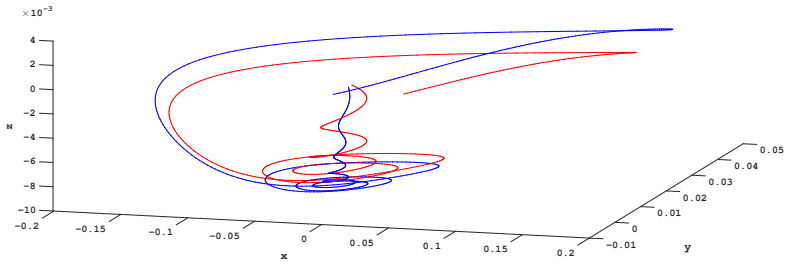

(b)

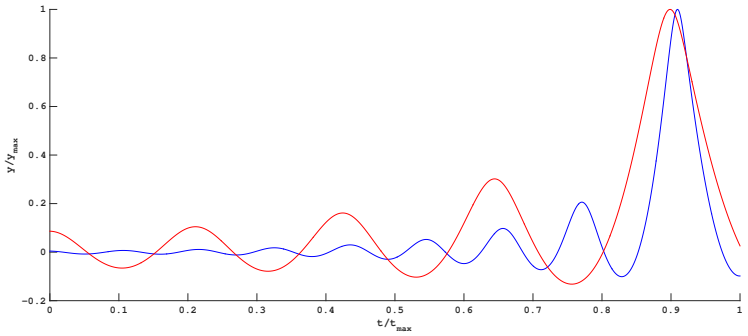

Figure 3.7: (a) Two phase space trajectories beginning and ending on the section $\{z = 0\}$ with stopping condition $\dot{z} < 0$ and (b) the time series of the y-coordinates of each trajectory. To better compare qualitative differences between these orbit segments, stopping times and amplitudes are both rescaled to one. Initial conditions: blue, $(x, y, z) = (0.000553, 0.000201, 0)$; red, $(x, y, z) = (0.000553, 0.003065, 0)$. Parameter set: $\nu \approx 0.00870134$, $a = 0.01$, $b = -1$, $c = 1$.

∂B_0 and S^r_ε partition this section according to the behavior of orbits containing canards.

Trajectories beginning in Σ_0 either follow W^s closely and spiral out along W^u or remain a bounded distance away from both the equilibrium point and W^s, instead making small-amplitude oscillations consistent with a folded node.

The transition from one type of small-amplitude oscillation to the other depends continuously on the initial condition from W^s, which we now demonstrate with an example. Two initial conditions are chosen on a vertical line em-

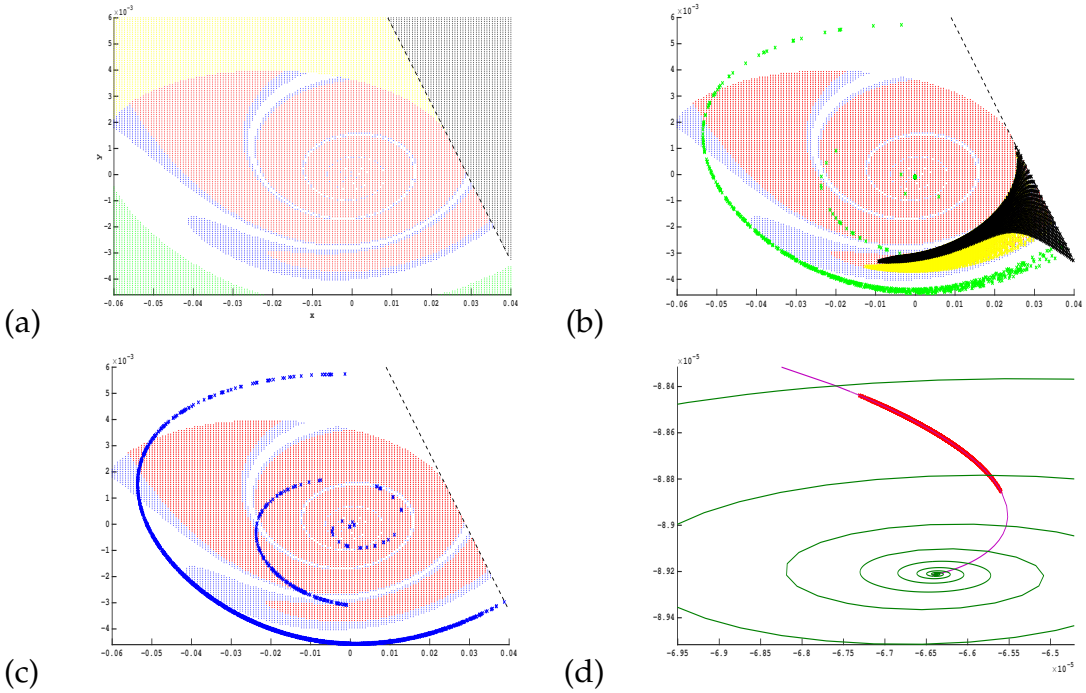

Figure 3.8: (a) Partition of a compact subset of the cross-section Σ_0. Black dashed line is the tangency of the vector field $\{\dot{z} = 0\}$, separating the subsets $\{\dot{z} > 0\}$ (black points) and $\{\dot{z} < 0\}$. Yellow (resp. green): points above (resp. below) the line $\{y = 0\}$ with winding number less than three. Red (resp. blue): points whose forward trajectories reach a maximal height greater than (resp. less than) 0.18 and have winding number three or greater. (b) Overlay of red and blue subsets of domain (points) with images of yellow, green, and black subsets (crosses). (c) Overlay of red and blue subsets of domain (points) with the image of the blue subset (crosses). (d) Overlay of attracting spiral (magenta), repelling spiral (dark green), and image of red subset (crosses). Note the change in scale of the final figure. Generated from a 500×500 grid of initial conditions beginning on Σ_0. Parameter set: $\nu \approx 0.00870134$, $a = -0.3$, $b = -1$, $c = 1$.

bedded in the section $\{z = 0\}$, having the property that the resulting trajectory jumps right from S^r_ε at an intermediate height before returning to the section with orientation $\dot{z} < 0$. These initial conditions are found by selecting points in Fig. 3.6(b) in the blue regions lying on a ray that extends outward from the center of the repelling spiral. The corresponding return trajectories are plotted in Fig. 3.7. The production of small-amplitude oscillations is dominated by the saddle-focus mechanism: in the example shown, the red orbit exhibits four oscillations before the (relatively) large-amplitude return, whereas the blue orbit exhibits seven oscillations. We can select trajectories with increasing numbers of small-amplitude oscillations by picking points closer to $W^s \cap \{z = 0\}$.

A complication in this analysis which we have ignored until now is that jumps at intermediate heights, which are clearly shown to occur in these examples, blur the distinction between 'large' and 'small' oscillations in a mixed-mode cycle. We will construct one such 'medium' amplitude MMO concretely in the next section. This makes a classification of trajectories based on signature less useful. Our forthcoming partition will instead classify orbits based on the number of turns and on a 'jump direction,' which will remove this ambiguity.

3.5.1 Dynamical partitions

We now study some of the possible concatenations of small-amplitude oscillation segments as seen in Fig. 3.7. The basis for determining allowed concatenations is to partition the cross-section Σ_0 and then to study the images of these partition subsets under the forward return map. We gradually define this partition in stages:

- First, tangencies of the vector field with Σ_0 allow us to restrict to an invariant subset of the cross-section
- Then, we identify mixed-rank behavior in this subset which is intimately connected to the intersections of S_ε^{a+} with S_ε^r. This allows us to generate a coarse partition.
- Finally, we define the winding number of a trajectory, which allows us to further refine this partition. Subsets in this refined partition therefore depend on both the turning of the trajectory with initial condition in Σ_0 as well as the location of this initial condition relative to S_ε^r.

Tangencies of the vector field with the cross-section are given by curves which partition the section into disconnected subsets. The subset that does not contain the attracting and repelling spirals is mapped with full rank to the remaining subset by the return map (Fig. 3.8(b)), allowing us to restrict our analysis to an invariant two-dimensional subset where the vector field is transverse everywhere. Mixed-rank behavior occurs in this subset, as shown in Fig. 3.8.

Note that the figures 3.8-3.12 are plotted at a slightly different parameter set from the earlier figures 3.6 and 3.7, whose parameter set was chosen to give a clearer picture of the main components of the return map. The main difference is that the line of vector field tangencies intersects a portion of the attracting spiral, but this does not affect the following arguments. Trajectories jumping left to S_ε^{a-} reach a greater maximal height (y-component) than the trajectories jumping right to S_ε^{a+}. The region is partitioned according to three criteria: their location with respect to the curve of tangency, and their location with respect to the repelling spiral (corresponding to left or right jumps), and their winding number, defined later in this section. See Fig. 3.8.

We can now state two significant results:

- *Mixed-rank dynamics*. As shown in Fig. 3.8(c)-(d), the red and blue regions collapse to S_ε^{a+} within one return. This includes those trajectories that return to the cross-section by first jumping right from S_ε^r to S_ε^{a+} at an intermediate height. Fig. 3.8(b) shows that the yellow subset returns immediately to this low-rank region. The green subset returns either to the low-rank region or to the yellow region. But note that it does not intersect its image, and furthermore, it intersects the yellow region on a portion of the attracting spiral. Therefore, after at most two returns the dynamics of the points beginning in Σ_0 (and which did not map to B_0) is characterized by the dynamics on the attracting spiral.
- *Trajectories jumping left or right return differently*. Those trajectories jumping left to S_ε^{a-} return to a tiny segment very close to the center of the S_ε^{a+}, as shown in Fig. 3.8(d). In contrast, the trajectories jumping right sample the entire spiral of S_ε^{a+}, as shown in Fig. 3.8(c). Thus, multiple intermediate-height jumps to the right are a necessary ingredient in concatenating small- and medium-amplitude oscillations (arising from right jumps) between large-amplitude excursions (arising from left jumps).

We now construct a dynamical partition of the cross-section. Let s and u denote a stable and unstable eigenvector, respectively, of the linearization of the flow at p_{eq}. Then consider a cylindrical coordinate system with basis (u, s, n) centered at p_{eq}, where $n = u \times s$. The *winding* of a given trajectory is the cumulative angular rotation (divided by 2π) of the projection of the trajectory onto the (u, n)-plane. The *winding number* (or simply *number of turns*) of a trajectory is the integer part of the winding.

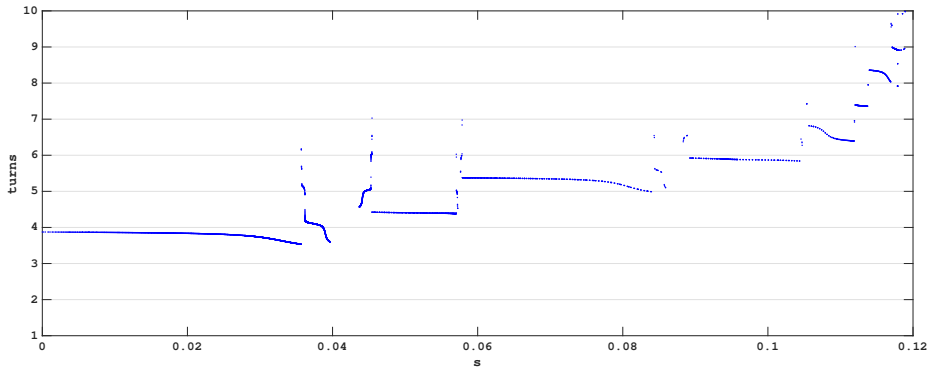

Figure 3.9: Winding of the attracting spiral as a function of its parametrization by arclength. The starting point $s = 0$ is chosen close to the tangency. Positive values of s track the spiral as it turns inward. Parameter set: $\nu \approx 0.00870134$, $a = -0.3$, $b = -1$, $c = 1$.

The cumulative angular rotation depends on both the initial and stopping condition of the trajectory, which in turn depend on the section used. Close to p_{eq}, the winding of a trajectory measures winding around W^s. Most of the rotation occurs as trajectories enter small neighborhoods of p_{eq} by winding around W^s; our choice of coordinates ensures that we can measure this winding in a well-defined manner.

If Fig. 3.9, we study the winding on a connected subset of the attracting spiral. On this connected subset we may parametrize the spiral by its arclength. The number of turns increases by approximately one whenever S_ε^{a+} intersects S_ε^r twice (these intersections occur in pairs since they correspond to bands of trajectories on S_ε^{a+} which leave the region by jumping left to S_ε^{a-}). In between these intersections, there are gaps corresponding to regions where S_ε^{a+} intersects B_0.

As shown in Fig. 3.10, sets in the partition are defined according to each tra-

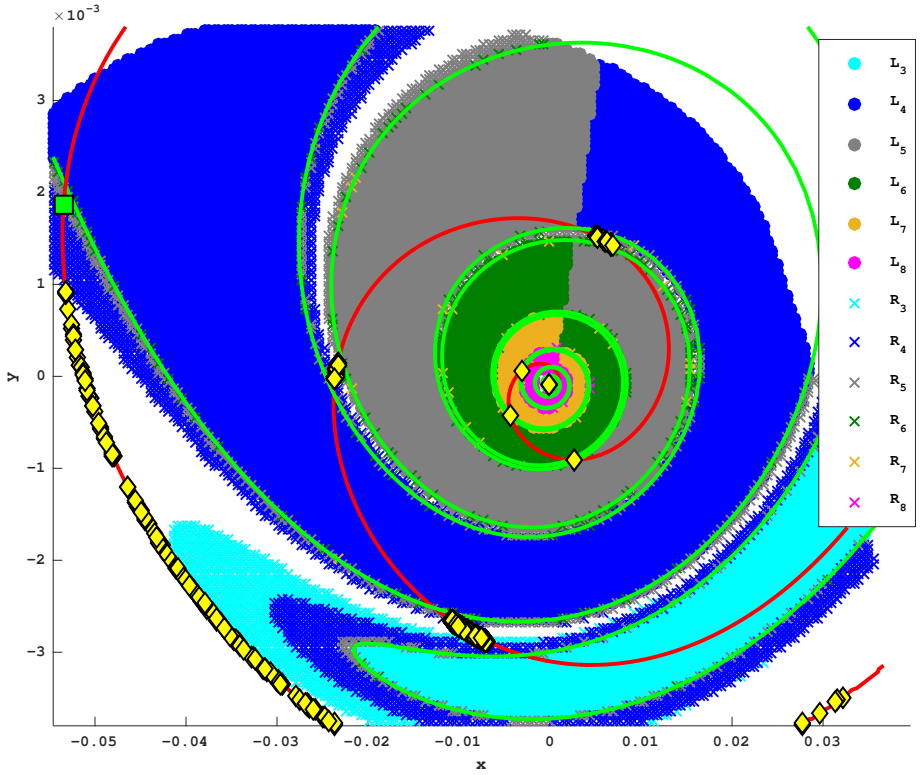

Figure 3.10: Partition of the section $\Sigma_0 = \{z = 0\}$ according to number of turns made by corresponding trajectories as well as whether the trajectories turn left or right from S^r_ε. Left-turning trajectories are plotted with dots and right-turning trajectories are plotted with crosses. Color definitions: teal, 3 turns; blue, 4 turns; gray, 5 turns; green, 6 turns; gold, 7 turns; magenta, 8 turns. The slow manifolds S^{a+}_ε (red curve) and S^r_ε (green curve) and the saddle-point defined in Figure 3.11 (green square) are also shown. Yellow diamonds: final intersections of trajectories starting from a 20×20 grid of initial conditions beginning on Σ_0, which exhibit between 4 and 35 returns before tending asymptotically to Γ. Parameter set: $\nu \approx 0.00870134$, $a = -0.3$, $b = -1$, $c = 1$.

jectory's winding number and jump direction. This partition uses the attracting and repelling spirals as a guide; small rectangles straddling the attracting spiral are contracted strongly transverse to the spiral and stretched along the attracting spiral, giving the dynamics a hyperbolic structure. In the next section we will compute a transverse homoclinic orbit, where this extreme contraction and expansion is shown explicitly.

3.5.2 Symbolic maps

We restrict ourselves to a subset $S \subset \Sigma_0$ where returns are close to rank one (i.e. the union of red and blue regions in Fig. 3.8(a)). Let $L_n \subset S$ (resp. $R_n \subset S$) denote points whose forward trajectories make n turns before jumping left to S_ε^{a-} (resp. right to S_ε^{a+}). Then define $L_{tot} = \cup_{n=0}^{\infty} L_n$ and $R_{tot} = \cup_{n=0}^{\infty} R_n$. The collection $\mathcal{P} = \{L_i, R_j\}_{i,j=1}^{\infty}$ partitions S. We clarify the following ambiguity: the newly-defined symbols L_i are unrelated to the large-amplitude oscillation notation in the definition of an MMO signature (eg. $L_i^{s_i}$).

For a collection of sets $\mathcal{A}$, let $\sigma(\mathcal{A})$ denote the set of all finite or infinite one-sided symbolic sequences $x = x_0 x_1 x_2 \cdots$ with $x_i \in \mathcal{A}$. We can assign to each $x \in S$ a symbolic sequence in $\sigma(\mathcal{P} \cup \{S^c, B_0\})$, also labeled x. This sequence is constructed using the return map: $x = \{x_i\}$ is defined by $x_i = \iota(R^i(x))$, where $\iota : \Sigma_0 \to \mathcal{P} \cup \{B_0, S^c\}$ is the natural inclusion map. We allow finite sequences since R is undefined over B_0. A portion of the partition is depicted in Fig. 3.10.

The results in Figs. 3.8 and 3.10 and the definition of B_0 constrain the allowed symbolic sequences:

- *Blocks containing S^c.* $R(S^c) \subset S$ (Fig. 3.8(b)).
- *Allowable symbols following R_i.* The following intersections with $R(R_{tot})$ are nonempty:

  $R(R_{tot}) \cap S_\varepsilon^{a+} \cap L_i \neq \emptyset$ and

  $R(R_{tot}) \cap S_\varepsilon^{a+} \cap R_j \neq \emptyset$

  whenever $L_i, R_j \neq \emptyset$ (Figs. 3.8(c) and 3.10).
- *Allowable symbols following L_i.* There exists a sufficiently large integer N with

  $R(L_{tot}) \subset S_\varepsilon^{a+} \cap (\cup_{n \geq N} L_n \cup R_n \cup B_0)$ (Figs. 3.8(d) and 3.10).
- *Finite symbol sequences.* The set of finite sequences are precisely those containing and ending in B_0 (yellow points in Fig. 3.10).

The subset S^c intersects the image of R_{tot} nontrivially. The first result implies the symbolic sequence of a point $x \in S$ whose forward returns leave the subset S must contain the block

$$x_{n_j-1} S^c x_{n_j},$$

where the index n_j is defined by the j-th instance when the orbit leaves S and $x_{n_j-1} \in \mathcal{P}$. Our numerical results allow us to further constrain the allowed symbols of x_{n_j}. For the parameter set we used, the subset $R(S^c \cap S_\varepsilon^{a+})$ nontrivially intersects subsets of $\mathcal{P} \cup \{B_0\}$ only in the subcollection $\mathcal{P}_c = \{L_3, L_4, L_5, R_3, R_4, R_5, B_0\}$. The portion of the attracting spiral which lies outside S is a subset of the region of Σ_0 where R has full rank. Therefore, the image of this portion of the attracting spiral is well-approximated by a curve segment lying inside the region sampled by the yellow and black points shown in Fig. 3.8(b). Therefore $x_{n_j} \in \mathcal{P}_c$ whenever n_j is defined.

The second result implies that for any integer $n \geq 1$, the block $L_n\alpha_m$ (where $\alpha \in \{L, R\}$) is impossible when $m < N$, since $R(L_n)$ is either B_0 or $\alpha_{m \geq N}$. For the parameter set used in Fig. 3.10, our calculations suggest $N \geq 13$. The third result reminds us that only right-jumping trajectories are able to sample the entire attracting spiral.

The second and third results then imply that blocks of type R_iL_j or R_iR_j are necessarily present in the symbolic sequences of orbits which concatenate small-amplitude oscillations with medium-amplitude oscillations as shown in Fig. 3.7, since medium-amplitude oscillations arise precisely from those points on Σ_0 whose forward trajectories remain bounded away from the saddle-focus (i.e. those points in Σ_0 sufficiently far from the intersection of W^s with Σ_0) and jump right. These results also imply that forward-invariant subsets lie inside the intersection of S_ε^{a+} with Σ_0. In terms of the full system, it follows that the trajectories corresponding to these points each contain segments which lie within a sheet of S_ε^{a+}.

In view of the last result, for each $i \geq 1$ define the i-th *escape subset* E_i to be the set of length-i sequences ending in B_0. Note that E_i contains the symbol sequences of the points in $R^{-(i-1)}(B_0)$. Escape rates of typical initial conditions in Σ_0 are studied in detail in the following section. The next section provides a concrete numerical example of a point in E_n, where n is at least 1284.

Let us summarize the main results of the symbolic dynamics. Points beginning on Σ_0 are identified with one of the following three types of one-sided symbolic sequences:

- Sequences ending in B_0 (tending asymptotically close to Γ)

(a)

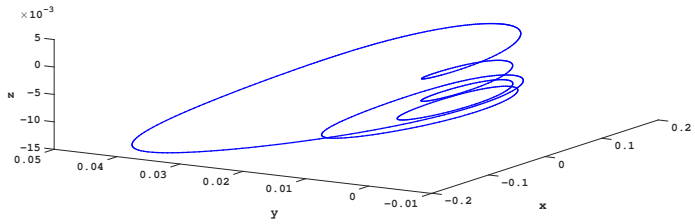

(b)

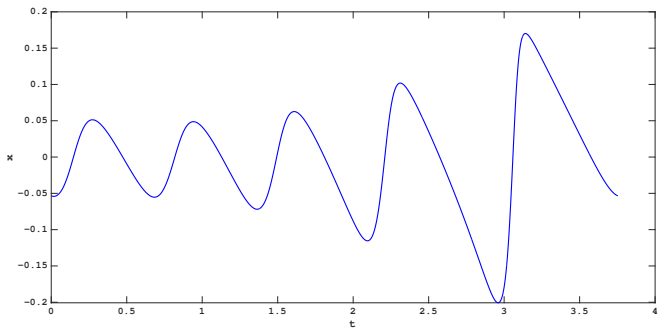

Figure 3.11: (a) Mixed-mode oscillation in phase space corresponding to the saddle point $p \approx (-0.053438, 0.001873)$ of the return map defined on $\Sigma_0 = \{z = 0\}$ and (b) the time series of its x-component. Parameter set: $\nu \approx 0.00870134$, $a = -0.3$, $b = -1$, $c = 1$.

- Sequences with an infinitely repeating finite block (periodic MMOs)
- Infinitely long, nonrepeating sequences (nontrivial, aperiodic MMOs).

3.5.3 Case study: Symbolic dynamics near a saddle-point and medium-amplitude oscillations

The structure of the invariant sets and escape sets of the two-dimensional return map is related to the intersection of the basin of attraction of the small-amplitude stable periodic orbit with Σ_0. We begin by studying two types of invariant sets: fixed points and transverse homoclinic orbits.

Certain invariant sets of the map may be used to construct open sets of points all sharing the same initial block in their symbolic sequence. We briefly describe how the simplest kind of invariant set—a fixed point—implies that neighborhoods of points must have identical initial sequences of oscillations. In Fig. 3.11 we plot the saddle-type MMO corresponding to a saddle equilibrium point p, whose location in the section $\{z = 0\}$ is plotted in Figs. 3.10 and 3.12. According to Fig. 3.10, p has symbolic sequence $R_5R_5R_5\cdots$, in agreement with the time-series shown in Fig. 3.11(b). Observe that the fixed-point is sufficiently far away from W^s (the stable manifold of the saddle-focus) that the oscillations of the corresponding periodic orbit do not clearly arise from small winding near p_{eq}. Furthermore, the dynamics in small neighborhoods of p are described by the linearization of the map R near p. This implies that small neighborhoods of p consist of points with initial symbolic blocks of R_5, where the length of this initial block can be as large as desired. We can relax the condition that this be the initial block by instead considering preimages of these neighborhoods.

From this case study we observe that arbitrarily long chains of oscillations of varying sizes can be constructed using immediate neighborhoods of fixed points, periodic points, and other invariant sets lying in $S_\varepsilon^{a+} \cap \{z = 0\}$. These in turn correspond to complicated invariant sets in the full three-dimensional system. Consequently, the maximum number of oscillations produced by a periodic orbit having one large-amplitude return can be very large at a given parameter value, depending on the number of maximum possible returns to sections in the region containing these local mechanisms. This situation should be compared to earlier studies of folded-nodes, in which trajectories with a given number of small-amplitude oscillations can be classified;[90] and the Shilnikov bifurcation in slow-fast systems, in which trajectories have unbounded numbers

of small-amplitude oscillations as they approach the homoclinic orbit.[42]

3.5.4 Structure of invariant and escape sets

The return map R strongly contracts two-dimensional subsets of the cross-section to approximately one-dimensional subsets of S_ε^{a+}. Subsequent returns act on S_ε^{a+} by stretching and folding multiple times, before finally contracting strongly onto S_ε^{a+} again. Chaotic invariant sets and horseshoes of the two-dimensional return map must clearly be very degenerate. We now explore the structure of these invariant sets.

Let U be a small neighborhood of the saddle fixed point p that we located in the previous section. In Fig. 3.12 we plot U, $R(U)$, $U \cap R^{-1}(U)$, and $W^s(p)$ on the section Σ_0. The image $R(U)$ is a nearly one-dimensional subset of S_ε^{a+} and the preimage is a thin strip which appears to be foliated by curves tangent to S_ε^r. The subsets $R(U)$ and $R^{-1}(U)$ contain portions of $W^u(p)$ and $W^s(p)$, respectively. The transversal intersection of $R(U)$ with $W^s(p)$ is also indicated in this figure.

Accurately computing R^{-1} is challenging. Trajectories which begin on the section and approach the attracting slow manifolds $S_\varepsilon^{a\pm}$ in reverse time are strongly separated, analogous to the scenario where pairs of trajectories in forward time are strongly separated by S_ε^r. This extreme numerical instability means that trajectories starting on the section and integrated backward in time typically become unbounded. In order to compute $W^s(p)$, we instead compute orbits in forward time and recast this as a boundary value problem, with initial conditions beginning in a line on the section and ending 'at' p. Beginning with a point y_0 along $W^s(p)$, we construct a sequence $\{y_0, y_1, \cdots\}$ along $W^s(p)$ as follows.

(C1) *Prediction step*. Let $w_i = y_{i-1} + hv_i$, where h is a fixed step-size and v_i is a numerically approximated tangent vector to $W^s(p)$ at y_{i-1}.

(C2) *Correction step*. Construct a line segment L_i of initial conditions perpendicular to v_i. Use a bisection method to locate a point $y_i \in L_i$ such that $|R(y_i) - p| < \varepsilon$, where ε is a prespecified tolerance.

The relevant branch of $W^s(p)$ which intersects $R(U)$ lies inside the nearly singular region of the return map, so the segment L_i can be chosen small enough that $R(L_i)$ is approximately a segment of S_ε^{a+} which straddles p. This justifies our correction step above.

It is usually not sufficient to assert the existence of a transverse homoclinic orbit from the intersection of the image sets. But in the present case, these structures are organized by the slow manifolds S_ε^{a+} and S_ε^r. The strong contraction onto S_ε^{a+} in forward time implies that the discrete orbits comprising $W^u(p)$ must also lie along this slow manifold. The unstable manifold $W^u(p)$ lies inside a member of the $O(\exp(-c/\varepsilon))$-close family which comprises S_ε^{a+}, so the forward images serve as good proxies for subsets of $W^u(p)$ itself. On the other hand, when U is sufficiently small, its preimage $R^{-1}(U)$ appears to be foliated by a family of curves tangent to S_ε^r, such that one of the curves contains $W^s(p)$ itself.

The Smale-Birkhoff homoclinic theorem[11, 81] then implies that there exists a hyperbolic invariant subset on which the dynamics is conjugate to a subshift of finite type. Fixed points lie in S_ε^{a+} due to strong contraction, but they need not lie in S_ε^r. We end this result by commenting on the apparent degeneracy of the two-dimensional sets $U, R(U)$, and $R^{-1}(U)$. A classical proof of the Smale-Birkhoff theorem uses a set $V = R^k(U) \cap R^{-m}(U)$ (with $k, m > 0$ chosen such that

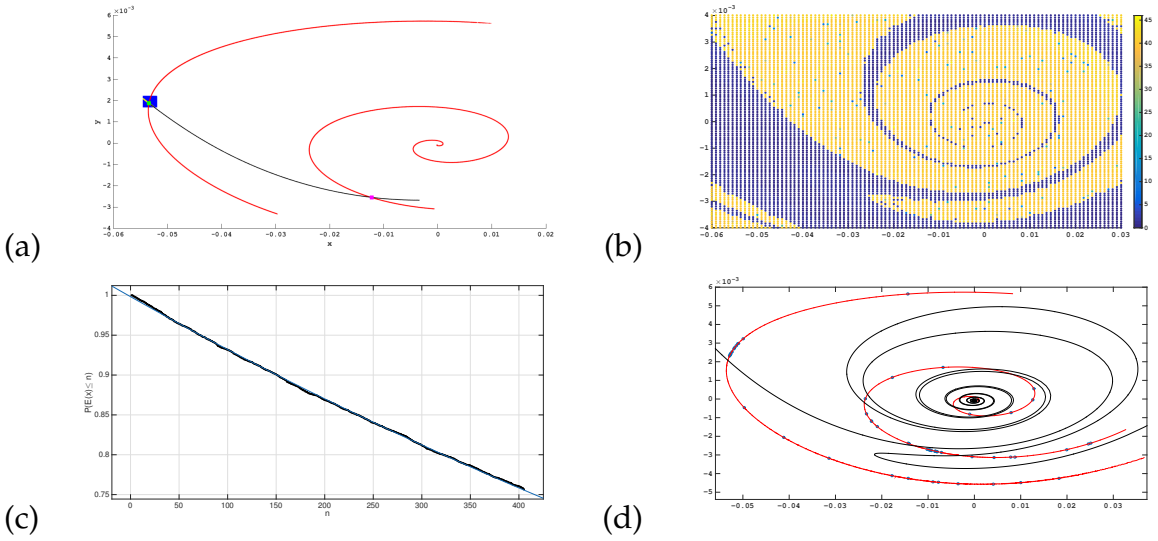

Figure 3.12: (a) A saddle equilibrium (green point) of the return map defined on $\Sigma_0 = \{z = 0\}$, together with a neighborhood U (blue grid), image $R(U)$ (red), subset of preimage $U \cap R^{-1}(U)$ (yellow), and a branch of its stable manifold $W^s(p)$(black). The intersection of $R(U)$ with $W^s(p)$ is also shown (magenta point). (b) Color plot of 10^4 initial conditions beginning in Σ_0 on a 100×100 grid, whose forward trajectories are integrated for the time interval $t \in [0, 600]$. Color denotes number of intersections with Σ_0 with orientation $\dot{z} < 0$. (c) Black points: $P(E(x) \leq n)$ vs. n for 10^4 points sampling a line segment on Σ_+. Blue curve: least squares exponential fit $y = Ae^{bn}$ of black points, with $A \approx 0.9984$ and $b \approx -6.87 \times 10^{-4}$. (d) Last recorded intersection (blue circles) of each trajectory defined in (b) with Σ_0. The attracting and repelling spirals (red and black curves, respectively) are overlaid. Parameter set: $\nu \approx 0.00870134$, $a = -0.3$, $b = -1$, $c = 1$.

V is nonempty) as the basis for constructing the Markov partition on which the shift is defined.[39] Here, V is well-approximated by a curve segment.

A natural question is whether this hyperbolic invariant set is indeed a chaotic attractor. It is difficult to conclusively decide set-invariance with finite-time computations. This difficulty is made clear in Fig. 3.12(b), where we study the eventual fate of a grid of initial conditions beginning on Σ_0. This figure

shows that even after a long integration time of $t = 600$, most initial conditions in B_0^c are able to return repeatedly to Σ_0. However, it may simply be that the measure of $(R^{-n}(B_0))^c$ decays extremely slowly to 0 as n tends to infinity.

Nonetheless, we can recover some comparisons to well-studied maps which have escape subsets and hyperbolic behavior. Known results on escape rates of expansive maps suggest that the probability that a typical point does not escape after n returns decreases as c^{-n} for some positive constant c.[74] Returning briefly to the section Σ_+, define the function $E : \Sigma_+ \to \{0, 1, 2, \cdots\} \cup \{\infty\}$ by $E(x) = n$ if n is the maximum integer for which $R^n(x)$ is defined (i.e. $R^n(x) \in B_0$) and $E(x) = \infty$ if $R^n(x)$ is defined for all n.

In Fig. 3.12(c) we compute $P(E(x) \leq n)$ vs. n for 10^4 points x sampling a line segment in Σ_+, for a very large integration time $t = 2 \times 10^4$. The function $P(E(x) \leq n)$ computes the proportion of those points in the line segment having $E(x) \leq n$. As the sample size grows large, $P(E(x) \leq n)$ converges to the probability that a typical point x (with respect to Lebesgue measure) lies in $R^{-n}(B_0)$. The resulting points admit a fit by an exponential function of the form Ae^{bx} with $b < 0$, suggesting that all points eventually escape with exponential decay. We remind the reader that the one-dimensional approximation $R : \Sigma_+ \to \Sigma_+$ is given in Fig. 3.2.

Finally, in Fig. 3.12(d), we plot the last recorded intersection with Σ_0 of those trajectories that do not tend to Γ within $t = 600$. Even with a relatively sparse grid of 10^4 initial points, these returns sample much of the attracting spiral. Many of the points are not visible at the scale of the figure because they sample the segment shown in Fig. 3.8(d): the penultimate intersections resulted in the trajectory jumping left to S_ε^{a-}. If a chaotic invariant measure exists, we expect

that its support on Σ_0 will be well-approximated by the points given in this figure. In terms of our dynamical partition, the consequence is that we observe arbitrarily long, nonrepeating symbolic sequences consisting of trajectory segments with unpredictable numbers of twists as well as types of twists (due to n, p_{eq}, and Γ).

3.6 Concluding remarks

We have highlighted just a few of the broad range of complex dynamics arising from a tangency of a slow manifold with an unstable manifold of an equilibrium point. This organization is made possible using global bifurcation theory and clever choices of return maps, defined on cross-sections where there is strong contraction near slow manifolds of the system.

We contributed a topological algorithm which classifies trajectories depending on both the number of turns they make, and on the direction of the 'jump' toward one of the attracting slow manifolds. This partition gives us some new insight into the way very different turning mechanisms—in this case, a saddle-focus equilibrium point and a folded singularity—interact in a slow-fast system. We use this partition to describe varying types of MMOs with oscillations arising from either of these turning mechanisms, or a combination of both. This demystifies how oscillations of varying types, such as those seen in Fig. 3.2(c)-(d), may be concatenated in a constructive way to produce MMOs. However, a shortcoming of this analysis is that the partition must be redrawn and reanalyzed for any new parameter set. It is desirable to find a rigorous model which

extends trajectories from flow maps defined near cylindrical cross-sections[34] near a saddle-focus equilibrium point, to regions near a folded singularity (one such analysis is provided by Krupa and Wechselberger[62]). Such an extension remains elusive and is the topic of future work.

We also motivate the study of maps having the topology shown in Fig. 3.2(a)-(b). These maps are distinguished by two significant features: they admit small disjoint escape subsets, and they may be approximated by unimodal maps over a large proportion of their domains. Sections 3.4.2 and 3.4.3 can then be regarded retrospectively as an introduction to the dynamics of these maps, framed in comparison to the relatively well-studied dynamics of unimodal and expansive maps. In particular, such maps undergo period-doubling cascades (Fig. 3.4) as a system parameter is varied. The forward trajectory of the critical point is also seen to have a transient density for a range of parameters (Fig. 3.5).

These results lead us to conjecture that statistical properties and universal cascades found in some subfamilies of unimodal maps, such as the quadratic family, persist for the family of maps studied in this paper. The geometric theory of rank-one maps pioneered by Wang and Young[88] is a possible starting point to prove theorems in this direction. This theory has been used successfully to identify chaotic attractors in families of slow-fast vector fields with one fast and two slow variables.[51] Their technique is based upon approximating returns by one-dimensional maps.

This work was supported by the National Science Foundation (Grant No. 1006272). The author thanks John Guckenheimer for useful discussions.

CHAPTER 4

PHASE DIAGRAM FOR THE KURAMOTO MODEL WITH VAN HEMMEN INTERACTIONS

4.1 Abstract

We consider a Kuramoto model of coupled oscillators that includes quenched random interactions of the type used by van Hemmen in his model of spin glasses. The phase diagram is obtained analytically for the case of zero noise and a Lorentzian distribution of the oscillators' natural frequencies. Depending on the size of the attractive and random coupling terms, the system displays four states: complete incoherence, partial synchronization, partial antiphase synchronization, and a mix of antiphase and ordinary synchronization.

4.2 Introduction

The study of collective synchronization has been greatly enriched by ideas from statistical physics. In 1967 Winfree discovered the first and still most influential link between these fields [91]. While exploring a toy model for interacting fireflies, pacemaker cells, or other large populations of biological oscillators, he found that synchronization behaved like a critical phenomenon: it occurred only when the attractive coupling between the oscillators exceeded a certain threshold. The onset of synchronization was strikingly analogous to a second-order phase transition, with the important conceptual difference that Winfree's system ordered itself in time, not space. In this analogy, the temporal alignment

of oscillator phases played the same role as the spatial alignment of spins in a ferromagnetic phase transition.

Since then, many other theorists have deepened and extended this analogy between synchronization in time and phase transitions in space [1, 84, 76, 85]. The field took off after Kuramoto [64] elegantly reformulated Winfree's model and derived its collective behavior analytically, using a dynamical version of mean-field theory.

Yet one question has long remained murky. Can a population of oscillators with a random mix of attractive and repulsive couplings undergo a transition to an "oscillator glass" [22], the temporal analog of a spin glass [10]? The main difficulty here (as well as in the work of Winfree and Kuramoto) is that these types of systems are composed of self-sustained limit-cycle oscillators, and hence are inherently far from equilibrium. As such, the methods of equilibrium statistical mechanics do not apply. Nor have simulations settled the issue. Daido [23] simulated an oscillator analog of the Sherrington-Kirkpatrick spin-glass model [79] and reported evidence for algebraic relaxation to a glassy form of synchronization, but those results have been challenged [82, 24, 83]. Other authors have looked for oscillator glass in simpler models with site disorder (that is, where the randomness is intrinsic to the oscillators themselves, not to the couplings between them) [22, 13, 73, 50, 48]. Even in this setting the existence or nonexistence of an oscillator glass state remains an open problem.

In this chapter we revisit one of the earliest models proposed for oscillator glass [13]: a Kuramoto model whose attractive coupling is modified to include quenched random interactions of the form used by van Hemmen in his model of spin glasses [87]. The model can now be solved exactly, thanks to a

remarkable ansatz recently discovered by Ott and Antonsen [72]. Their breakthrough has already cleared up many other longstanding problems about the Kuramoto model and its offshoots [18, 75, 71, 68, 66, 48, 57, 69, 49, 50]. For the Kuramoto-van Hemmen model examined here, the Ott-Antonsen ansatz reveals that the model's long-term macroscopic dynamics are reducible to an eight-dimensional system of ordinary differential equations. Two physically important consequences are that the model does not exhibit algebraic relaxation to any of its attractors, nor does it have the vast number of metastable states one would expect of a glass. On the other hand, the frustration in the system does give rise to two states whose glass order parameter is non-zero above a critical value of the van Hemmen coupling strength.

4.3 Equations of motion and numerical simulations

The governing equations of the model are

$$\dot{\theta}_i = \quad \omega_i + \sum_{j=1}^{N} K_{ij} \sin(\theta_j - \theta_i) \tag{4.1}$$

for $i = 1, \ldots, N \gg 1$, where

$$K_{ij} = \frac{K_0}{N} + \frac{K_1}{N}(\xi_i \eta_j + \xi_j \eta_i). \tag{4.2}$$

Here θ_i is the phase of oscillator i and ω_i is its natural frequency, randomly chosen from a prescribed distribution $g(\omega)$ which we take to be a Lorentzian of width γ and zero mean: $g(\omega) = \gamma/[\pi(\omega^2 + \gamma^2)]$. By rescaling time, we may set $\gamma = 1$ without loss of generality. The parameters $K_0,\ K_1 \geq 0$ are the Kuramoto and van Hemmen coupling strengths, respectively. The random variables ξ_i and η_i are independent and take the values ± 1 with equal probability.

Simulations of the model (Fig. 4.1) show four types of long-term behavior. (1) *Incoherence* (Fig. 4.1(a)): When K_0 and K_1 are small, the oscillators run at their natural frequencies and their phases scatter. (2) *Partial locking* (Fig. 4.1(b)): If we increase K_0 while keeping K_1 small, oscillators in the middle of the frequency distribution lock their phases while those in the tails remain desynchronized. (3) *Partial antiphase locking* (Fig. 4.1(c)): If instead we increase K_1 while keeping K_0 small, the system settles into a state of partial antiphase synchronization, where half of the central oscillators lock their phases 180 degrees apart while the other half behaves incoherently. (4) *Mixed state* (Fig. 4.1(d)): If both K_0 and K_1 are sufficiently large and in the right proportion, we find a mixed state that combines aspects of the partially locked and antiphase locked states. But note two changes—the central oscillators that behaved incoherently in Fig. 4.1(c) now lock as in Fig. 4.1(b), and the antiphase locked oscillators of Fig. 4.1(c) are now less than 180 degrees apart.

These four states are not new. They were found and analyzed by Bonilla et al. [13] for a variant of Eq. (4.1) with a white noise term and a uniform (not Lorentzian) distribution of natural frequencies. The advantage of the present system is that the stability properties and phase boundaries of the four states can be obtained analytically. Figure 4.2 shows the resulting phase diagram.

4.4 Analysis via the Ott-Antonsen Ansatz

We turn now to the analysis. As mentioned above, the Ott-Antonsen ansatz [72] has become standard, so we suppress the intermediate steps in the following derivation (but see [72] for details). The ansatz applies to (4.1) in the continuum

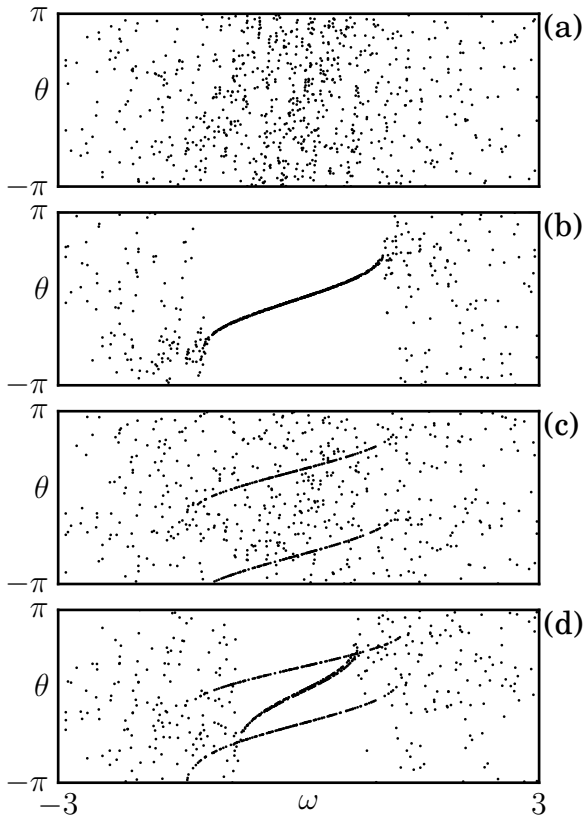

Figure 4.1: Statistical steady states for the Kuramoto-van Hemmen model. Equation (4.1) was integrated numerically for $N = 1000$ oscillators with Lorentzian distributed frequencies and random initial phases, using a fourth-order Runge-Kutta method with a fixed step size of 0.05. Parameter values: (a) Incoherence: $K_0 = 1, K_1 = 1$; (b) Partial locking: $K_0 = 2.5, K_1 = 1$; (c) Partial antiphase locking: $K_0 = 1, K_1 = 2.75$; (d) Mixed state: $K_0 = 2.5, K_1 = 2.75$. Only oscillators with $-3 \leq \omega \leq 3$ are shown.

limit and restricts attention to an invariant manifold that determines the system's long-term dynamics [71]. On this manifold the time-dependent density $\rho(\theta, t, \omega, \xi, \eta)$ of oscillators at phase θ with natural frequency ω and van Hemmen parameters ξ, η is given by

$$\rho = \frac{1}{2\pi}\left\{1 + \left[\sum_{n=1}^{\infty}(\alpha^* e^{i\theta})^n + \text{ c.c.}\right]\right\} \tag{4.3}$$

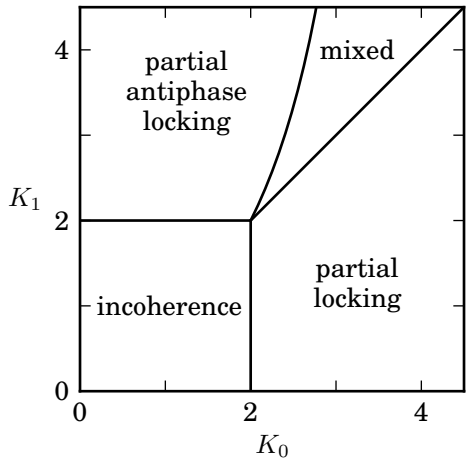

Figure 4.2: Phase diagram for (4.1), (4.2) with $g(\omega) = 1/[\pi(1+\omega^2)]$.

where $\alpha = \alpha(t, \omega, \xi, \eta)$ and the asterisk and c.c. denote complex conjugation. This density evolves according to the continuity equation

$$\frac{\partial \rho}{\partial t} + \frac{\partial}{\partial \theta}(\rho v) = 0 \tag{4.4}$$

where $v = v(t, \omega, \xi, \eta)$ denotes the velocity field in the continuum limit,

$$v = \omega + \mathrm{Im}[e^{-i\theta}(K_0 Z + K_1 \xi W_\eta + K_1 \eta W_\xi) + \text{ c.c.}] \tag{4.5}$$

and the complex order parameters Z, W_ξ, and W_η are given by

$$\begin{aligned} Z &= \langle e^{i\theta} \rangle, \\ W_\xi &= \langle \xi e^{i\theta} \rangle, \\ W_\eta &= \langle \eta e^{i\theta} \rangle. \end{aligned} \tag{4.6}$$

The angle brackets $\langle \cdot \rangle$ denote integration with respect to the probability measure $\rho(\theta)d\theta\, g(\omega)d\omega\, p(\xi)d\xi\, p(\eta)d\eta$. The distribution p is the normalized distribution on ξ (resp. η) such that ξ (resp. η) equals $+1$ or -1 with equal probability $\frac{1}{2}$.

When (4.3) and (4.5) are inserted into (4.4), one finds that the dependence on θ is satisfied identically if $\alpha(t, \omega, \xi, \eta)$ evolves according to the following system

of integro-differential equations:

$$\begin{aligned}\dot{\alpha} &= -\frac{\alpha^2}{2}\left[K_0 Z^* + K_1\left(\xi W_\eta^* + \eta W_\xi^*\right)\right] + i\omega\alpha \\ &\quad + \frac{1}{2}[K_0 Z + K_1(\xi W_\eta + \eta W_\xi)]. \end{aligned} \tag{4.7}$$

This system is infinite-dimensional, since there is one equation for each real ω. But its macroscopic dynamics are governed by a much smaller, finite-dimensional set of ODEs. The reduction occurs because the different $\alpha(t, \omega, \xi, \eta)$ in (4.7) are coupled only through the order parameters Z, W_ξ, and W_η. Those order parameters in turn are expressible, via (4.6), as integrals involving ρ and therefore α itself. Under the usual analyticity assumptions [72] on α, the various integrals can be expressed in terms of a finite set of α's, and these obey the promised ODEs, as follows.

Consider $Z = \int e^{i\theta}\rho(\theta)d\theta\, g(\omega)d\omega\, p(\xi)d\xi\, p(\eta)d\eta$. To calculate this multiple integral, first substitute (4.3) for ρ and perform the integration over θ to get $Z = \int \alpha\, g(\omega)d\omega\, p(\xi)d\xi\, p(\eta)d\eta$. Second, evaluate the integral $\int_{-\infty}^{\infty} \alpha\, g(\omega)d\omega$ by considering ω as a complex number and computing the resulting contour integral, choosing the contour to be an infinitely large semicircle closed in the upper half plane. The Lorentzian $g(\omega) = 1/[\pi(1 + \omega^2)]$ has a simple pole at $\omega = i$, so the residue theorem yields

$$\int_{-\infty}^{\infty} \alpha\, g(\omega)d\omega = \alpha(t, i, \xi, \eta). \tag{4.8}$$

Third, integrate over ξ and η. Since these variables take the values ± 1 with equal probability, Z receives contributions from four subpopulations, corresponding to $(\xi, \eta) = (+1, +1)$, $(+1, -1)$, $(-1, +1)$, and $(-1, -1)$. If we define the sub-order

parameters for these subpopulations as

$$\begin{aligned} A(t) &= \alpha(t, i, +1, +1) \\ B(t) &= \alpha(t, i, -1, -1) \\ C(t) &= \alpha(t, i, +1, -1) \\ D(t) &= \alpha(t, i, -1, +1), \end{aligned} \tag{4.9}$$

we find that Z is given by

$$Z = \frac{1}{4}(A + B + C + D). \tag{4.10}$$

Similar calculations show that the glass order parameters can also be expressed in terms of A, B, C, D:

$$\begin{aligned} W_\xi &= \frac{1}{4}(A - B + C - D), \\ W_\eta &= \frac{1}{4}(A - B - C + D). \end{aligned} \tag{4.11}$$

The sub-order parameters A, B, C, D have physical meanings. For example, A can be thought of as a giant oscillator, a proxy for all the microscopic oscillators with $(\xi, \eta) = (+1, +1)$. Likewise, B, C and D represent giant oscillators for the other subpopulations.

The equations of motion for these giant oscillators are obtained by inserting (4.10), (4.11) into (4.7) and analytically continuing to $\omega = i$. The result is the

following closed system:

$$\begin{aligned}
\dot{A} &= -\frac{1}{2}A^2[K_0Z^* + \frac{K_1}{2}(A^* - B^*)] - A \\
&\quad + \frac{1}{2}[K_0Z + \frac{K_1}{2}(A - B)] \\
\dot{B} &= -\frac{1}{2}B^2[K_0Z^* + \frac{K_1}{2}(B^* - A^*)] - B \\
&\quad + \frac{1}{2}[K_0Z + \frac{K_1}{2}(B - A)] \\
\dot{C} &= -\frac{1}{2}C^2[K_0Z^* + \frac{K_1}{2}(D^* - C^*)] - C \\
&\quad + \frac{1}{2}[K_0Z + \frac{K_1}{2}(D - C)] \\
\dot{D} &= -\frac{1}{2}D^2[K_0Z^* + \frac{K_1}{2}(C^* - D^*)] - D \\
&\quad + \frac{1}{2}[K_0Z + \frac{K_1}{2}(C - D)]. \qquad (4.12)
\end{aligned}$$

Since A, B, C, and D are complex numbers, the system (4.12) is eight-dimensional.

The four steady states shown in Fig. 4.1 correspond to four families of fixed points of (4.12), each of which is characterized by a simple configuration of A, B, C, D in the complex plane. Figure 4.3 plots those four families schematically on the phase diagram, showing where each exists and is linearly stable. We discuss them in turn.

The incoherent state of Fig. 4.1(a) corresponds to the fixed point at the origin, $A = B = C = D = 0$, with order parameters $Z = W_\xi = W_\eta = 0$. It exists for all $K_0,\ K_1 \geq 0$ but is linearly stable iff (if and only if) $K_0 < 2$ and $K_1 < 2$. This stability region is shown as the square in the lower left of Fig. 4.3.

The partially locked state (Fig. 4.1(b)) corresponds to a configuration where A, B, C and D all equal the same nonzero complex number, as shown in the lower right panel of Fig. 4.3. By the rotational symmetry of the system, we can assume

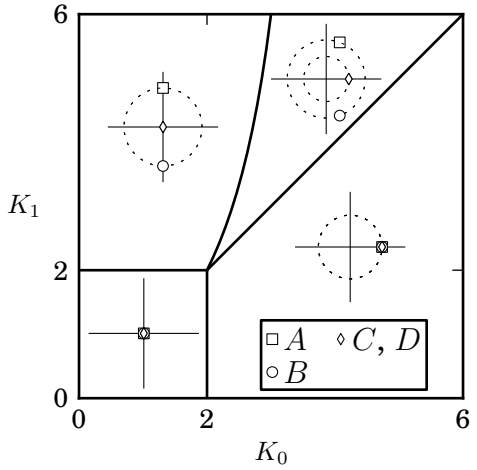

Figure 4.3: Stable fixed points A, B, C, D for the four states. In each panel, the axes show the region of the complex plane with $-1 \leq \mathrm{Re}(z) \leq 1$ and $-1 \leq \mathrm{Im}(z) \leq 1$. Rotationally equivalent fixed points lie on the dashed circles.

that $A = B = C = D = R_{PL} > 0$. Such a state is a fixed point of (4.12) iff $K_0 > 2$ and $R_{PL} = \sqrt{1 - 2/K_0}$, in which case it is linearly stable iff $K_1 < K_0$. (There is a trivial zero eigenvalue associated with the rotational symmetry, so what we really mean is that the state is linearly stable to all perturbations other than rotational ones. Likewise, there is a whole circle of partially locked states, all equivalent up to rotation, as indicated by the dashed circle in the lower right panel of Fig. 4.3.) The order parameters are $Z = \sqrt{1 - 2/K_0}$ and $W_\xi = W_\eta = 0$.

The antiphase state (Fig. 4.1(c)) corresponds to a fixed point where $A = -B = R_A > 0$ and $C = D = 0$. It exists iff $K_1 > 2$ and $R_A = \sqrt{1 - 2/K_1}$. When it exists it is linearly stable iff

$$K_0 < 4K_1/(2 + K_1). \tag{4.13}$$

Finally, the mixed state (Fig. 4.1(d)) corresponds to a configuration where $A = B^*$ and $C = D = R_M > 0$. It exists iff $K_1 > 2$ and $4K_1/(2 + K_1) < K_0 < K_1$ (the

wedge in the upper right of Fig. 4.3) and satisfies

$$\begin{aligned} \mathrm{Re}(A) &= \frac{K_0}{2K_1 - K_0}\sqrt{1 + \frac{2}{K_1} - \frac{4}{K_0}} \\ \mathrm{Im}(A) &= 2\sqrt{\frac{(K_1 - K_0)(K_1(K_1 - 2) + K_0)}{K_1(2K_1 - K_0)^2}} \\ R_M &= \sqrt{1 + \frac{2}{K_1} - \frac{4}{K_0}}. \end{aligned} \tag{4.14}$$

We were unable to find the eigenvalues analytically in this final case, but we verified linear stability numerically for a sample of mixed states up to $K_1 = 10^5$.

All the transitions on the stability boundaries of Fig. 4.3 are continuous and non-hysteretic. In particular, the mixed state morphs continuously into the antiphase state on the left side of its stability region, and into the partially locked state on the right side. To verify this, observe that the configuration of A, B, C, D in the mixed state, as parametrized by Eq. (4.14), continuously deforms into the states on either side of it as (K_1, K_2) approaches the relevant stability boundary.

4.5 Conclusion

The glass order parameters W_ξ and W_η are nonzero for the antiphase and mixed states, so in that specific sense the model can be said to exhibit a glassy form of synchronization [13]. Moreover, $W_\xi = W_\eta$ for all four states, which confirms a conjecture of Bonilla et al. [13]. On the other hand, the oscillator model (4.1), (4.2) lacks other defining features of a glass, such as a large multiplicity of metastable states and non-exponential relaxation dynamics; the same is true of the original van Hemmen spin-glass model [19].

Experimental tests of the phase diagram predicted here may be possible in

a variety of oscillator systems with programmable coupling. Prime candidates are optical arrays [47] or populations of photosensitive chemical oscillators [86] in which the interactions are mediated by a computer-controlled spatial light modulator.

BIBLIOGRAPHY

[1] Juan A. Acebrón, L. L. Bonilla, Conrad J. Pérez Vicente, Félix Ritort, and Renato Spigler. The kuramoto model: A simple paradigm for synchronization phenomena. *Rev. Mod. Phys.*, 77:137–185, Apr 2005.

[2] E. Allgower and K. Georg. *Numerical Continuation Methods: An Introduction*. Springer-Verlag, New York, 1990.

[3] X. b. Lin. Using Mel'nikov's method to solve Šilnikov's problems. In *Proc. Roy*, pages 295–325, 116, 1990. Soc. Edinburgh Sect. A.

[4] S. M. Baer and T. Erneux. Singular Hopf bifurcation to relaxation oscillations. *SIAM Journal on Applied Mathematics*, 46:721–739, 1986.

[5] M. Benedicks and L.S. Young. Absolutely continuous invariant measures and random perturbations of certain one-dimensional maps. *ETDS*, 12:13–37, 1992.

[6] E. Benoît. Canards et enlacements. *Inst. Études Sci Publ. Math*, 72:63–91, 1990.

[7] É. Benoît. Canards et enlacements. *Inst. Hautes Études Sci. Publ. Math*, 72:63–91, 1990.

[8] W.-J. Beyn. Global bifurcations and their numerical computation. In *Continuation and Bifurcations: Numerical Techniques and Applications*, pages 169–181. D. Roose et. al., eds., NATO Adv. Sci. Inst. Ser. C Math. Phys. Sci. 313, Kluwer, Dordrecht, The Netherlands, 1990.

[9] W.-J. Beyn. The numerical computation of connecting orbits in dynamical systems. *The numerical computation of connecting orbits in dynamical systems*, 10:379–405, 1990.

[10] K. Binder and A. P. Young. Spin glasses: Experimental facts, theoretical concepts, and open questions. *Rev. Mod. Phys.*, 58:801–976, Oct 1986.

[11] G.D. Birkhoff. Nouvelles recherches sur les systèmes dynamiques. In *Collected Mathematical Papers, Vol. 2*, pages 530–662. Amer. Math. Soc., Providence, R.I., 1950.

[12] K. Bold, C. Edwards, J. Guckenheimer, S. Guharay, K. Hoffman, J. Hubbard, R. Oliva, and W. Weckesser. The forced van der Pol equation II: Canards in the reduced system. *SIAM J. Appl. Dyn. Syst.*, 2(4):570–608, 2003.

[13] LL Bonilla, CJ Pérez Vicente, and JM Rubi. Glassy synchronization in a population of coupled oscillators. *Journal of Statistical Physics*, 70(3-4):921–937, 1993.

[14] B. Braaksma. Singular Hopf bifurcation in systems with fast and slow variables. *J. Nonlinear Sci*, 8:457–490, 1998.

[15] B. Braaksma. Singular Hopf bifurcation in systems with fast and slow variables. *J. Nonlinear Sci.*, 8:459–490, 1998.

[16] M. Brøns, M. Krupa, and M. Wechselberger. Mixed mode oscillations due to the generalized canard phenomenon. *Bifurcation Theory and Spatio-Temporal Pattern Formation, Fields Inst. Commun., AMS, Providence RI*, 40:39–63, 2006.

[17] A. R. Champneys, Yu. A. Kuznetsov, and B. Sandstede. A numerical toolbox for homoclinic bifurcation analysis. *Internat. J. Bifur. Chaos Appl. Sci. Engrg.*, 6:867–887, 1996.

[18] L. M. Childs and S. H. Strogatz. Stability diagram for the forced Kuramoto model. *Chaos*, 18(4):043128, December 2008.

[19] TC Choy and D Sherrington. The van hemmen model-a true spin glass? *Journal of Physics C: Solid State Physics*, 17(4):739, 1984.

[20] P. Coullet and C. Tresser. Itérations d'endomorphismes et groupe de renormalisation. *J. Physique*, 8:C5–25, 1978.

[21] J.D. Crawford. Amplitude expansions for instabilities in populations of globally-coupled oscillators. *J. Stat. Phys.*, 74(5-6):1047–1084, 1994.

[22] H. Daido. Scaling behaviour at the onset of mutual entrainment in a population of interacting oscillators. *J. Phys. A: Math. Gen.*, 20:L629–L636, July 1987.

[23] Hiroaki Daido. Order function and macroscopic mutual entrainment in uniformly coupled limit-cycle oscillators. *Prog. Theor. Phys.*, 88(6):1213–1218, 1992.

[24] Hiroaki Daido. Algebraic relaxation of an order parameter in randomly coupled limit-cycle oscillators. *Phys. Rev. E*, 61:2145–2147, Feb 2000.

[25] M. Desroches, J. Guckenheimer, B. Krauskopf, C. Kuehn, H. Osinga, and M. Wechselberger. Mixed-mode oscillations with multiple time scales. *SIAM Review*, 54:211–288, 2012.

[26] A. Dhooge, W. Govaerts, and Yu. A. Kuznetsov. Matcont: A matlab package for numerical bifurcation analysis of ODEs. *ACM Trans. Math*, 29:141–164, 2003. Available online from www.matcont.ugent.be/.

[27] M. Diener. The canard unchained or how fast/slow dynamical systems bifurcate. *Math. Intelligencer*, 6:38–48, 1984.

[28] E. Doedel. *AUTO: Software for continuation and bifurcation problems in ordinary differential equations*. Available online from.

[29] F. Dumortier and R. Roussarie. Canard cycles and center manifolds. *Mem*, 121:457–490, 1996.

[30] M. J. Feigenbaum. Quantitative universality for a class of nonlinear transformations. *J. Stat. Phys.*, 19:25–52, 1978.

[31] N. Fenichel. Persistence and smoothness of invariant manifolds for flows. *Math. JIndiana Univ*, 21:193–226, 1972.

[32] N. Fenichel. Persistence and smoothness of invariant manifolds for flows. *Indiana Univ. Math. J.*, 21:193–226, 1972.

[33] P. Glendinning and C. Sparrow. Local and global behavior near homoclinic orbits. *J. Stat Phys*, 35:645–696, 1984.

[34] P. Glendinning and C. Sparrow. Local and global behavior near homoclinic orbits. *J. Stat. Phys.*, 35:645–696, 1984.

[35] A. Goryachev, P. Strizhak, and R. Kapral. Slow manifold structure and the emergence of mixed-mode oscillations. *J. Phys Chem*, 107(18):2881–2889, 1997.

[36] J. Guckenheimer. Return maps of folded nodes and folded saddle-nodes. *Chaos*, 18:015108, 2008.

[37] J. Guckenheimer. Singular Hopf bifurcation in systems with two slow variables. *SIAM J. Appl. Dyn. Syst.*, 7:1355–1377, 2008.

[38] J. Guckenheimer, K. Hoffman, and W. Weckesser. Numerical computation of canards. *Internat. J. Bifur. Chaos Appl. Sci*, 10:2669–2687, 2000.

[39] J. Guckenheimer and P. Holmes. *Nonlinear Oscillations, Dynamical Systems, and Bifurcations of Vector Fields*. Springer-Verlag, Berlin, New York, 1983.

[40] J. Guckenheimer and C. Kuehn. Computing slow manifolds of saddle type. *SIAM J. Appl. Dyn. Syst.*, 8(3):854–879, 2009.

[41] J. Guckenheimer and D. LaMar. *Periodic orbit continuation in multiple time scale systems*. Numerical continuation methods for dynamical systems, pp. 253–267, Underst. Complex Syst., Springer, Dordrecht, 2007.

[42] J. Guckenheimer and I. Lizarraga. Shilnikov bifurcation of mixed-mode oscillations. *SIAM J. Appl. Dyn. Syst.*, 14:764–786, 2015.

[43] J. Guckenheimer and P. Meerkamp. Unfoldings of singular Hopf bifurcation. *SIAM Journal on Applied Dynamical Systems*, 11:1325–1359, 2012.

[44] J. Guckenheimer and P. Meerkamp. Unfoldings of singular Hopf bifurcation. *SIAM J. Appl. Dyn. Syst.*, 11:1325–1359, 2012.

[45] J. Guckenheimer and H. Osinga. The singular limit of a Hopf bifurcation. *Discrete Cont. Dyn. Syst.*, 32:2805–2823, 2012.

[46] J. Guckenheimer and H. M. Osinga. The singular limit of a Hopf bifurcation. *Discrete Contin. Dyn. Syst.*, 32:2805–2823, 2012.

[47] Aaron M Hagerstrom, Thomas E Murphy, Rajarshi Roy, Philipp Hövel, Iryna Omelchenko, and Eckehard Schöll. Experimental observation of chimeras in coupled-map lattices. *Nature Physics*, 8(9):658–661, 2012.

[48] Hyunsuk Hong and Steven H. Strogatz. Kuramoto model of coupled oscillators with positive and negative coupling parameters: An example of conformist and contrarian oscillators. *Phys. Rev. Lett.*, 106:054102, Feb 2011.

[49] D. Iatsenko, S. Petkoski, P. V. E. McClintock, and A. Stefanovska. Stationary and Traveling Wave States of the Kuramoto Model with an Arbi-

trary Distribution of Frequencies and Coupling Strengths. *Phys. Rev. Lett.*, 110(6):064101, February 2013.

[50] Dmytro Iatsenko, Peter VE McClintock, and Aneta Stefanovska. Oscillator glass in the generalized kuramoto model: synchronous disorder and two-step relaxation. *arXiv preprint arXiv:1303.4453*, 2013.

[51] M. Wechselberger J. Guckenheimer and L.-S. Young. Chaotic attractors of relaxation oscillators. *Nonlinearity*, 19:701–720, 2006.

[52] M. V. Jakobson. Absolutely continuous invariant measures for one-parameter families of one-dimensional maps. *Comm. Math. Phys.*, 81:39–88, 1981.

[53] C. K. R. T. Jones. *Geometric Singular Perturbation Theory*. Lecture Notes in Math. 1609, Springer, Berlin, Heidelberg, 1995.

[54] C. K. R. T. Jones and N. Kopell. Tracking invariant manifolds with differential forms in singularly perturbed systems. *J. Differential Equations*, 108:64–88, 1994.

[55] C.K.R.T. Jones. *Geometric Singular Perturbation Theory*. Lecture Notes in Math. 1609. Springer, Berlin, Heidelberg, 1995.

[56] C.K.R.T. Jones and N. Kopell. Tracking invariant manifolds with differential forms in singularly perturbed systems. *J. Differential Equations*, 108:64–88, 1994.

[57] M. Komarov and A. Pikovsky. Effects of nonresonant interaction in ensembles of phase oscillators. *Phys. Rev. E*, 84(1):016210, July 2011.

[58] M. T. M. Koper and P. Gaspard. Mixed-mode and chaotic oscillations in a simple model of an electrochemical oscillator. *J. Phys*, 95:4945–4947, 1991.

[59] M. T. M. Koper and P. Gaspard. The modeling of mixed-mode and chaotic oscillations in electrochemical systems. *J. Chem. Phys.*, 96:7797–7813, 1992.

[60] M. T. M. Koper and P. Gaspard. The modeling of mixed-mode and chaotic oscillations in electrochemical systems. *J. Chem. Phys.*, 96:7797–7813, 1992.

[61] M. Krupa and M. Wechselberger. Local analysis near a folded saddle-node singularity. *J. Differential Equations*, 12:2841, 2010.

[62] M. Krupa and M. Wechselberger. Local analysis near a folded saddle-node singularity. *J. Differential Equations*, 248:2841–2888, 2010.

[63] Y. Kuramoto. *Chemical Oscillations, Waves, and Turbulence*. Springer-Verlag, Berlin Heidelberg, 1984.

[64] Y. Kuramoto. *Chemical Oscillations, Waves, and Turbulence*. Springer, Berlin, 1984.

[65] Y. Kuznetsov. *Elements of Applied Bifurcation Theory*. Springer-Verlag, New York, 1998.

[66] Carlo R. Laing. The dynamics of chimera states in heterogeneous kuramoto networks. *Physica D*, 238(16):1569 – 1588, 2009.

[67] N. Levinson. Perturbations of discontinuous solutions of non-linear systems of differential equations. *Acta Math*, 82:71–106, 1950.

[68] E. A. Martens, E. Barreto, S. H. Strogatz, E. Ott, P. So, and T. M. Antonsen. Exact results for the kuramoto model with a bimodal frequency distribution. *Phys. Rev. E*, 79:026204, Feb 2009.

[69] E. Montbrió and D. Pazó. Collective synchronization in the presence of reactive coupling and shear diversity. *Phys. Rev. E*, 84(4):046206, October 2011.

[70] T. Nowicki and S. van Strien. Absolutely continuous invariant measures for c^2 unimodal maps satisfying the collet-eckmann conditions. *Invent. Math.*, 93(3):619–635, 1988.

[71] E. Ott and T. M. Antonsen. Long time evolution of phase oscillator systems. *Chaos*, 19(2):023117, June 2009.

[72] Ed Ott and Thomas M Antonsen. Low dimensional behavior of large systems of globally coupled oscillators. *Chaos*, 18(3):037113, 2008.

[73] Gabriel H. Paissan and Damin H. Zanette. Synchronization of phase oscillators with heterogeneous coupling: A solvable case. *Physica D*, 237(6):818 – 828, 2008.

[74] G. Pianigiani and J.A. Yorke. Expanding maps on sets which are almost invariant: decay and chaos. *Trans. AMS*, 252:351–366, 1979.

[75] A. Pikovsky and M. Rosenblum. Partially Integrable Dynamics of Hierarchical Populations of Coupled Oscillators. *Phys. Rev. Lett.*, 101(26):264103, December 2008.

[76] Arkady Pikovsky, Michael Rosenblum, and Jürgen Kurths. *Synchronization*. Cambridge University Press, 2003.

[77] F. Diener É Benoît, J.-L. Callot and M. Diener. Chasse au canards. *Collect. Math.*, 31:37–119, 1981.

[78] S. Schecter. Rate of convergence of numerical approximations to homoclinic bifurcation points. *IMA J. Numer. Anal*, 15:23–60, 1995.

[79] David Sherrington and Scott Kirkpatrick. Solvable model of a spin-glass. *Phys. Rev. Lett.*, 35:1792–1796, Dec 1975.

[80] L.P. Silnikov. A case of the existence of a denumerbale set of periodic motions. *Sov. Math. Dokl.*, 6:163–166, 1965.

[81] S. Smale. *Diffeomorphisms with many periodic points*, pages 63–80. Differential and Combinatorial Topology. Princeton Univ. Press, Princeton, N.J., 1965.

[82] J. C. Stiller and G. Radons. Dynamics of nonlinear oscillators with random interactions. *Phys. Rev. E*, 58:1789–1799, Aug 1998.

[83] J. C. Stiller and G. Radons. Self-averaging of an order parameter in randomly coupled limit-cycle oscillators. *Phys. Rev. E*, 61:2148–2149, Feb 2000.

[84] Steven H. Strogatz. From kuramoto to crawford: exploring the onset of synchronization in populations of coupled oscillators. *Physica D*, 143(14):1 – 20, 2000.

[85] Steven H Strogatz. *Sync*. Hyperion, 2003.

[86] Mark R Tinsley, Simbarashe Nkomo, and Kenneth Showalter. Chimera and phase-cluster states in populations of coupled chemical oscillators. *Nature Physics*, 8(9):662–665, 2012.

[87] JAN L VAN HEMMEN. CLASSICAL SPIN-GLASS MODEL. *Phys. Rev. Lett.*, 49:409–412, 1982.

[88] Q. WANG AND L.-S. YOUNG. TOWARD A THEORY OF RANK ONE ATTRACTORS. *Ann. Math.*, 167:349–480, 2008.

[89] M. WECHSELBERGER. EXISTENCE AND BIFURCATION OF CANARDS IN $\mathbb{R}^3$ IN THE CASE OF A FOLDED NODE. *SIAM Journal on Applied Dynamical Systems*, 4:101–139, 2005.

[90] M. WECHSELBERGER. EXISTENCE AND BIFURCATION OF CANARDS IN $\mathbb{R}^3$ IN THE CASE OF A FOLDED NODE. *SIAM. J. Appl. Dyn. Syst.*, 4:101–139, 2005.

[91] ARTHUR T. WINFREE. BIOLOGICAL RHYTHMS AND THE BEHAVIOR OF POPULATIONS OF COUPLED OSCILLATORS. *J. Theor. Biol.*, 16(1):15 – 42, 1967.